DESIGN, SYNTHESIS, AND CHARACTERIZATION OF METAL OXIDE NANOSTRUCTURES FORMED THROUGH NATURAL AND DIRECT-WRITE PROCESSES

by

MEREDITH CHRISTINE SHARPS

A DISSERTATION

Presented to the Department of Chemistry and Biochemistry
and the Graduate School of the University of Oregon
in partial fulfillment of the requirements
for the degree of
Doctor of Philosophy

June 2019

DISSERTATION APPROVAL PAGE

Student: Meredith Christine Sharps

Title: Design, Synthesis, and Characterization of Metal Oxide Nanostructures Formed Through Natural and Direct-Write Processes

This dissertation has been accepted and approved in partial fulfillment of the requirements for the Doctor of Philosophy degree in the Department of Chemistry and Biochemistry by:

Dr. Catherine Page	Chairperson
Dr. James Hutchison	Advisor
Dr. Darren Johnson	Advisor
Dr. Ramesh Jasti	Core Member
Dr. Benjamín Alemán	Institutional Representative

and

Janet Woodruff-Borden	Vice Provost and Dean of the Graduate School

Original approval signatures are on file with the University of Oregon Graduate School.

Degree awarded June 2019

DISSERTATION ABSTRACT

Meredith Christine Sharps

Doctor of Philosophy

Department of Chemistry and Biochemistry

June 2019

Title: Design, Synthesis, and Characterization of Metal Oxide Nanostructures Formed Through Natural and Direct-Write Processes

Inorganic metal oxide nanomaterials are of interest because they exhibit unique properties that can aid in applications including catalysis, energy storage, sensing, and medicine. These properties arise from nanoscale structure, but understanding what structural aspects determine properties and subsequently controlling them remains difficult. Electron microscopes have been integral in both the fabrication of nanomaterials and the analysis of nanoscale structure, enabling the examination of structure related properties and the design of new materials. Direct-writing of metal oxide nanomaterials through electron beam lithography offers a method to explore structural control. Direct-write processes begin from precursors that must first undergo a chemical transformation in a bottom-up approach. However, the chemistry that occurs during electron irradiation is not well understood. The work described in this dissertation investigates the formation process of nanoscale metal oxides through both direct-write electron beam processes and processes used by nature, relying upon electron microscopy to both fabricate and analyze the materials.

This dissertation first introduces recent improvements in characterization techniques that not only advance our understanding of materials for the future, but also allow investigation of man-made materials throughout history. Only recently have improvements in characterization techniques allowed us to uncover the historical use of nanomaterials in cultural heritage, providing an unconventional link between our past, present, and future. The first four studies presented here investigate the chemistry of direct-write electron beam processes. These studies consider the chemistry of the electron beam as a reagent, the importance of precursor structure in the patterning process, the chemical transformations that occur during direct-writing, and the potential to control local structure through precursor choice. These studies all utilize the electron beam as a fabrication tool, identifying ways in which direct-writing can improve device processing and design of materials. The fifth study uses the electron beam as an analysis tool on an unusual cultural heritage sample: a nanoscale metal oxide naturally forming on architectural stone. Analyzing the nanoscale structure of the oxide better informs its natural formation chemistry, which also has implications for a variety of other fields.

This dissertation includes previously published and unpublished co-authored material.

CURRICULUM VITAE

NAME OF AUTHOR: Meredith Christine Sharps

GRADUATE AND UNDERGRADUATE SCHOOLS ATTENDED:

University of Oregon, Eugene, OR
Emory University, Atlanta, GA

DEGREES AWARDED:

Doctor of Philosophy, Chemistry, 2019, University of Oregon
Master of Science, Chemistry, 2015, University of Oregon
Bachelor of Science, Chemistry and Music, 2014, Emory University

AREAS OF SPECIAL INTEREST:

- Materials Science
- Cultural Heritage
- Electron Beam Lithography
- Photoresist Chemistry
- Inorganic Cluster Synthesis
- Nanomaterial Characterization
    - Electron Microscopy
    - Surface Characterization

PROFESSIONAL EXPERIENCE:

Graduate Research Fellow, Department of Chemistry and Biochemistry, University of Oregon, 2016-2019

Graduate Research Intern, Smithsonian Institution Museum Conservation Institute, 2018

Graduate Teaching Assistant, Department of Chemistry and Biochemistry, University of Oregon, 2014-2016

GRANTS, AWARDS, AND HONORS:

Student Scholar Award, Microanalytical Society, 2019

Graduate Research Fellowship Award, National Science Foundation, 2016-2019

Graduate Research Internship Award, National Science Foundation, 2018

Special Opportunity Award, The Graduate School, University of Oregon, 2018

Science Communications Fellowship, Oregon Museum of Science and Industry, 2016

Excellence in Undergraduate Research, Emory University, 2014

Best Technical Achievement Award, REMRSEC REU, Colorado School of Mines, 2013

PUBLICATIONS:

Sharps, M. C.; Frederick, R. T.; Javitz, M. L.; Herman, G. S.; Johnson, D. W.; Hutchison, J. E. Organotin Carboxylate Reagents for Nanopatterning: Chemical Transformations During Direct-Write Electron Beam Processes. *Chem. Mater*. **2019**, *Accepted.*

Crockett, B. M.; Jansons, A. W.; Koskela, K. M.; Sharps, M. C.; Johnson, D. W.; Hutchison, J. E. Influence of Nanocrystal Size on the Optoelectronic Properties of Thin, Solution-Cast Sn-Doped In_2O_3 Films. *Chem. Mater.* **2019**, *31*, 3370-3380.

Sharps, M. C.; Marsh, D. A.; Zakharov, L. N.; Hutchison, J. E.; Johnson, D. W. Implications of Crystal Structure on Organotin Carboxylate Photoresists. *Cryst. Res. Technol.* **2017**, *52*, 1700081.

Marsh, D. A.; Elliott, W. S.; Smith, R. M.; Sharps, M. C.; Baumeister, M. K.; Carnes, M. E.; Zakharov, L. N.; Casey, W. H.; Johnson, D. W. Stable heterometallic cluster ions based on Werner's Hexol. *Angew. Chem. Int. Ed.* **2017**, *56*, 8776-8779.

Fairley, K. C.; Sharps, M. C.; Mitchson, G.; Ditto, J.; Johnson, D. W.; Johnson, D. C. Low Voltage Patterning of $HafSO_x$: Effects of Voltage on Resolution, Contrast, and Sensitivity. *J. Vac. Sci. Technol. B.* **2016**, *34*, 041607.

Greenaway, A. L.; Sharps, M. C.; Boucher, J. W.; Strange, L. E.; Kast, M. G.; Aloni, S.; Boettcher, S. W. Selective Area Epitaxy of GaAs Microstructures by Close-Spaced Vaper Transport for Solar Energy Conversion Applications. *ACS Energy Lett.* **2016**, *1*, 402-408.

Anderson, R. T.; Zang, X.; Fernando, R.; Dzara, M. J.; Ngo, C.; Sharps, M.; Pinals, R.; Pylypenko, S.; Lusk, M. T.; Sellinger, A. Direct Conversion of Hydride- to Siloxane-Terminated Silicon Quantum Dots. *J. Phys. Chem. C.* **2016**, *120*, 25822-25831.

ACKNOWLEDGMENTS

None of this would be possible without the support and guidance of many people. I am lucky to be advised by two incredible professors, Dr. James Hutchison and Dr. Darren Johnson. Jim, I have learned so much from you about what it means to think critically about science, how to mentally navigate unknown and stressful situations, and how to balance hard work, self-care, and adventure. The Journal of Jim's Desk has certainly made me a better writer. Often times you sort through my rambling thoughts and pick out landmarks that guide me towards my goals. Thank you for not letting me lose sight of what I care about. Darren, you have been an amazing role model these past five years. You push for excellence but also realize that life is much more than the product of our hands and minds. I have learned from you that success is not defined by what we do, but by who we are. Your acceptance, kindness, and care speak louder than you know. Thank you for encouraging me to try out different career paths and for your unwavering support. To both of you: my success is your success.

Thank you to my committee members, Dr. Catherine Page, Dr. Ramesh Jasti, and Dr. Benjamín Alemán, for making me feel comfortable in committee meetings and for your encouragement and support in my future. I also would not be here without my previous science mentors, including Dr. Daphne Norton, who told me to consider applying to UO, Dr. Simon Blakey, Dr. Alan Sellinger, Dr. James Kindt, and my high school chemistry teacher, Amy James, who first sparked my love for chemistry.

I am lucky to count many of my co-authors as both mentors and friends. I would like to especially thank Dr. Adam Jansons, Dr. Brandon Crockett, Dr. Annie Greenaway, Dr. Kurtis Fairley, and Dr. David Marsh for their mentorship during my first and second years, their guidance and support throughout graduate school, and their friendships beyond. I would like to thank undergraduate student Madison Javitz for her hard work. To all of these people, I am excited to see where your endeavors and successes lead you.

Part of my research was done during an internship with the Museum Conservation Institute at the Smithsonian Institution. I want to thank Dr. Edward Vicenzi, Dr. Thomas Lam, and Carol Grissom, as well as the other interns and staff who welcomed me to MCI.

I would like to acknowledge National Science Foundation grants (CHE-1102637, CHE-1606982, CHE-1427987, NNCI-1542101), which funded the Center for Sustainable

Materials Chemistry and characterization facilities at both UO and OSU where much of this work was performed. I especially want to thank Dr. Steve Golledge, Dr. Lev Zakharov, Josh Razink, Kurt Langworthy, Julie Chouinard, Bobby Fischer, Dr. Mike Nellist, and Dr. Ryan Frederick for their expertise in a variety of characterization techniques used throughout this work. I would like to acknowledge NSF Grant No. 1309047, which funded me through the form of a Graduate Research Fellowship and a Graduate Research Internship during the past three years.

I do not have the space to thank everyone who helped me throughout graduate school, but I do want to mention some lab mates and friends by name who made this time pleasant. To Dr. Susan Cooper, Dr. Brandon Crockett, and Dr. Brantly Fulton, my fellow Dutchers, for convincing me to join as a joint student and for supporting me in research, in pursuit of adventure, and in life. To past members of my labs: Dr. Tatiana Zaikova, Dr. Adam Jansons, Dr. Samantha Young, Dr. Kurtis Fairley, Dr. David Marsh, and Doug Banning, and to current lab members: Kenyon Plummer, Jaclyn Kellon, Aurora Ginzburg, Tawney Knecht, Raina Krivina, Casey Bisted, Makenna Pennel, Dr. Jessica Lohrman, Dr. Sean Fontenot, Elizabeth Cochran, Lisa Eytel, Jordan Levine, Hazel Fargher, Jeremy Bard, Ngoc-Minh Phan, Trevor Shear, and Thaís De Faria. Thank you for cultivating a welcoming place to work. Thank you to all the chemistry department support staff who make this place run like a well-oiled machine. To Kiran Varani, Janet Macha, and Jeanne Basom, you have all gone above and beyond for me in my time here.

I want to thank the communities I have found in Eugene for giving me a safe and welcoming home: A Community for Minorities in STEM, Graduate Christian Fellowship, and Emmaus Life church. Kiana Kawamura, Lana Angulo, Katie Gedeon, Katie Tassan, Megan Lindsay, Esther Weng, Tai and Micah Donor, Scott and Charissa Lamb, walking through life these past five years has been easier with people like you by my side.

Thank you to my parents, Dr. Paul and Cheryl Sharps, my brother Chris, and my sister-in-law Grishma, for your support, love, and fervent prayer for me. You've seen me struggle more than most people, and I want to thank you for always supporting my path and calling. I am also grateful to Hans Noyes for his friendship, partnership, and support during this last year. I am so looking forward to our future adventures.

Finally, and most importantly, *Soli Deo Gloria*.

Dedicated to Donald Kincheloe Harris (1991-2016).
This one is for the both of us.

TABLE OF CONTENTS

Chapter Page

LIST OF FIGURES

Figure Page

Figure Page

LIST OF TABLES

Table Page

LIST OF SCHEMES

CHAPTER I

INTRODUCTION

Note: Portions of this chapter may appear in an upcoming publication authored by Meredith C. Sharps, Darren W. Johnson, and James E. Hutchison. The chapter is written by M.C.S. with editorial support from D.W.J and J.E.H.

Material Connections Between our Past, Present, and Future

Nature has provided a vast wealth of resources for man to draw upon and to use creatively. From the first documented use of limestone, shell, and clay-based tools by Neolithic man to the digital tools of the 21st century, human civilizations are marked and even distinguished by their use of inorganic materials. Humans have long understood that these inorganic materials have interesting and useful properties. The first civilization to extract metal from ore discovered the malleability and conductivity of copper sometime during the Chalcolithic age, between 5000-1500 BC.[1] The ability to change properties such as hardness, brittleness, and melting point by combining copper with other elements such as tin and arsenic ushered in the Bronze Age. Wrought iron, iron alloys, and steel-based materials were discovered to be stronger than bronze, and the transition to iron-based materials is designated as the Iron Age. Even now, modern society is in the Digital Age, designated by our use of digital and electronic tools created from the same inorganic resources given to us by nature.

For millennia, humans have understood and harnessed the useful properties of materials like glasses, metals, and ceramics. Historically, the properties of these materials have been tuned empirically, driven by practicality, convenience, art, and curiosity. Only in the past 200 years or so have we begun to understand that the atomic structure of a material imparts its properties, leading to a significant shift in how we design the tools that we use. We now manipulate matter to form structures that impart the properties we desire, rather than using the trial-and-error method of the past. More recently, in the past 50 years or so, have we begun to harness and control the properties of *nano*materials, which are defined by the length scale of 1-100 nm. On the nanoscale, materials exhibit unique and often surprising properties compared to their bulk counterparts, but which are similarly imparted by structure.

The recent availability of computer-based analytical techniques has allowed for observation and manipulation at the nanoscale, leading to advancements in technologies aimed at addressing global issues in areas like energy storage, pollution, catalysis, and medicine.[1] It is not often obvious what aspects of structure (size, surface area, material defects, vacancies, architecture, morphology, strain, etc.) cause the properties of nanomaterials to arise. Understanding how the structure of a material impacts its properties can lead to new applications, improvements upon old applications, and design criteria for new materials. However, the ability to study and manipulate matter on the nanoscale is not just limited to finding solutions for current problems. Analyzing the structure and composition of old materials with these new techniques lets us reach into the past, giving us insight into human history, the ways in which ancient civilizations have interacted with materials, and ultimately connects our material heritage with our future.

The development of nanocharacterization techniques, such as electron microscopes and X-ray spectroscopies, has had a powerful impact on the study and creation of nanoscale inorganic materials. This dissertation focuses on the ability to harness electron beams to both create nanomaterials for our future and examine nanomaterials from our past. First, it will explore the chemistry involved in nanolithography, a process originally developed for the semiconductor industry to define device components for integrated circuits. Nanolithography has now been used to fabricate plasmonic arrays, fluidic devices, metamaterials, and has been adapted to materials that can interface with biological systems. This dissertation will explore the chemistry that underlies electron beam lithography with inorganic metal-oxo clusters in an effort to determine material quality for future direct-write applications of functional materials. Second, this dissertation will consider how developments in analytical instrumentation like the electron microscope have been used to understand our past through analysis of cultural heritage materials. Advancements in electron microscopy and focused ion beam (FIB) techniques that have been primarily used in the semiconductor industry for site-specific characterization, compositional analysis, failure analysis, and mitigation and repair of integrated circuit defects[2] are here adapted to study cultural heritage materials.

This introduction first provides a background on the development of modern computer technology and the impact that computers have had on the field of nanotechnology. In particular, the semiconductor industry has been integral in developing the technologies used throughout this dissertation for both fabrication and analysis. Next, the process of electron beam lithography and the materials used to define nanoscale patterns will be introduced. Finally, this introduction will discuss ways in which improvements in electron microscopy have been used to study materials created by ancient cultures, revealing that modern nanotechnology is not so modern after all.

The Transistor and the Rise of the Digital Age

Information technology may be ubiquitous today, but its rise to abundance is recent and its history rich with technological developments, especially those on the nanoscale. The mid-20th century shift from mechanical and analog technologies to digital ones has transformed the way we work, live, and communicate, thanks to the development of the modern computer.[3,4] However, the computer as we know it today – small, personalized, and powerful – was only achievable after the invention of the bipolar transistor in 1947.[5] Although computing technology existed prior to this breakthrough, the transistor, the ability to shrink it, and the subsequent nanotechnology it enabled supported digitalization on a societal scale.

Transistors are semiconductor devices that take input signals and amplify them to generate larger output signals. The first commercial device to use the transistor was the pocket-sized transistor radio. Sounds picked up by a microphone were translated as electrical signals that would be amplified by transistors before reaching the speakers. Prior to this, vacuum tube technologies were used to complete circuits in radios, telephone systems, televisions, and computers. These systems were large, bulky, and unreliable. The commercial success of the hand-held transistor radio paved the way for transistors to be used in other technologies that relied upon vacuum tube systems. By

1960, a new device architecture allowed the transistor to act not just as an amplifier, but also as a switch, allowing a small current applied in one area of the transistor to switch on a larger current in another. The ability to switch a current 'on' or 'off' forms the basis for storing and accessing memory in nearly all modern computing technologies.[6] Billions of transistors now exist in our pockets in the form of integrated circuits, working in concert as the brains behind our mobile devices. The success of the transistor in bringing us into the Digital Age is due, in part, to its ability to be continually miniaturized.

In 1965, the co-founder of Intel, Gordon Moore, predicted that the density of transistors on integrated circuits would double approximately every two years.[7] This idea, known as Moore's Law, became the driving force behind innovation in the semiconductor industry. Increased component density on integrated circuits translates to better performance, and the push to stay on track with Moore's Law has resulted in many advancements over the past 50 years, including high-speed internet, mobile phones, and smart technologies that are beginning to infiltrate cars, homes, and even clothing and accessories.[8] In order to achieve the rate Moore predicted, significant challenges in both fabrication and analysis had to be overcome to create smaller features. These challenges were overcome with help from the nanotechnology field, which was itself enabled by the integrated circuit.

The idea of studying, observing, and creating materials at angstrom length scales was not unique to the semiconductor industry. In 1959, Richard Feynman gave a lecture titled "Plenty of room at the bottom." In this lecture, Feynman predicted advancements in angstrom level material manipulation.[9] His predictions were largely built upon technologies that already existed, but he extrapolated these technologies to the limits of physics, using his imagination to guide the outcome. For example, advancements in electron optics paved the way for the development of electron microscopes by the early 1930s, decades before Feynman's talk. The theoretical resolution of an electron microscope was 0.22 nm, but this was not yet experimentally achievable by the time Feynman described imaging atoms in his lecture (experimentally, this resolution would be achieved in the 1970s).[10] Feynman used these theoretical regimes to imagine things like writing the entire Encyclopedia Britannica on the head of a pin, storing information on the nanometer scale, resolving atoms, and directly manipulating atoms for chemical synthesis. His talk described key ideas behind nanotechnology,[11] a term that was not coined until fifteen years later.

In order to observe and manipulate the world of the small, it took the combined effort of physicists, chemists, engineers, and the commercial drive of the semiconductor-based electronics industry. The development of the integrated circuit, with the transistor as the key component, transformed electronics and enabled the computer-driven analytical techniques we have today, including microscopic techniques like scanning tunneling microscopy (STM) and atomic force microscopy (AFM). These techniques would eventually allow for the visualization of single atoms in 1971[10] and led to the development of the nanotechnology field in the 1980s.[12,13]

As components on integrated circuits shrank smaller than 100 nm, they entered the realm of nanotechnology. Advancements in analytical techniques like scanning electron microscopy (SEM) addressed nanofabrication issues associated with creating high resolution photolithography masks for component design, and focused ion probe (FIB) technologies improved metrology, failure analysis, and device repair of integrated circuits. The invention of the transistor allowed important developments in the field of nanotechnology, and in return, advancements in nanotechnology have helped sustain Moore's Law.

Creating Future Nanomaterials: Lithography and the Chemistry of Patterning

The microfabrication process at the heart of Moore's Law is photolithography. Lithography is the process that allows nanoscale patterns to be defined and transferred from material to material, ultimately defining each component on an integrated circuit and allowing multiple components to be constructed simultaneously.[14] Lithography is currently the most common top-down nanofabrication process and is still used to define integrated circuits in electronic devices.[15] The process itself has been refined through the years in order to improve resolution, thus satisfying the semiconductor industry's push towards higher component density. The minimum component size has decreased by three orders of magnitude since photolithography was first introduced, shrinking from 15 µm in the first integrated circuit to 14 nm today.

Modern photolithography relies upon the interaction of a material with high energy photons, but lithography utilizing other irradiation sources, such as ion-beam, electron-beam, and X-ray lithography, have also been developed. During the process of lithography, a material called a resist is deposited onto a substrate, usually a silicon wafer. When exposed to photons, ions, X-rays, or electrons, the resist will undergo a reaction that induces a change in solubility by either breaking chemical bonds or cross-linking them, depending upon the material. In photolithography, the resist is exposed through a mask used to define the pattern. For lithographies where beams of ions, electrons, or X-rays can be directed using computer programming, patterns can be written directly onto the resist. After exposure, the more soluble portion of the resist can be rinsed away in a developing solution to reveal the pattern (Scheme 1.1). This pattern can then be transferred, either through etching the material underneath the resist or through deposition to add another material, ultimately building up the components of the device. The resist is then selectively removed, revealing the pattern transfer.

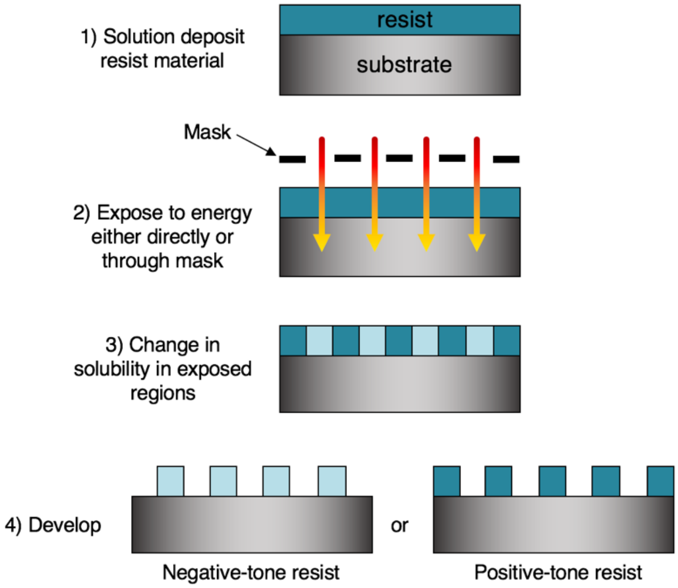

Scheme 1.1. Lithography process. 1) A resist material is solution deposited onto a substrate before being exposed to an irradiation source (2) either through a mask (UV) or directly (X-ray, electron, or ion beam). The irradiated resist undergoes a chemical change (3), causing it to become more or less soluble than the surrounding, non-irradiated resist. Upon developing the film (4), the more soluble portion will rinse away and reveal either a negative-tone or positive-tone pattern.

The critical dimension (CD), or smallest possible patternable feature, is directly related to wavelength of light, shown by equation 1. By reducing the wavelength of incoming radiation, the CD can be reduced, thereby improving resolution.

$$\mathrm{CD} = k_1 \frac{\lambda}{\mathrm{NA}} \tag{1}$$

Where k_1 is a process related coefficient, λ is the wavelength of light, and NA is the numerical aperture of the lens. Many of the efforts to increase resolution have come as a result of decreasing the wavelength of incoming irradiation. The first lithography sources relied on UV light at 436 nm. The current state-of-the-art method uses 193 nm light with immersion lens technology and a multiple-step method.[16]

The smaller wavelengths achievable by sources such as electrons and X-rays can improve theoretical resolution through the relationship in equation 1, but these direct-write processes are often slower compared to photomask exposures and they can only operate under high vacuum. For the semiconductor industry, high throughput and low cost are key, which is why the photomasking process has not been abandoned for other methods that can achieve sub-10 nm resolution. Methods such as electron beam lithography (EBL) are only used industrially to create and define the photomasks used for photolithography.

Improving upon the current state-of-the-art lithography process cannot occur at the current wavelength without detriment to processing time and throughput. For almost a decade, the semiconductor industry has been pushing to decrease the 193 nm wavelength to 13.5 nm, considered extreme ultraviolet (EUV). Theoretically, sub-10 nm lithography can be achieved using single-step exposure. However, switching to EUV poses many challenges before it can fully be adopted and commercialized. One of these areas is in resist development: the chemistries optimized for 193 nm sources are not viable for high resolution at 13.5 nm.

Resist properties are controlled by the chemistry of the patterning mechanism. As the wavelength of light or irradiation source changes, it becomes imperative to tune the resist chemistry to the wavelength of light. There are three main properties of resists: resolution, line edge roughness, and sensitivity (RLS).[17] Resolution describes the minimum size scale achievable by the resist, line edge roughness limits how closely spaced patterns can be as well as the sharpness of the features, and sensitivity is defined as the amount of energy needed to pattern an area, directly relating to write-time and throughput.

Currently, chemically amplified resists are state-of-the-art. These resists, developed in the 80s, typically consist of a resin polymer, a photo-acid generator, and a solvent.[6] The photo-acid generator initiates polymer chain scission when exposed 193 nm. These resists are highly sensitive for deep UV (DUV) wavelengths but face many problems with resolution and pattern transfer, including unwanted diffusion of the photoactive compound, poor thin film energy absorption, and poor etch selectivity.[18–20] A new class of inorganic-based resists have reached records for resolution but require more activation energy for cross-linking, thus resulting in poorer sensitivity for DUV sources. These inorganic resists include materials often consisting of organometallic clusters or nanoparticles with an inorganic core and stabilized by organic ligands. However, the inorganic nature of these materials can maximize absorption of EUV photons, reduce pattern blurring, and increase etch resistance, ultimately improving sensitivity and resolution at 13.5 nm.[17,21,22]

A wide variety of materials have been explored as inorganic resists. Metal oxide sulfate (MSO_x) materials, with sulfate and peroxide groups, have shown high sensitivity at EUV wavelengths.[23–25] Organotin carboxylate clusters have been studied to understand how patterning environment, stabilizing ligand shell, and exposure source influence lithographic properties.[19,26–33] Metal and metal oxide nanoparticles have also been utilized as resists. Both nanoparticles that are stabilized by photoreactive compounds[34–38] and those with long-chain organic ligands[39] have been explored. Despite the different chemistries that occur during exposure of these materials, most inorganic resists form negative-tone patterns that are typically assumed to be dense metal or metal oxides after exposure,[40] lending themselves well towards direct-writing of functional materials.

The semiconductor industry has largely driven the development of resists, focusing on RLS properties at different exposure energies. While some of the inorganic resists listed above have been examined for mechanistic insight, little is known about the chemistries of the reaction, the product that forms, and how the properties of these products are controlled. If we can understand how the precursor material changes during the patterning reaction, it will become feasible to design precursors with qualities specific to a given application. Irradiation products from these reactions can find use as functional materials in applications ranging from optoelectronics, plasmonics, metamaterials, nanophotonics, and in biomedicine.[15] The ability to directly pattern a material transforms lithography from a top-down approach to a bottom-up approach, allowing more chemical control over the structure that forms and ultimately decreasing the number of patterning steps required to fabricate devices.[37]

The majority of this dissertation focuses on understanding the chemistry of inorganic clusters in electron beam lithography applications. Chapter II explores the importance of the electron beam as a reagent in the reaction, and how advances in electron microscopy instrumentation can help achieve higher sensitivity without loss of resolution in hafnium-based resists. This chapter has been previously published in the Journal of Vacuum Science and Technology B (Fairley, K. C.; Sharps, M. C.; Mitchson, G.; Ditto, J.; Johnson, D. W.; Johnson, D. J. Low Voltage Patterning of HafSO$_x$: Effects of Voltage on Resolution, Contrast, and Sensitivity. *J. Vac. Sci. Technol. B.* **2016**, *34*, 041607). Chapter III compares the crystal structure of a series of five organotin clusters, determining what structural factors may influence the chemistry of the patterning reaction. This chapter was previously published in Crystal Research and Technology (Sharps, M. C.; Marsh, D. A.; Zakharov, L. N.; Hutchison, J. E.; Johnson, D. W. Implications of Crystal Structure on Organotin Carboxylate Photoresists. *Cryst. Res. Technol.* **2017**, *52*, 1700081). Chapter IV investigates how the structure of these organotin clusters impacts the patterning reaction and product formation and was previously published in Chemistry of Materials (Sharps, M. C.; Frederick, R. T.; Javitz, M. L.; Herman, G. S.; Johnson, D. W.; Hutchison, J. E. Organotin Carboxylate Reagents for Nanopatterning: Chemical Transformations During Direct-Write Electron Beam Processes. *Chem. Mater.* **2019**, *accepted*). Finally, Chapter V extends this work to combine the use of clusters with colloidal nanocrystals, exploring these materials as tunable, patternable nanocomposites. This chapter was written by me with editorial assistance from Jim Hutchison and Darren Johnson. Experimentation was performed by me, Raina Krivina, Checkers Marshall, and Brandon Crockett.

Nanomaterials and Cultural Heritage: Electron Microscopy Shedding Light on the Past

The conscious effort to understand and fabricate nanomaterials is a modern endeavor, but humans have manufactured synthetic materials for millennia. From metallurgy and pottery to smelting and the use of iron and bronze, human societies are marked by the synthesis of materials.[41] The study of cultural heritage provides a tangible way to understand the history of past human societies and how they created and used materials. Analysis of cultural heritage is difficult, however, constrained by the fragility and rarity of the materials being studied. Historical artifacts are often incredibly old, precious, come in many shapes and sizes, or cannot be physically moved, making many types of analyses difficult because they require physical manipulation of the object or destruction of the material (such as chemical digestion for elemental analysis). Ideal analysis for cultural heritage must check a multitude of boxes, including being non-destructive, fast, universal, versatile, sensitive, and multi-elemental.[42] Very few techniques can cover all of these requirements, and it often takes a variety of complementary techniques to gain information about a specimen. With improvements in nanocharacterization techniques, it has become easier to gain in-depth information non-invasively from small amounts of material. Techniques that combine multiple analyses, like electron microscopes equipped with X-ray spectroscopies, have shown wide versatility when faced with the material challenges of studying cultural heritage.

Until the 20th century, the ability to image nanoscale objects was impossible. The resolution of microscopes was limited by the wavelength of visible light focused by optical lenses. In the 1920s, the development of electron optics began when it was discovered that magnetic fields could act as lenses to focus beams of electrons,[10] which have wavelengths five orders of magnitude below that of visible light. In 1931, the first transmission electron microscope (TEM) was constructed. In TEM, electrons pass through a sample to hit a detector on the opposite side of the sample, imaging the material by what is transmitted. This type of analysis can provide morphological and structural data but does not provide surface sensitive information and is limited to thin samples.[42] The development of SEM in the 1940s used detectors mounted on the same side of the sample as the electron source.[43] These detectors image electrons that are not transmitted but instead backscattered or secondary to the incoming beam, providing images that are reflective of a sample surface rather than the whole. Rapid developments in detectors, vacuum pump technologies, emission sources, aberration correctors, and electronic amplification systems (enabled by the transistor) allowed SEMs to be commercially used by 1965.[42] The commercial availability of the SEM provided a variety of scientific fields with a new method of analysis. Further improvements allowing the ability to look at structure and composition in tandem make this tool particularly powerful for the study of cultural heritage.

SEM has been used to study cultural heritage since the 1960s because of its commercial availability and versatility. As a non-destructive technique for many inorganic samples, SEM, paired with energy dispersive X-ray spectroscopy (EDS) for compositional analysis, has been used to study provenance, technology and technique of artifact manufacture, historical use, and degradation processes.[42] These studies help to form a scientific basis for understanding history, art history, archaeology, restoration and conservation, as well as determining authenticity.[44] More recent advancements in electron microscopy have aided study in areas where samples are easily damaged by the electron beam or are otherwise difficult to analyze. For example, two techniques, environmental SEM (ESEM) and low voltage SEM (LVSEM) are now being widely used for biological samples and for cultural heritage materials that would be sensitive to the electron beam. TEM has also been utilized to study structure and composition for cultural heritage materials, albeit less widely than SEM because of the sample preparation necessary and the limited analysis area.

The ability to study nanoscale structure and composition of cultural heritage with electron microscopy has revealed how humans have interacted with nanotechnology in the past. While the field of nanotechnology has only been in existence since the 1980s, humans have fabricated nanoscale materials since the Final Bronze Age (1200-1000 BC). Glass fragments and beads found in northern Italy mark the only known center of glass-making technology during the Bronze Age. The origin of red pigment in these glasses comes from the surface plasmon of copper particles that were dispersed at the surface of the glass.[45] These metallic particles could only be created through careful control of reductive/oxidative processes, showing that this region was advanced in its glass-making technology. While this is currently the earliest known source of nanotechnology, the chemistries used in this process became widespread as a method to color both glass and ceramics. Copper nanoparticles have been found in glasses and ceramics across the world from ancient Celtic, Roman, Japanese, and Chinese cultures.[46]

The unique properties of nanomaterials are what make certain artifacts curious to researchers today. The reductive and oxidative control necessary to create nanoparticles in glass as dyes was mastered by craftsmen in the Roman empire and spread to other areas of the world. Mastery of the technique produced examples like the Lycurgus Cup, a rare piece of craftsmanship that exhibits a dichroism effect thanks to the inclusion of nanoscale gold and silver alloys.[47] In direct light, the cup appears a greenish jade color, but becomes ruby colored when light is transmitted through the glass.

The Lycurgus cup is an example of a specimen that required the development of nanocharacterization techniques to be understood. In the 1950s, small samples of the glass were examined using elemental analysis, with the goal of understanding what pigment was responsible for the unique color effect. The glass was determined to be primarily soda-lime silica glass, contained 0.5% Mn, and also included a variety of trace elements including Au and Ag. It was hypothesized that the color effect came from colloidal gold, but ultimately that the effect came from careful control of conditions during fabrication.[47] By the 1960s, attempts to recreate the color added empirical evidence to reinforce the idea that the coloration was indeed due to nanoparticles, but these studies were unable to determine the percentages of Au and Ag, whether these were separate phases, alloys, or even determine the size of the particles. It wasn't until the late 1980s that the glass was examined again, this time with TEM.[48] TEM, paired with X-ray analysis, revealed that the particles were indeed Au/Ag alloys, ranged from 50-100 nm in size, and contained a small percentage of Cu. Understanding that it was not just the composition, but the structure of the nanoparticles in the glass that caused the unique color changing properties led to breakthroughs in understanding how the glass was fabricated, why it was difficult to reproduce, and also aided in modern recreation of dichroic glass.

The Lycurgus cup is a rare example of exquisite nanotechnology from history, but it was an anomaly during its time and empirically difficult to recreate. Other examples of nanoparticles as optical pigments, like those found in lusterware, were recreated to a high degree of accuracy. While most of lusterware was created using the same elements – copper and silver – a high variation in color, shine, and depth comes from the manufacturing process, allowing control of the size, distribution, and shape of the nanoparticles in the glaze.[46] The variety of colors found in lusterware are attributed to the plasmonic properties of the nanoparticles, and good models have been created to describe color based on the size, composition, and density of the particles in the glassy matrix. From the spatial and size distributions, clear differences in manufacturing techniques can be found between different production sites around the world. The ways that the metallic nanoparticles are distributed and organized throughout the glazes suggest that high empirical control was used by ceramic manufacturers. There is good evidence to support that, while craftsmen did not realize that nanoparticles were the origin of the color in their glazes, the syntheses that they had were well controlled to exploit the optical properties nanoparticles have to offer.

The ability to understand the curious properties exhibited by historic artifacts has not just revealed information about human history and historic manufacture of materials but has inspired research into new technologies. The glazes and glasses colored by nanoparticles and the curious dichroism of the Lycurgus cup were the earliest examples of metamaterials and have had a role in inspiring work towards manipulating light for cloaking devices.[49,50] Another pigment used in pre-Columbian Mesoamerica, Maya blue, has remained vibrant and stable throughout time, despite exposure to acidic or alkaline conditions and even to a variety of solvents.[51] The technique to make this pigment has since been lost, but upon analysis, it was found to be an organic/inorganic hybrid material formed from the combination of clay with indigo. The clay itself is less chemically resilient than the pigment and exhibits a fibrous structure with pores between 1-2 nm in diameter. The indigo molecules chemically bind within the pores of the clay, creating a synergistic material exhibiting both enhanced stability and vibrant color. The structure of the material leads to the resilient properties of Maya blue and has inspired researchers to study similar structural systems to create long-lasting, sustainable dyes and high durability coatings.[52,53] In a final example, Damascus steel blades produced in the 17th century were prized for their strength, sharp edges, and shatter resistance. Investigations into the structure of the material revealed that these qualities were imparted by carbon and Fe_3C nanotubes and Fe_3C microspheres within the steel.[54] The method of manufacture of these blades was lost in the 1800s, but the ability to understand the structure has led to a rediscovery of the process that created these nanostructures in the steel.[55] The ability to strengthen materials through the use of nanoparticle or nanotube additives mirrors many of the efforts to improve material strength using nanocomposites today.

Structure determines property, and the ability to understand and manipulate structure allows us to control properties. From the examples above, it is clear that studying the curious properties in cultural heritage materials can lead to surprising information about structure, which in turn leads to information about synthesis and manufacture. Ultimately, these studies provide new insight into technologies that can be adapted for creating better or more sustainable materials in the future. The ways in which humans have used and made materials in the past impacts how we use and make materials today. The ability that we now have to see nanoscale structure and investigate composition with characterization techniques like SEM and TEM has revealed that nanotechnology is *ancient* technology, even though human understanding of how nanoscale structure affects properties is a 20th century phenomenon.

The final study (Chapter VI) in this dissertation provides an example of how FIB prepared samples and scanning TEM (STEM), a technique developed for modern nanotechnology and used widely in the semiconductor industry,[56] can be applied to the study of cultural heritage. In particular, it is used to examine nanoscale structure and composition not on an ancient artifact, but on architectural stone from a historic building. This analysis better informs the formation process of a naturally occurring metal oxide that is discoloring the surface of the stone. This work, similar to other work in cultural heritage, has impacts beyond just history and preservation/conservation, but has the potential to impact fields like astrobiology and geology. Experiments in this work were performed by me and Edward Vicenzi, who also conceptualized the basis for this work. This chapter is being prepared for publication, written by me with editorial assistance from Edward Vicenzi and Carol Grissom. Studying and preserving materials from our past impacts not just our understanding of history, but also our trajectory into the future. The future that we are imagining today will someday become the history we protect, telling the story of how humans are more connected through time – and through our use and creation of materials – than we might first suspect.

Bridge to Chapter II

The study in Chapter II describes the role of the electron beam as an important reagent in the patterning reaction for electron beam lithography. Here, reducing the accelerating voltage used to pattern a high-resolution inorganic thin film electron beam resist, $HafSO_x$, dramatically decreases the dose required to pattern sub-10 nm lines, increasing sensitivity of the material without loss in contrast. High resolution patterning at 10 keV shows no decrease in obtainable feature size, producing 9 nm wide lines with half the dose required previously and with no increase in line edge roughness. Monte Carlo simulations predict that even lower primary beam energies, down to 5 keV, could enable patterning of sub-20 nm features with significantly enhanced throughput.

CHAPTER II

SUB-30 KEV PATTERNING OF HAFSOX RESIST: EFFECTS OF VOLTAGE ON RESOLUTION, CONTRAST, AND SENSITIVITY

Reprinted with permission from Fairley, K. C.; Sharps, M. C.; Mitchson, G.; Ditto, J.; Johnson, D. W.; Johnson, D. C. Sub-30 keV Patterning of $HafSO_x$ Resist: Effects of Voltage on Resolution, Contrast, and Sensitivity. *J. Vac. Sci. Technol. B.* **2016**, *34*, 041607. Copyright 2016, American Vacuum Society.

Introduction

Improvements in scanning electron microscope (SEM) technology have led to overall performance enhancements across a broad range of common accelerating voltages, including those less than 5 keV.[1] The use of magnetic immersion lenses and stage deceleration have significantly reduce the impacts of aberrations associated with low energy (1-5 keV) beams.[2] This has been vital for studying biological samples in which beam damage is a serious concern. Modern cold-field emission sources, monochromators, and better lenses have improved the low-energy beam performance even further.[1] These performance enhancements have led to an explosion of SEM use in the biological world, in which beam damage at high voltages has traditionally been a limiting factor.[3] More recently, these advances have been applied to electron beam lithography.[3,4,5]

Electron beam lithography (EBL) performed using an SEM operating at high accelerating voltages, 30 keV and above, has been used extensively for the patterning of densely packed features with critical dimensions less than 10 nm.[6] High accelerating voltages reduce the spot size of the beam and penetrate deep into thick, dense films to fully expose them.[7] Significant work has been done to optimize the chemistry of the EBL resists for enhanced sensitivity at these voltages.[6] However, high accelerating voltages create several problems for EBL that are exacerbated with the use of thin (tens of nm) films. A significant portion of the energy of the beam passes through the resist and is buried deep in the substrate instead of reacting with the resist.[8] These electrons heat and damage the sample directly beneath the beam and diminish lateral resolution due to long-range proximity effects from secondary electrons.[9] It has been shown in several high resolution resists that decreasing the accelerating voltage leads to an increase in the sensitivity of the target resist.[8,10,11] Due to the enhanced sensitivity, the time required to pattern the resist is dramatically decreased, enabling patterning of larger, more intricate structures while avoiding vacuum damage through drying or condensation effects in sensitive films. If the beam energy is reduced too much, however, the beam interaction volume may become smaller than the film thickness. This is a problem for full exposure, but has been shown to lead to interesting 3-D stepped structures in positive tone resists.[12] For thin inorganic resists, this suggests that reducing the accelerating voltage to an optimal value may lead to a substantial decrease in patterning time with full resist exposure and minimal impact on lateral resolution.

In this work, we investigate the patterning sensitivity and contrast of $\mathrm{HafSO_x}$,[13–16] a negative-tone inorganic electron beam resist, at primary beam energies of 2-30 keV, and the lateral resolution of the resist by patterning at 10 keV. $HafSO_x$ was chosen as a model inorganic resist because films of this resist are thin, dense and laterally homogeneous. Consistent with reports for other thin inorganic resists, the sensitivity of $HafSO_x$ increased dramatically as the beam energy decreased. We were able to use a 10 keV beam energy to produce sub 10 nm lines without any loss in line edge roughness using only half the dose required at 30 keV. Monte Carlo simulations predict sensitivity enhancements with decreased beam energy in good agreement with our experimental observations. The simulations also suggest that patterning at beam energies less than 10 keV may still enable patterning of sub-20 nm feature sizes or better as film thickness decreases. This work has implications for improving the throughput of EBL with existing thin inorganic resists while maintaining high lateral resolution.

Experimental

$HafSO_x$ Film Preparation

A 1 M stock solution of $HfOCl_2 \cdot 8H_2O$ (Alfa Aesar) was prepared by dissolution and dilution with 18 MΩ nanopure water. Solutions for spin coating were prepared by mixing 2 N H_2SO_4(aq) (VWR) and 30 wt% H_2O_2(aq) (EMD Millipore) followed by the addition of $HfOCl_2$(aq). The final solution was diluted using 18 MΩ water to a concentration of 0.105 M sulfuric acid, 0.45 M hydrogen peroxide, and 0.15 M hafnium. N-type, Sb-doped silicon substrates (0.008-0.02 Ω-cm) received surface treatments using a MΔRCH cs-1701 plasma cleaner running on O_2 plasma at 30% O_2 in N_2 using 150 W for 60 s immediately before spin coating. To obtain more reliable ellipsometry measurements, 100 nm thermally grown oxide silicon substrates were used and treated with SC1 (5 parts 18 MΩ water, 1 part 29% ammonium hydroxide, 1 part 30% hydrogen peroxide) at 80 °C for 30 minutes before plasma cleaning. Films were prepared by filtering the solutions through a 0.45 μm filter and then spin-coating at 3000 rpm for 30 s. The HafSO$_x$ thin films were then subjected to a one minute anneal at 80 °C as a soft bake to densify the films.

Exposure for Dose Arrays

HafSO$_x$ films prepared as described above were patterned in an FEI Helios 600i DualBeam either manually or by using FEI's automation program, iFast. Arrays of 200x200 μm^2 boxes spaced 400 μm apart were patterned with accelerating voltages of 2, 5, 10, 20, or 30 kV at a pitch of 60 nm and a dwell time of 100 ns. The number of beam passes across a pattern controlled the dose,

$$Dose = \frac{N \times I \times t}{p_x^{\ 2}} \qquad (1)$$

where N is the number of passes, I is the beam current in μA, t is the dwell time in s, and p$_x$ is the pitch in the X and Y directions, measured in cm. The beam current was measured prior to each experiment using a Faraday cup standard. Films were developed at room temperature in 25 wt% tetramethylammonium hydroxide (TMAH, Alfa Aesar) for 1 min and thoroughly rinsed with 18 MΩ water, followed by a post development hard bake at 300 °C for 3 min.

Ellipsometry Measurements

Data was taken on a J.C. Woollam VASE Ellipsometer with focusing probes installed to reduce the ellipsometric spot size to 60 μm. Each patterned box was measured at three angles, 55°, 60°, and 65°, with 8 second acquisitions at each angle. The resist was modeled as a Cauchy film on 100 nm SiO$_2$. All measurements had an MSE value below 10. The squares patterned with doses below the turn-on dose allow the contrast and sensitivity to be calculated by the number of partially patterned squares. A trend line is drawn between the points that lie between a normalized thickness of 0.2 and 0.8, with 1 being completely patterned, striking the x-axis at d_0 and providing a y value of 1 at d_{100}. The slope of the trend line is used to calculate the contrast of the resists and d_{100} is defined as the sensitivity.

Exposure for Resolution Arrays

HafSO$_x$ films were prepared as described above and patterned using an FEI Helios 600i DualBeam. A 10 keV beam with a current of 7.7 pA was used to pattern high resolution line arrays. An objective immersion lens, which immerses the sample in a magnetic lens field, was applied to sharpen the electron beam spot size even further and allow for better resolution. To focus the beam without exposing the resist or moving the stage from the target location, a 2 μm tall platinum-carbon pillar 50 nm in diameter was created by using the electron beam to decompose a platinum-containing gas precursor, MeCpPtMe$_3$. Individual platinum grains were used to confirm the final focus and stigmation without exposing any of the surrounding material. The horizontal field width was set to 61.4 μm, and the pattern was then generated from a bitmap using iFast. The pitch, set by the bitmap pixel size, was set at 10 nm, but only a single pass per line was used to allow for the highest resolution.

Line Width and Edge Roughness Measurements

Following exposure, the resolution arrays described above were developed using the same procedure as described for the dose arrays and subsequently imaged with the SEM. High magnification, high resolution images were obtained (1.484 pixels per nm) and analyzed using the freely available ImageJ software. The images were converted to binary format, and the average line widths for six of the lines in the array were obtained over a 700 nm length of each line. The line width roughness was calculated as three sigma of the standard deviation in the line width measurements for each line. The reported average line width and line width roughness were calculated by averaging the values obtained for each line. The line edge roughness was calculated in a similar fashion. The top and bottom edge positions were determined for each line, then the top and bottom line edge roughness was calculated as three times the standard deviation in the line edge position. These values were then averaged for each line. The line edge roughness we report was obtained by averaging the line edge roughness measurements for all six distinct lines.

Monte Carlo Simulations

We calculated the point spread functions ("PSFs") of 2, 5, 6, 10, 20, and 30 keV primary beam energies in 22 nm thick soft-baked HafSO$_x$ films using the Monte Carlo software CASINO v3.2.0.4.[17] The PSFs represent the implanted energy distribution in the resist as a function of radial distance from the beam irradiation spot.[8] We initially assumed an unexposed film density of 4.3 g/cm^3, with a 100 nm SiO$_2$ (1.74 g/cm^3) layer and an infinitely thick Si substrate beneath the resist. We also tested a range of film thicknesses (20 – 24 nm) and densities (4.0 – 4.6 g/cm^3) at each energy in order to understand how the simulation results might change with potential experimental variations. All simulations were conducted using a 1 nm beam spot size and 100,000 electrons. The beam PSFs were calculated from the implanted energy distributions summed radially over the depth of the resist layer. The default electron-sample models in the software were used.

STEM Imaging

Cross-sectional images of developed HafSO$_x$ lines were acquired using high-angle annular dark field imaging in a scanning transmission electron microscope (HAADF STEM, FEI Titan, 300 kV incident beam). The specimens for cross-sectional imaging were prepared using Ga$^+$ focused ion beam (FIB) milling and following a procedure similar to the Wedge-prep method described by Schaffer et al.[18]

Results and Discussion

Arrays of 200 μm squares were patterned in HafSO$_x$ using doses from 1 μC/cm^2 to 1 mC/cm^2 and accelerating voltages from 2 keV to 30 keV to determine the turn-on dose in the resist at each voltage. Planar SEM images (see Figure 2.1 for an example) were used to identify the approximate turn-on dose for the resist by observing when patterned material no longer remained after development. The images showed no defects, such as voids or ridges in the exposed films, which ensures accuracy in the ellipsometry measurements used to quantify the thickness of the films to determine sensitivity and contrast. Several arrays were also created using an immersion lens to confirm there was no impact on the sensitivity when high-resolution patterns were created. The patterned square edge length was reduced to 80 μm for these arrays due to a reduction in the maximum horizontal field width allowed with the immersion lens active. The immersion lens did not impact the sensitivity or contrast when patterning the resist.

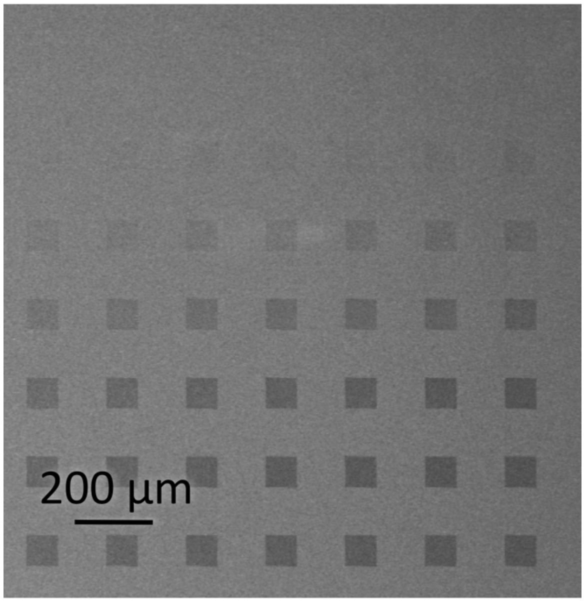

Figure 2.1. SEM back scattered electron image of an example dose array on SiO_2 post-development. Each square represents a different electron beam dose, increasing from top left to bottom right. Darker squares indicate thicker films as more of the $HafSO_x$ film condenses.

The sensitivity and contrast are both excellent measures of the quality of a resist. Films with high sensitivity require less energy and time to pattern, allowing for patterning using instruments that are more economically accessible. Films with high contrast enable close packing of patterned features and sharp sidewalls due to the high separation between patterned and non-patterned material. The completely patterned squares are 9 nm thick and give a baseline for sensitivity calculations. The experimental d_{100} value linearly decreases with decreasing accelerating voltage, as shown in Figure 2.2, indicating a much higher resist sensitivity at low accelerating voltages. At 2 keV the time required for full resist exposure is almost an order of magnitude less than at 30 keV, the beam energy at which high resolution lines in $HafSO_x$ were previously reported.[13]

At all accelerating voltages, the contrast values are greater than two. The contrast initially decreases as the accelerating voltage used to pattern the material decreases at 10 keV, but the contrast then recovers at 2 keV. This could be due to the tradeoff from losing the narrow "neck" of the interaction volume at high voltages and reducing the entire interaction volume into the thin film. In the middle where the contrast decreases, the interaction volume is in a regime that gains no benefit from the narrow interaction volume "neck" or from complete confinement of the volume in the thin film. (Figure 2.2)

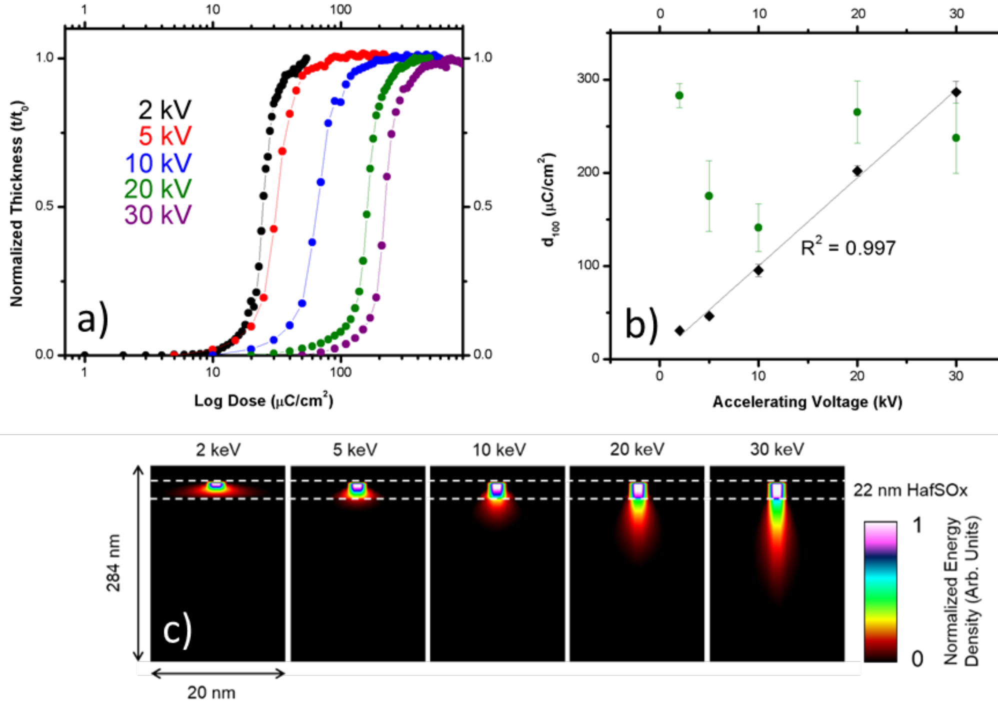

Figure 2.2. a) Plotted contrast curves for varying accelerating voltages and b) the dependence of contrast and d_{100} on accelerating voltage. c) Modeled interaction volumes for the corresponding voltages showing the retraction of the "tear drop" into the film. Note that the scales of the x- and y-axes are unequal.

While high sensitivity and high contrast are important requirements for an E-beam resist, the ability to pattern at high resolution is essential in order to outperform the myriad of well-established low resolution organic resists. To understand the interaction volume of the beam used to pattern the contrast curves and gain insight into the resolution, Monte Carlo simulations were used to model secondary electrons within the film and substrate. As expected from previous results with other resists,[8,11] decreasing the accelerating voltage leads to the containment of more electrons within the resist. To further grasp how the beam energy at different voltages is implanted radially within the film, PSF analysis was used. The normalized PSFs of the beam for 2, 5, 10, 20, and 30 keV primary beam energies are shown in Figure 2.3. Integrating the area under each unnormalized PSF provides an estimate for the total amount of energy deposited in the resist, from which the PSF could be normalized to the total energy deposited in the resist by that beam. Because the sensitivity of the resist changes greatly with primary beam energy, this allows a more accurate comparison of how the energy is distributed radially throughout the resist.

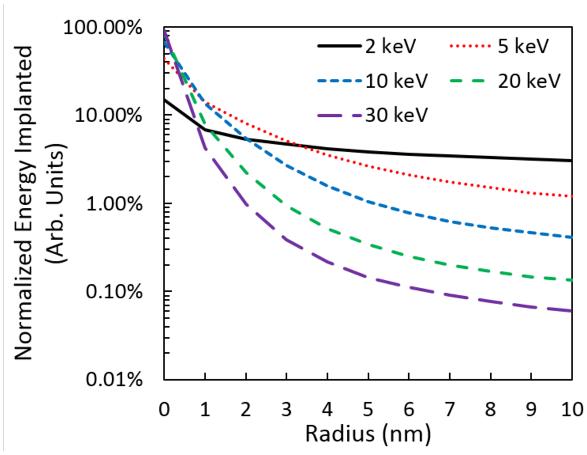

Figure 2.3. Simulated normalized PSFs for 2, 5, 6, 10, 20, and 30 keV primary beam energies in a 22 nm thick $HafSO_x$ resist.

In Figure 2.4, we show the sensitivity enhancement relative to 30 keV calculated from our simulations and from our experimental data from the turn-on dose curves. The trend in our simulation results is similar to the trend in our experimental observations: the resist sensitivity increases at an increasing rate as the beam energy decreases. For beam energies 10 keV and greater, the simulated and experimental data match closely where there is little beam spread. At lower energies, the theoretical and experimental data start to differ. This may be due to the effective dose applied during the simulation. For 100,000 electrons landing within a 1 nm spot, the applied dose is 1.02 x 10^6 μC·cm^{-2}, about three orders of magnitude larger than the range of d_{100} values for energies investigated experimentally. The large number of electrons is necessary for accurate Monte Carlo performance, but leads to excessively large applied doses, especially for the lower accelerating voltages. Furthermore, the simulations do not take into account the cross-linking, oxygen evolution, and other chemical changes that occur within the resist layer during lithographic exposure[19] but rather assume the film density and thickness do not change. Thus, while the simulation sensitivity enhancement shows qualitatively the same trend as observed in the experimental data, it is not surprising that the exact values differ.

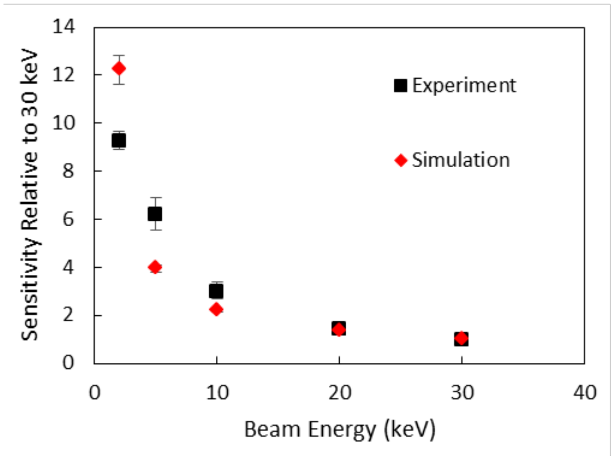

Figure 2.4. Simulated and experimental sensitivity enhancement as a function of beam energy, relative to 30 keV. For the experimental data points, the error bars reflect the uncertainty in the calculation of d_{100}. For the simulated data points, the error bars reflect the sensitivity of the model to small changes in film thickness and composition relative to the assumed values.

The normalized PSFs in Figure 2.3 also give some indication of the possible lateral resolution that could be achieved as the beam energy is decreased. As expected, the energy deposited by a 30 keV beam is deposited within a very narrow region through the resist. As the beam energy is decreased, the width of the region in which energy is deposited increases. We expect the area in which the majority of the beam's energy is deposited will correlate with the area in which the film is actually exposed. The width of the exposed region does not scale linearly with beam energy but increases rapidly as the beam energy is decreased below 10 keV. Our average line width measurements (vide infra) indicate that at 10 keV the exposure radius of the beam is approximately 4 nm. From our simulations, this radius corresponds to approximately 99% of the total energy deposited in the resist by the 10 keV beam. Assuming that 99% of the deposited energy corresponds to the threshold between patterned and non-patterned resist at other beam energies as well, the simulation results imply that even a 5 keV primary beam may enable patterning of sub-20 nm features with a 4-6x reduction in patterning time relative to patterning at 30 keV.

To test the resolution of $HafSO_x$ at low accelerating voltages, line arrays were created with varying pitch. When patterning with small horizontal field widths, three artifacts produced by the limitations of the instrumentation arose that impeded high-resolution measurements. As a result, we could only test the lateral resolution using a 10 keV or greater beam energy. At 10 keV, high resolution lines were produced with line widths of 8.9(3) nm spaced 35 nm apart, as shown in Figure 2.5. The dose used to create these lines was 488 $\mu C/cm^2$, resulting in a nearly twofold reduction in the time previously required at 30 keV to create the same patterns. As measured from a plan view image, the line width roughness of the 8.9(3) nm lines was 2.5(3) nm and the line edge roughness was 2.6(3) nm, very similar to previously reported 30 keV patterning of $HafSO_x$.[13] These results show that high-resolution lines can be patterned using accelerating voltages less than 30 keV in less time while maintaining the same low roughness and critical dimensions.

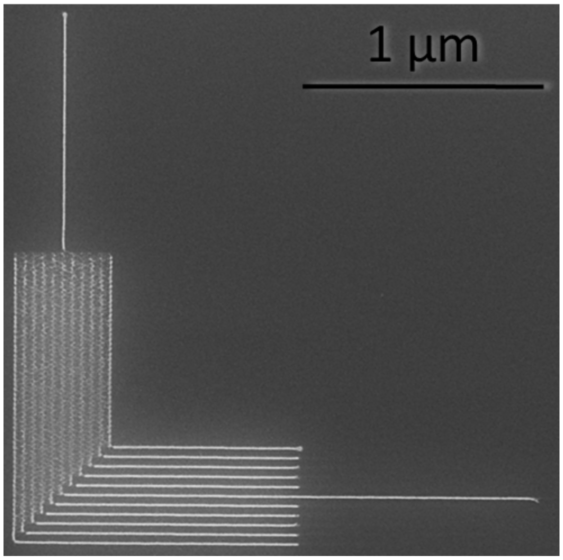

Figure 2.5. SEM image of patterned 9 nm $HafSO_x$ lines spaced 35 nm apart at 10 keV on a Si substrate with native oxide. One line was extended to check that the maximum resolution does not change with close packing of the lines.

After obtaining plan view images of the lines to obtain the line edge and width roughness, cross-sectional STEM gave further supporting measurements of the line height and width. HAADF-STEM images (Figure 2.6) of a line array patterned at 10 keV show the height of each HfO_2 line, 9 nm, is identical to the film thicknesses determined for the dose arrays after exposure and development using ellipsometry. The images also show an approximately 8.5 nm full width at half maximum (FWHM) for the lines. There is a 1-2 nm residual film between each of the lines that remains after processing, as was seen in prior $HafSO_x$ studies.[13] The lines are spaced 30 nm apart from each other in an array of 11 lines, giving tight packing along with the high resolution. However, the moderate contrast leads to rounded edges instead of an ideal top hat shape. The contrast curves indicate that 10 keV accelerating voltage should produce the lowest resolution lines with the highest roughness. This is most likely due to the fact that it does not have as small a spot size nor as small an interaction volume seen at higher and lower voltages, respectively.

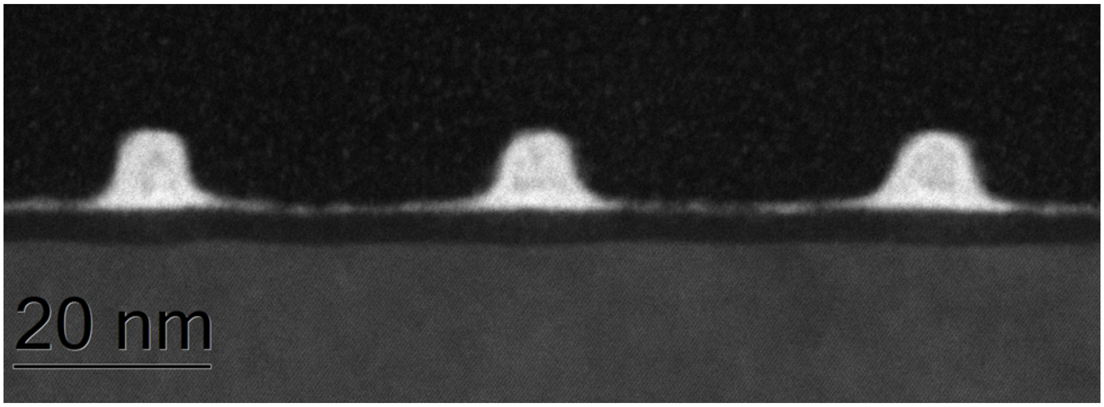

Figure 2.6. STEM cross-section images of high-resolution lines patterned using 10 keV primary beam energy.

For a 22 nm thick $HafSO_x$ resist, 10 keV beam energy appears to provide an acceptable compromise between high-resolution patterning and increased resist sensitivity. At very low beam energies, such as 2 keV, the lateral resolution is expected to be much worse than at 30 keV because more lateral scattering of the primary beam occurs in the resist. However, a 1-2 keV beam may still enable high resolution patterning in thinner resists (thicknesses around 5 nm from our simulations), where only the “neck” of the interaction volume is in the resist.

Since inorganic resists, such as $HafSO_x$, can be spin coated to varying thicknesses, we also simulated the effects of resist thickness using a 10 keV incident beam (Figure 2.7). Decreasing the resist thickness provides an effect similar to increasing the primary beam energy. More of the energy is deposited immediately in the vicinity of the beam irradiation spot for a thinner resist than for a thicker resist. However, decreasing the resist thickness also leads to less total energy deposited in the resist and a corresponding decrease in the resist sensitivity. These results imply that as inorganic resists are made thinner, the ability to use lower accelerating voltages, which enables faster processing, becomes more feasible without any loss in resolution.

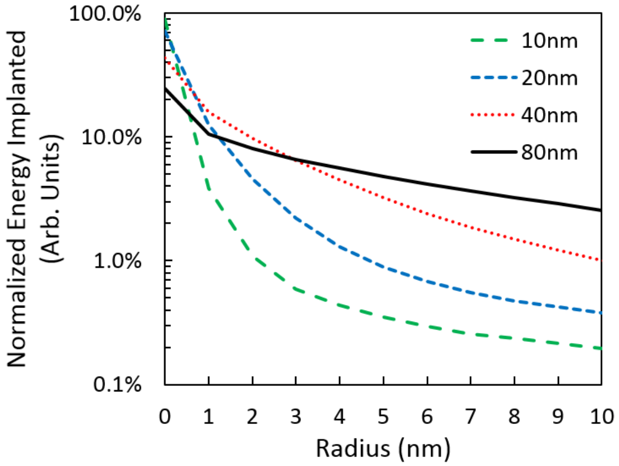

Figure 2.7. Percentage of total energy deposited in the resist as a function of radius from the beam irradiation spot for HafSO$_x$ films of different thicknesses.

Conclusions

With modern advances in microscopy, accelerating voltages less than 30 keV can still enable high resolution and low roughness in the patterned thin inorganic E-beam resists. Our experimental results show that reducing the accelerating voltage of the primary beam to 10 keV or less dramatically increases the sensitivity of a HafSO$_x$ resist and still enables high-resolution patterning. Sub 10 nm lines were produced using 10 keV in half the time required at 30 keV. Our simulations indicate that the resist sensitivity increases strongly as the primary beam energy is reduced, in good agreement with our experimental observations. Additionally, our simulations indicate for a 22 nm thick

$HafSO_x$ resist, 10 keV appears to provide a compromise between good lateral resolution (sub-10 nm) and high throughput (2-3x relative to 30 keV patterning). Further reductions in process time may be achievable once hardware challenges are overcome. These results suggest that rather than maximizing the voltage of the incoming electrons, it is better to match the energy required to penetrate only as deep as the thickness of the resist.

Bridge to Chapter III

In lithography, low-energy patterning has been limited by shallow electron penetration into resist films. The use of thin films can reconcile this issue, but many resists are not etch resistant to further processing steps when applied in thin layers. The development of inorganic thin film resists has mitigated this issue. We have shown here that thin inorganic cluster resists can maintain sub 10-nm resolution at 10 kV accelerating voltages, previously only achieved at 30 kV voltages. Below 10 kV, however, resolution performance rapidly fails due to beam spreading.[20] With advances in instrumentation, the use of a deceleration stage, or retarding field, can theoretically maintain resolution while increasing sensitivity of a given thin-film resist. Beam deceleration is a common technique used for imaging samples that are sensitive and require low accelerating voltages in order to reduce sample damage. By doing so, the effective energy that reaches the sample is reduced, but the electron signal received from backscattered or secondary electrons is greater due to interactions with the higher incoming beam energy.[21] It is possible to improve image resolution at low voltages by using a higher accelerating voltage and applying a bias to the stage and the sample. Monte Carlo simulations predict that the sensitivity of a 6 kV beam can be achieved while maintaining the resolution of a 10 kV beam with the use of a properly functioning deceleration stage. This demonstrates that advancements in instrumentation have the ability to directly influence performance in device fabrication.

Instrumentation is a vital component in lithography applications, as electrons constitute one of the reactants when creating patterns. The other reagent is the resist, the material that interacts with electrons to undergo a change in solubility. Through the examination of crystal structures, Chapter III explores the choice of resist materials, and how understanding their structures may impact reactivity. In this chapter, a series of five organotin carboxylate clusters of the type $[RSn(O)O_2CR']_6$ containing *n*-butyl ligands and carboxylates ranging in size from formate to diphenylacetate were synthesized and examined by single crystal X-ray diffraction. The crystal and packing structures of each compound were compared with regards to the steric and intermolecular forces of the varying carboxylate groups in order to aid the understanding of how these same factors relate to irradiation trends in EUV lithography of thin films. The trends found are compared to other factors that may also dictate resist formation in order to elucidate a fuller picture of the chemical transformations that occur when patterning inorganic materials.

CHAPTER III

IMPLICATIONS OF CRYSTAL STRUCTURE ON ORGANOTIN CARBOXYLATE PHOTORESISTS

Reprinted with permission from Sharps, M. C.; Marsh, D. A.; Zakharov, L. N.; Hutchison, J. E.; Johnson, D. W. Implications of Crystal Structure on Organotin Carboxylate Photoresists. *Cryst. Res. Technol.* **2017**, *52*, 1700081. Copyright 2017, WILEY-VCH Verlag GmbH & Co.

Introduction

Organooxotin cluster chemistry has been widely studied since the early 1920s,[1–8] with a variety of discrete cluster species existing in the literature. In particular, organotin carboxylate clusters exhibit a wealth of structural diversity,[9–11] with many derivatives finding application as organic-inorganic hybrid materials,[12,13] catalysts,[14,15] anti-fungal agents,[16] and anti-tumor agents.[17,18] Recently, a few of these compounds have been evaluated as next-generation thin film inorganic photolithographic resists the electronics industry. Tin clusters have shown promise as extreme ultraviolet (EUV) resists because of the high absorption cross section of tin in the EUV, superior etch selectivity compared to traditional photoresists, and improved critical dimensions resulting from shorter diffusion pathways in the material.[19–22] The mechanism of cross-linking of these materials when exposed to EUV sources has been attributed to decomposition mechanisms of the organic ligands stabilizing the tin centers,[19] however, the extent to which the organic ligand identity affects the sensitivity of the subsequent film remains elusive. In studies of a tin cluster, $[(RSn)_{12}O_{14}(OH)_6]O_2CR'_2$, where the carboxylate acts as a counteranion,[19] and the tin monomer, $R_2Sn(O_2CR')_2$, where the carboxylate is covalently bound,[21] it has been reported that the homolytic bond strength of the tin-alkyl chain bond has a significant impact on the radiation sensitivity of the resulting film, but that the carboxylate ligands only loosely correlate to sensitivity through the extent of molecular weight.

Here, we present a systematic study of the single crystal structures and crystal packing of five organotin clusters of the general formula $[n\text{BuSn(O)O}_2\text{CR}]_6$ (Scheme 3.1) in an effort to understand how varying the structure of the carboxylate group affects the cluster-to-cluster interactions, and subsequently, how these interactions may affect the sensitivity of the resulting organotin resist. We also discuss other factors that may influence the patterning chemistry, including the homolytic bond strengths of the carboxylates. While we realize that the crystallization of these clusters does not provide a perfect analogy to cluster interactions in thin films, examining the crystal structure and packing provides insight into the intermolecular interactions at play between the clusters that are still expected to have an impact on the films. By taking a molecular approach to understanding cluster interactions and reactivity, we identify multiple factors that may impact the ability of these clusters to crosslink and form the insoluble network required for a negative-tone resist. We intend in future work to explore experimentally how these factors relate to the sensitivity of thin-film resists as well as final film properties.

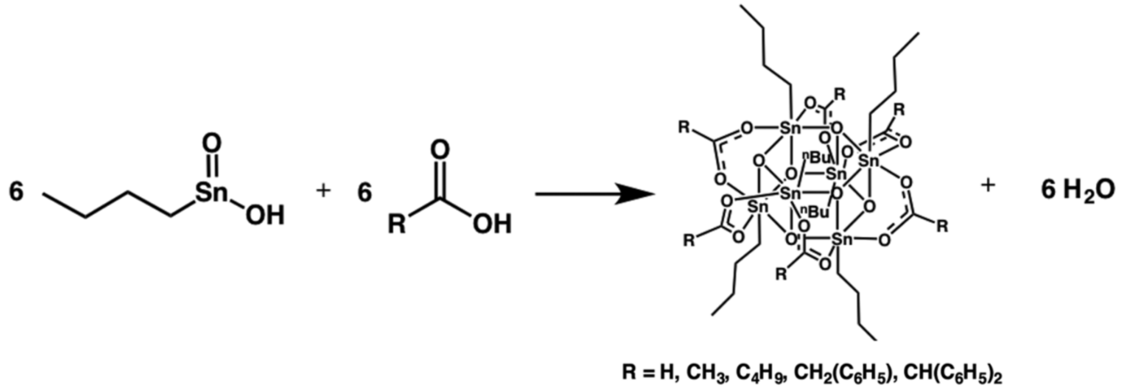

Scheme 3.1. Generic reaction scheme for the formation of tin cluster species $[n\text{BuSn(O)O}_2\text{CR}]_6$ from a condensation reaction of butylstannoic acid with a carboxylic acid. Carboxylate R groups are ordered below the drum structure in order of increasing steric bulk. Carboxylate groups: formate, acetate, pivalate, phenylacetate, and diphenylacetate.

Experimental

General

All reagents and chemicals were obtained from commercial sources and used without further purification. All reactions are modified from literature methods to accommodate the carboxylic acids used herein.[2,5,23–25] In all cases we used a slight molar excess of carboxylic acid, and variability in reaction times were modified based on yields. ^{1}H and ^{119}Sn {^{1}H} NMR spectra were obtained on a Bruker Avance III-HD 600 spectrometer (600.02 MHz for ^{1}H and 223.61 MHz for ^{119}Sn {^{1}H}) in $CDCl_3$ at 25 °C. Proton resonances are referenced to tetramethylsilane, while tin resonances are referenced to tetramethyltin (external standard). Infrared spectra were recorded using KBr pellets on a Thermo Scientific Nicolet 6700 FT-IR. All IR spectra, proton, and tin spectra can be found in Appendix B.

X-Ray Crystallography

Diffraction intensities were collected at 200 K (**1** and **4**) and 173 K (**2**, **3** and **5**) on a Bruker Apex2 DUO CCD diffractometer using MoKα radiation, λ= 0.71073 Å (**1**, **3**, **4** and **5**) and CuKα radiation, λ= 1.54178 Å (**2**). Absorption corrections were applied by SADABS.[23] Space groups were determined based on systematic absences (**2** and **5**) and intensity statistics (**1**, **3** and **4**). Structures were solved by direct methods and Fourier techniques and refined on F^2 using full matrix least-squares procedures. All non-H atoms were refined with anisotropic thermal parameters except C atoms in the disordered toluene molecule in **4,** which were refined with isotropic thermal parameters. All H atoms were refined in calculated positions in a rigid group model. All diffraction data for Mo source were collected up to $2\theta_{\max} = 56.0°$, but only reflections with $2\theta_{\max} = 48.0$ and $50.0°$ have been used in the final refinement respectively for **5** and **3**. However, it provides appropriate number of reflections per number of refined parameters; 7932/592 (**5**) and 6428/365 (**3**). Besides the main molecules, the structures of **1**, **2** and **4** have additional solvent toluene molecules. Some terminal $–CCH_2CH_2CH_3$ and $–C(CH_3)_3$ groups and solvent toluene molecules in these structures are disordered over two positions. The disordered fragments were refined with restrictions; the standard bond distances have been used in the refinements as the targets for corresponding bonds. All calculations were performed by the Bruker SHELXL-2014/7 package.[24]

Synthesis

Hexameric n-Butyloxotin Formate $[nBuSn(O)O_2CH]_6$ (1). Butylstannoic acid (1.09 g, 5.20 mmol) was added to 50 mL of toluene under N_2. To this, formic acid (0.22 mL, 5.8 mmol) was added and the solution refluxed for 24 hours. During this time, solvent and water were removed using a Dean-Stark apparatus and the reaction flask was refilled with toluene as necessary. The resulting reaction mixture was centrifuged and the supernatant was left to evaporate. The resulting white powder was dissolved in toluene, filtered, and recrystallized through slow evaporation (yield 297 mg, 24.2%). IR (KBr) cm^{-1}: 2956 (m), 2927 (m), 2902 (m), 2871 (m), 1627 (s), 1568 (s), 1385 (s), 1368 (s), 619 (m). ^{1}H NMR ($CDCl_3$) δ 8.23 (6H, s), 1.73-1.65 (12H, m), 1.41-1.32 (24H, m), 0.92 (18H, t, J=7.3Hz). ^{119}Sn {^{1}H} NMR ($CDCl_3$) δ -477.7 (s, with ^{117}Sn satellites, $^{2}J(^{119}$Sn-O-^{117}Sn) = 232 Hz (single oxo-bridge) and 50 Hz (double oxo-bridge)).

Hexameric *n*-Butyloxotin Acetate [*n*BuSn(O)O_2CCH_3]$_6$ (2). Butylstannoic acid (1.05 g, 5.02 mmol) was added to 50 mL of toluene under N_2. Acetic acid (0.30 mL, 5.2 mmol) was added and refluxed for four hours. Upon reflux, the solution became clear. Approximately 25 mL of solvent and water were removed using a Dean-Stark apparatus. The final reaction mixture was left to evaporate, forming large, square-shaped crystals. These were washed with acetonitrile and dissolved in toluene, filtered, and allowed to recrystallize through slow evaporation (yield 1.12 g, 89.0%). IR (KBr) cm^{-1}: 2957 (m), 2928 (m), 2904 (w), 2871 (w), 1599 (s), 1541 (s), 1448 (s), 611 (s). ^{1}H NMR ($CDCl_3$) δ 2.03 (18H, s), 1.63-1.57 (12H, m), 1.28 (12H, sex, J=7.3Hz), 1.22-1.17 (12H, m), 0.86 (18H, t, J=7.3Hz). ^{119}Sn {^{1}H} NMR ($CDCl_3$) δ -484.96 (s, with ^{117}Sn satellites, $^{2}J(^{119}$Sn-O-^{117}Sn) = 246 Hz (single oxo-bridge) and 67 Hz (double oxo-bridge)).

Hexameric *n*-Butyloxotin Pivalate [*n*BuSn(O)$O_2C_4H_9$]$_6$ (3). Butylstannoic acid (1.16 g, 5.57 mmol) was added to 50 mL of toluene under N_2. To this was added pivalic acid (625 mg, 6.13 mmol). The solution was refluxed for six hours, during which solvent and water were removed using a Dean-Stark apparatus and the reaction flask was refilled with toluene as necessary. The final reaction mixture was allowed to evaporate and the resulting white powder was washed with acetonitrile, dissolved in toluene, filtered, and recrystallized through slow evaporation (yield 970 mg, 59.4%). IR (KBr) cm^{-1}: 2960 (m), 2926 (m), 2872 (m), 1589 (m), 1538 (m), 1485 (m), 1423 (m), 1380 (m), 1230 (m), 602 (m). ^{1}H NMR ($CDCl_3$) δ 1.67 (12H, quin), 1.38 (12H, sex, J=7.3Hz), 1.18 (12H, t), 1.14 (54H, s), 0.89 (18H, t, J=7.3Hz). ^{119}Sn {^{1}H} NMR ($CDCl_3$) δ -486.15 (s, with ^{117}Sn satellites, $^2J(^{119}Sn\text{-}O\text{-}^{117}Sn)$ = 249 Hz (single oxo-bridge) and 73 Hz (double oxo-bridge)).

Hexameric *n*-Butyloxotin Phenylacetate [*n*BuSn(O)$O_2(CH_2)(C_6H_5)]_6$ (4). Butylstannoic acid (1.09 g, 5.20 mmol) was added to 50 mL of toluene under N_2. To this solution was added phenylacetic acid (775 mg, 5.69 mmol) and the solution was refluxed for six hours. Solvent and water were collected and removed using a Dean-Stark apparatus and the reaction flask was refilled with toluene as necessary. The final reaction mixture was centrifuged and the supernatant was allowed to evaporate, forming crystals. The crystals were washed with acetonitrile (yield 1.56 g, 91.8%). IR (KBr) cm^{-1}: 3062 (w), 3029 (w), 2956 (m), 2926 (m), 2902 (w), 2870 (w), 1600 (s), 1542 (s), 1425 (s), 1385 (s), 711 (m), 608 (s). ^{1}H NMR ($CDCl_3$) δ 7.24-7.14 (30H, m), 3.51 (12H, s), 1.44-1.37 (12H, m), 1.18 (12H, sex, J=7.3Hz), 1.13-1.08 (12H, m), 0.78 (18H, t, J=7.3Hz). ^{119}Sn {^{1}H} NMR ($CDCl_3$) δ -483.19 (s, with ^{117}Sn satellites, $^2J(^{119}Sn\text{-}O\text{-}^{117}Sn)$ = 242 Hz (single oxo-bridge) and 69 Hz (double oxo-bridge)).

Hexameric *n*-Butyloxotin Diphenylacetate [*n*BuSn(O)$O_2(CH)(C_6H_5)_2]_6$ (5). Butylstannoic acid (1.09 g, 5.20 mmol) was added to 50 mL of toluene under N_2. To this was added diphenylacetic acid (1.21 g, 5.70 mmol). The solution was refluxed for six hours during which solvent and water were removed using a Dean-Stark apparatus and the reaction flask was refilled with toluene as necessary. The final mixture was cooled to room temperature and centrifuged, and the supernatant was allowed to evaporate. The resulting white powder was washed with acetonitrile, dissolved in toluene, filtered, and recrystallized through slow evaporation (yield 1.55 g, 74.0%). IR (KBr) cm^{-1}: 3061 (w), 3028 (w), 2953 (m), 2925 (m), 2902 (w), 2869 (w), 1602 (s), 1552 (s), 1406 (s), 1384 (s), 699 (m), 618 (m). ^{1}H NMR ($CDCl_3$) δ 7.20-7.08 (60H, m), 4.82 (6H, s), 1.31-1.23 (12H, m), 1.11-1.04 (24H, m), 0.64 (18H, t, J=7.3Hz). ^{119}Sn {^{1}H} NMR ($CDCl_3$) δ -480.42 (s, with ^{117}Sn satellites, $^{2}J(^{119}Sn\text{-}O\text{-}^{117}Sn)$ = 241 Hz (single oxo-bridge) and 71 Hz (double oxo-bridge)).

Crystallographic Results and Discussion

Cluster Core

Structures of the crystallized clusters are shown in Figure 3.1 from both the side view and the top down view of the central hexagonal rings. A list of the important Sn-O bond distances in the core of the cluster and selected bond angles are shown in Table 3.1, including the O-C-O bond angles of the bidentate bridging carboxylates. The Sn-O_{hexa} bonds refer to bond lengths and angles within the hexagonal rings, Sn-O_{rect} refer to the bonds connecting the two sets of hexagonal rings, and Sn-O_{carb} refers to bonds and angles associated with the carboxylate ligands. Comparisons of all bond distances and angles in the cluster showed no significant differences, suggesting that the identity of the carboxylate ligand does not affect the geometry of the cluster core, nor the bite angle of the bridging carboxylate. This is consistent with other examples in the literature.[11]

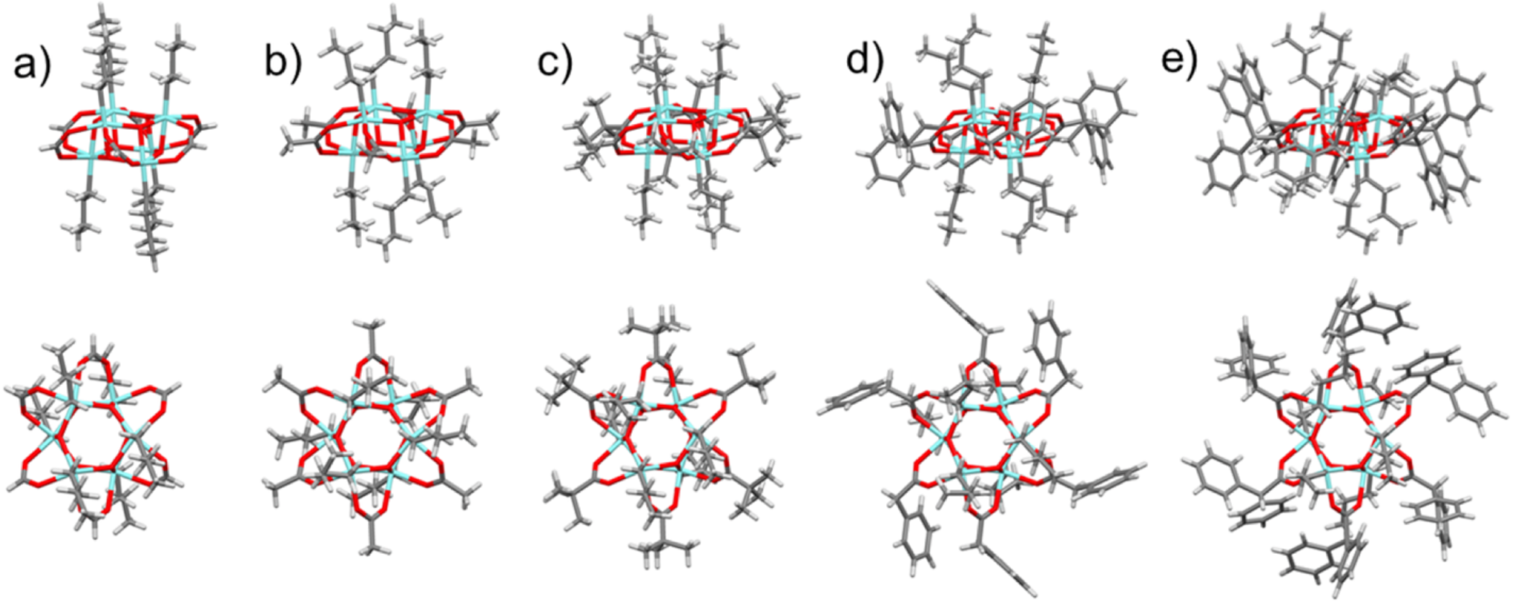

Figure 3.1. Stick representations of the X-ray crystal structures of the synthesized drum clusters from the side view (top) and a top down view (bottom): (a) **1**, (b) **2**, (c) **3**, (d) **4**, (e) **5**. Tin is shown in teal, oxygen in red, carbon in grey, and hydrogen in white. While the carboxylate ligands increase in size, the shape of the core hexagonal rings change negligibly.

Table 3.1. Structural parameters for the main bonds and angles in the core of the clusters. Repeated lengths are not shown.

	Sn-O$_{hexa}$		Sn-O$_{rect}$	Sn-O$_{carb}$		Sn-O-Sn$_{hexa}$	O-Sn-O$_{hexa}$	O-C-O$_{carb}$
Formate (**1**)	2.083(2)	2.091(2)	2.090(3)	2.177(2)	2.182(2)	133.1(1)	104.4(1)	128.1(5)
	2.082(2)	2.088(2)	2.098(3)	2.168(2)	2.169(4)	131.0(1)	103.8(1)	127.9(4)
	2.091(3)	2.092(2)	2.087(3)			131.8(1)	105.7(1)	128.2(4)
Acetate (**2**)	2.084(2)	2.086(2)	2.088(2)	2.161(2)	2.173(3)	132.2(1)	104.31(9)	126.2(3)
	2.091(2)	2.095(2)	2.089(2)	2.167(3)	2.160(3)	132.5(1)	104.73(9)	125.3(5)
			2.079(2)	2.163(3)		133.2(1)	103.99(9)	125.8(3)
Pivalate (**3**)	2.093(4)	2.095(3)	2.093(3)	2.167(4)	2.167(5)	132.0(2)	104.2(1)	125.8(6)
	2.098(4)	2.100(5)	2.095(4)	2.175(4)	2.172(3)	133.3(2)	103.9(1)	125.2(5)
	2.092(4)		2.097(4)	2.160(5)		132.4(2)	105.1(1)	125.5(5)
Phenylacetate (**4**)	2.094(2)	2.095(3)	2.088(2)	2.162(3)	2.161(2)	132.7(1)	104.73(8)	126.0(3)
	2.088(2)	2.082(3)	2.080(2)	2.123(3)	2.172(3)	133.0(1)	103.88(8)	125.9(3)
	2.095(2)	2.092(3)		2.176(3)	2.167(2)	131.6(1)	104.70(8)	125.4(3)
Diphenylacetate (**5**)	2.083(5)	2.108(3)	2.088(4)	2.160(3)	2.174(5)	132.1(2)	105.3(2)	125.7(6)
	2.093(4)	2.086(4)	2.085(4)	2.190(4)	2.158(5)	133.2(2)	103.6(1)	125.1(6)
	2.099(4)	2.089(3)	2.087(4)	2.176(3)	2.128(7)	131.3(2)	104.5(2)	125.3(6)

Table 3.2. Crystallographic data and refinement parameters.

Compound	Formate (**1**)	Acetate (**2**)	Pivalate (**3**)	Phenylacetate (**4**)	Diphenylacetate (**5**)
formula	$C_{44}H_{76}O_{18}Sn_6$	$C_{43}H_{80}O_{18}Sn_6$	$C_{54}H_{108}O_{18}Sn_6$	$C_{86}H_{112}O_{18}Sn_6$	$C_{108}H_{116}O_{18}Sn_6$
formula weight	1605.18	1597.21	1757.54	2145.88	2414.14
temperature/K	200(2)	173(2)	173(2)	200(2)	173(2)
wavelength/Å	0.71073	1.54178	0.71073	0.71073	0.71073
crystal system	Triclinic	Monoclinic	Triclinic	Triclinic	Monoclinic
space group	P-1	C2/c	P-1	P-1	$P2_1/n$
a/Å	11.5495(8)	23.4172(12)	11.7971(14)	13.3783(7)	16.4033(12)
b/Å	16.9939(11)	15.5755(8)	12.5537(14)	14.0174(7)	14.0937(10)
c/Å	17.2602(11)	16.1195(8)	14.0136(16)	14.0438(7)	22.1560(15)
α/°	111.165(3)	90	106.696(2)	71.843(2)	90
β/°	103.540(3)	93.827(2)	101.725(2)	88.139(2)	98.436(3)
γ/°	102.139(3)	90	105.543(2)	62.764(2)	90
V/Å^3	2904.4(3)	5866.2(5)	1824.8(4)	2206.04(19)	5066.7(6)
Z	2	4	1	2	2
D_{calcd}/g cm^{-3}	1.835	1.808	1.599	1.615	1.582
μ/mm^{-1}	2.603	20.524	2.079	1.736	1.522
F (000)	1568	3128	876	1072	2416
crystal size/mm	0.25 x 0.22 x 0.19	0.09 x 0.08 x 0.02	0.330 x 0.210 x 0.170	0.23 x 0.15 x 0.13	0.300 x 0.290 x 0.210
index ranges	$-15 \leq h \leq 15$	$-27 \leq h \leq 27$	$-14 \leq h \leq 14$	$-17 \leq h \leq 17$	$-18 \leq h \leq 18$
	$-22 \leq k \leq 22$	$-18 \leq k \leq 16$	$-14 \leq k \leq 14$	$-18 \leq k \leq 18$	$-15 \leq k \leq 16$
	$-22 \leq l \leq 22$	$-19 \leq l \leq 18$	$-16 \leq l \leq 16$	$-18 \leq l \leq 18$	$-25 \leq l \leq 25$
reflections corrected	66886	25137	34692	53029	37883
independent reflections [R_{int}]	14034 (0.0377)	5183 (0.0501)	6428 (0.0418)	10657 (0.0392)	7932 (0.0572)
data/restraints/parameters	14034 / 0 / 613	5183 / 0 / 305	6428 / 0 / 365	10657 / 9 / 468	7932 / 6 / 592
goodness-of-fit on F^2	1.027	1.033	1.063	1.149	1.075
R_1/wR_2 [$I > 2\sigma(I)$]	0.0264/0.0663	0.0255/0.0611	0.0335/0.0647	0.0276/0.0650	0.0423/0.1055
R_1/wR_2 [all data]	0.0414/0.0829	0.0295/0.0630	0.0526/0.00809	0.0364/0.0746	0.0557/0.1236
largest diff peak and hole/ e Å^{-3}	0.906/-0.783	1.142/-0.446	2.185/-0.98	1.458/-0.800	1.897/-1.013

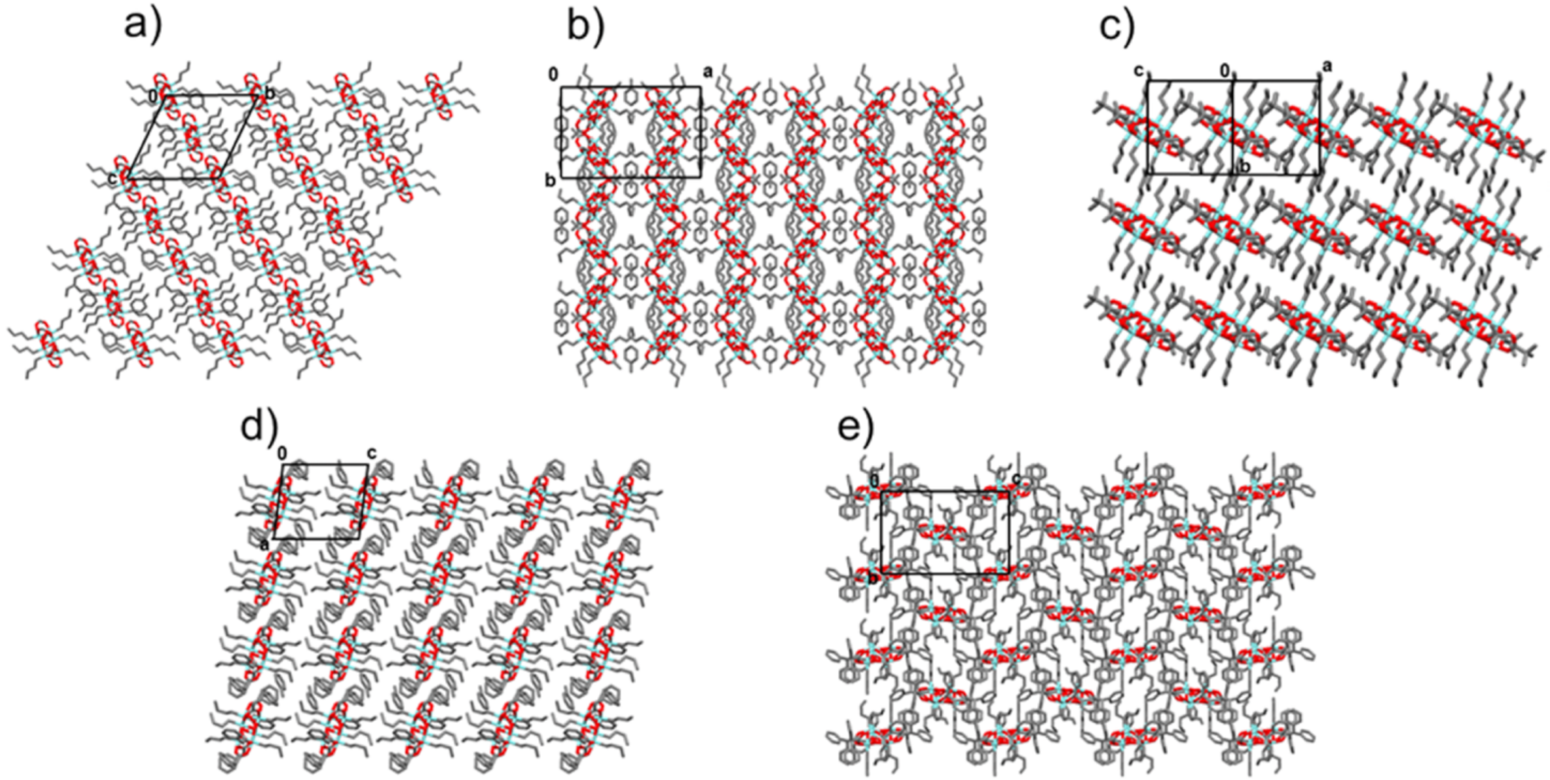

Figure 3.2. Stick representations of the packing structures showing side-on views of the clusters. Hydrogen atoms have been omitted for clarity. (a) **1**, (b) **2**, (c) **3**, (d) **4**, (e) **5**. (a), (c), and (d) are *P*-1 triclinic structures and align in sheets, while (b) adopts a *C*2/*c* structure and forms zig-zagging sheets and (e) adopts a $P2_1/n$ structure that has a body-centered arrangement.

Packing Structures

Clusters **1**, **3**, and **4** adopt triclinic *P*-1 packing structures, while clusters **2** and **5** crystallize in monoclinic space groups *C*2/*c* and $P2_1/n$, respectively. All clusters were crystallized from toluene, and one solvent molecule crystallizes per cluster in the structures of **1**, **2**, and **4**, whereas **3** and **5** do not contain solvent molecules. This is likely due to differences in the packing of the bulky *t*-butyl groups in **3** compared to the other carboxylate R groups and the additional aromatic interactions of the diphenyl groups in **5**, thus decreasing the need for solvent stabilization in these two crystal structures.

Figure 3 shows packing structures of each of the crystals from a side view of the cluster. The unit cell is shown to orient the eye. All three of the triclinic *P*-1 structures adopt sheet-like layers, where the clusters align side-by-side and are separated by areas defined by *n*-butyl ligand interactions. The two monoclinic structures adopt different geometries to accommodate the R groups of the carboxylate. The acetate groups on cluster **2** fit together interstitially, causing each cluster to alternate its orientation, shown from a top-down view in Figure 3.3 and leading to the zigzag-type layers in Figure 3.2. Cluster **5** also packs into sheets, but the spacing from the diphenylacetate groups promotes alternating layers such that the molecules in the unit cell adopt an arrangement reminiscent of a body-centered cubic structure, shown in Figure 3.3. A top down view of this array is also shown in Figure 3.3, revealing clear views down the center of the hexagonal rings.

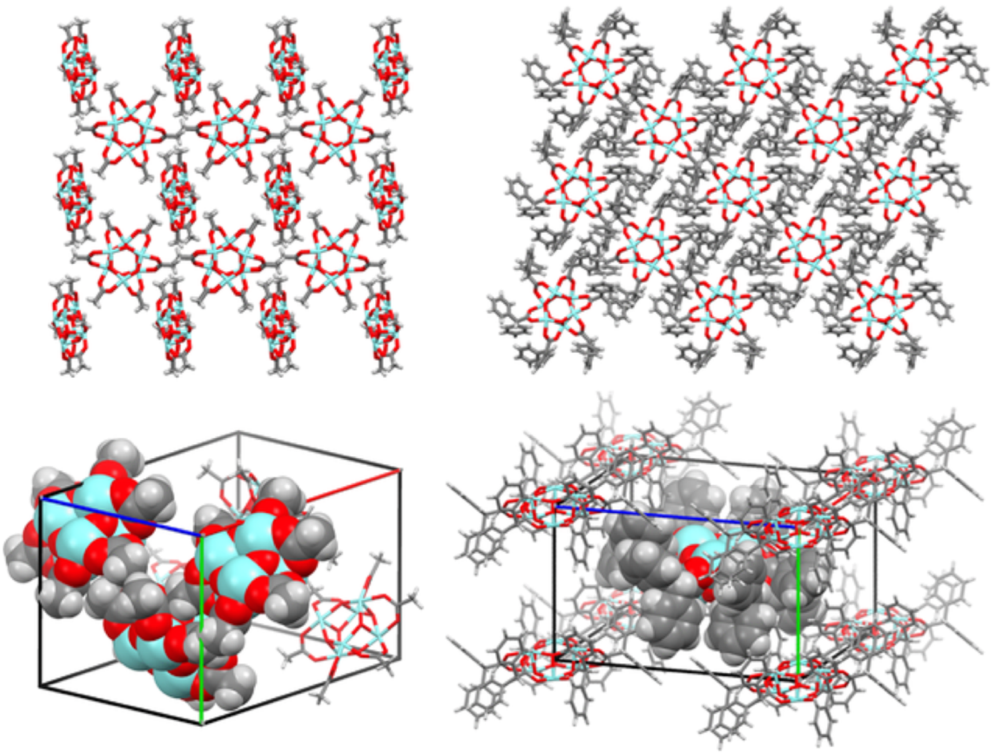

Figure 3.3. Top left: Packing structure of **2** shown down the axis of the hexagonal rings. The unit cell (bottom left) illustrates how the methyl groups on the acetate ligands fit together interstitially. Top right: Packing structure of **5** shown down the axis of the hexagonal rings. The unit cell (bottom right) shows the body-centered arrangement of the clusters. *N*-butyl groups and solvent molecules have been omitted for clarity.

The intermolecular distances between the clusters are thought to affect the efficiency of cross-linking during irradiation of the material.[21] This implies that the larger the spacing between clusters, the more energy will be needed to cross-link, thus decreasing a material's sensitivity to the irradiation source. However, it could also be hypothesized that these intermolecular distances will not affect sensitivity, but rather the film density and porosity post-irradiation will be affected based on the size of the gaps left by removal of ligands. To measure the differences in the packing structures, the closest Sn-to-Sn distances were measured across adjacent clusters. In all of the packing structures, two different distances can be observed, one across the *n*-butyl groups and the other across the carboxylate groups. Clusters **1**, **2**, **4**, and **5** generally stack with hexagonal units face-to-face across the *n*-butyl groups. Each of these has consistent Sn-to-Sn distances between 11 and 12 Å (Figure 3.4). In **3**, however, the *t*-butyl groups on the carboxylate ligands maximize van der Waals interactions with the *n*-butyl groups, so that the hexagonal faces of the drums do not perfectly align and the clusters are offset at an angle to one another. Due to these interactions, the distance between the Sn atoms from one hexagonal face to the next decreases to an average of 9.5 Å. In each cluster, the closest Sn-to-Sn distances between adjacent clusters can be observed across the carboxylate groups. The closest three distances across these groups were measured and averaged, with the results shown in Figure 3.4. The average distances increase with increasing bulk of the carboxylate group, so that **1** < **2** < **3** < **4** < **5**, trending with the relative steric bulk of each carboxylate ligand.

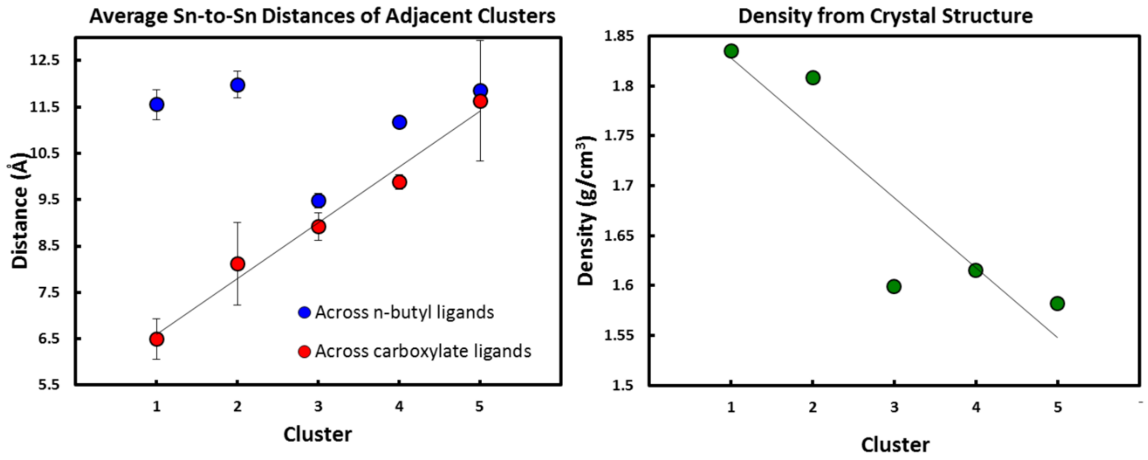

Figure 3.4. Left, average and standard deviation of the three closest Sn-to-Sn distances across different ligand groups in the packing structures. In general, the distance across the *n*-butyl groups is constant while the distance across the carboxylate groups increases with size. Right, trend showing general decrease of density as the carboxylate groups increase in size. In both graphs a line is drawn to guide the eye.

All structures were determined in a close temperature range (either 173 or 200 K), therefore the densities reported from the crystal structures could be another measure of close packing, describing the close packing of the entire structure rather than just the inorganic core. For these compounds, the density of the clusters generally trend with the Sn-to-Sn spacing, where the cluster with the closest spacing has the highest density and the cluster with the largest spacing has the lowest density.

This trend breaks with **3**, however, such that the clusters order from highest density to lowest density in the following order: **1** > **2** > **4** > **3** > **5**. This could be due to two factors. First, the additional intermolecular aromatic interactions provided by the phenyl groups of **4** can increase the density of the ligand packing through close contact as opposed to **3**, which features only weak van der Waals interactions. Second, because **3** and **5** do not crystallize with solvent molecules, the densities reported may be intrinsically lower than those that do crystallize with toluene solvates that fill volumes in the lattice that would otherwise be voids. Both of these factors could have implications on the formation of a metal oxide from irradiation of the clusters. In the first case, when considering the ease with which cleaved ligand fragments can leave a film, the varying strengths of intermolecular forces within the R groups becomes important. The weaker the intermolecular forces, the less energy will be required to desorb the fragments from the film. From this standpoint, a smaller, more volatile carbon group or a branched hydrocarbon would be preferential to a ligand that is capable of aromatic interactions. In the second case, the presence of toluene in the crystal structure suggests that certain R groups require solvent stabilization in order to crystallize. In films, this may impact the ability of the solvent to leave, requiring more energy to remove the molecule as the final oxide is formed.

While intermolecular distances, forces, solvent content, and density trends found in the crystal structures provide a means of predicting photolithographic irradiation trends, they give only a small picture of the factors that can dictate resist formation. Decomposition of the ligands also plays a significant role, as it is necessary for these groups to cleave from the core of the cluster before they can leave the material in order for a dense metal-oxide resist to form. Homolytic cleavage of the Sn-C bonds of the alkyl groups has already been shown to impact energy requirements for patterning.[19,21] For the carboxylate groups, photo-induced homolytic cleavage can be dictated by the C-C radical stability, and therefore the identity of the R group should have an impact on carboxylate decomposition.[26] For the clusters presented here, R group radical stability trends from **5** > **4** > **3** > **2** > **1**, suggesting that the cluster with the diphenylacetate groups will require less energy to cleave the carboxylate ligands while the formate cluster will require the most. This is opposite the predicted trends from density and closest intermolecular distances found from the crystal structures. Taken together, it is clear that multiple factors have the ability to influence the formation of a dense, metal-oxide from these clusters, but it is uncertain to what degree each of these will actually contribute to energy requirements needed to form the oxide and how they will impact the final quality of that oxide. We are currently investigating how cluster structure dictates resist formation by examining sensitivity trends and analyzing the final oxide films after exposure to both UV and electron beam sources.

Conclusion

We have prepared and determined the X-ray crystal structures of a series of five organotin carboxylates of the general formula $[n\text{BuSn(O)O}_2\text{CR}]_6$. We analyzed these structures in the context of the use of tin clusters as EUV photoresists. By changing the carboxylate group, the cores of the structures remain unchanged; however, the steric bulk and intermolecular forces of the different carboxylate ligands had significant effects on the packing structure of the clusters. The nature of the carboxylate influenced the incorporation of solvent molecules in the crystals as well. The crystal structures of these clusters provide insight into how close packing and density change as a function of ligand size and identity. These trends in packing and density are likely to influence the efficiency of cross-linking of the inorganic metal centers along with factors such as ligand decomposition and ligand desorption and should be considered when designing photoresists capable of high resolution and high sensitivity. This work provides a clear set of hypotheses with which to experimentally study thin-film resist formation, and we intend in future work to describe how these factors relate to radiation doses necessary for film formation and how structural differences impact the properties of the final films.

Bridge to Chapter IV

Modifying the ligand structure of the organotin drum clusters has an impact on their cluster-to-cluster interactions, such as close packing and density. While this information can be gleaned from studying the crystal structures, experimental data is necessary to determine what impact these factors actually have on the patterning reaction. Chapter IV describes an experimental study of three different organotin carboxylate species that vary in core structure in order to elucidate the effects of structure on reactivity in the context of direct-write electron beam patterning. The chemical reaction that occurs between the organotin reagents and the electron beam, the patterned film products, and the ligand decomposition and desorption byproducts were compared across all species. We found that both the metal-oxo content and the ligand coordination mode of each organotin reagent affected the reaction efficiency during electron beam patterning. In each case, an insoluble metal-oxo product formed after irradiation, but the composition, structure, and surface morphology of the products were nearly indistinguishable from the initial films. Examining the byproducts of the irradiation chemistry using electron stimulated desorption confirmed that many of the organic ligands remained in the film during the reaction, likely cross-linking the clusters together to form a metal-oxo polymer product. Finally, we discuss the implications of the chemical transformations that occur during patterning for the use of these organotin reagents as both photoresists for lithography and direct-write functional nanomaterials.

CHAPTER IV

ORGANOTIN CARBOXYLATE REAGENTS FOR NANOPATTERNING: CHEMICAL TRANSFORMATIONS DURING DIRECT-WRITE ELECTRON BEAM PROCESSES

This chapter is expected to appear as Sharps, M. C.; Frederick, R. T.; Javitz, M. L.; Herman, G. S.; Johnson, D. W.; Hutchison, J. E. Organotin Carboxylate Reagents for Nanopatterning: Chemical Transformations During Direct-Write Electron Beam Processes. *Chem. Mater.* **2019**, *accepted.* Copyright 2019, American Chemical Society.

Introduction

The use of inorganic materials for patterning chemistry has been prompted by the semiconductor industry's ever-increasing demand for high density integrated circuits.[1] Improved processing capacity stems from the ability to continually decrease feature size and, thus, circuit component size. Electron beam lithography (EBL) and extreme ultraviolet lithography (EUVL) have become promising approaches to writing sub-20 nanometer features.[2,3] However, one also needs new resists that can capture these electrons or photons and produce nanoscale patterns. Development of new resists has focused on inorganic materials, often composed of metal oxide nanoparticles[4–7] or clusters[8–14] containing metals like Sn, Hf, Zr, and Ti. These materials have been used to maximize the absorption of EUV photons, reduce pattern blurring, and increase etch resistance.[15–17] Each of these attributes stems from the inorganic nature of these reagents and allows for higher resolution patterning. The use of stabilizing ligands allows these reagents to be processed in solution, thus enabling traditional manufacturing procedures.[1] Although the practical utility of these materials has been established in the context of nanolithography (optimizing line edge roughness, critical dimension, contrast, and sensitivity), little is known about the chemistry of the patterning process or the composition of the post-irradiated material. The influence of precursor structure on the patterned product has not been explored. Depending on the properties of these post-processed metal oxide materials, nanoscale products from these novel resists have the potential to find applications as functional materials in addition to their use as agents for pattern transfer.[18]

For inorganic resists, the mechanisms that govern contrast change and pattern formation are dictated in part by the ligands that are used to stabilize the metal, cluster, or nanoparticle in solution and how these ligands decompose or react under incident irradiation. Although there are a wide variety of chemistries that can occur for each of these types of materials, the products formed during the patterning reaction are often presumed to be dense metal oxides.[11] For example, in metal oxide sulfate (MSO_x) cluster materials with hydrogen peroxide, radiation induced peroxide desorption and subsequent condensation leads to M-O-M crosslinking, prompting a solubility change.[8,19,20] Metal oxide nanoparticle resists have been developed to be stabilized by photosensitive ligands or photoacid generators that decompose under UV irradiation, causing changes in solubility that lead to particle agglomeration.[1,4,18,21] In other cases, nanoparticles stabilized by long-chain organic ligands undergo cross-linking when exposed to electrons or X-rays.[22] For organometallic clusters, it is hypothesized that irradiation drives decomposition of organic groups, followed by cross-linking of metal and oxygen bonds to create an insoluble network.[9,10,23,24] We have previously demonstrated the loss of butyl ligands in resists deposited from two model organotin species.[25–27] The irradiation products that form from each of these inorganic resists, or reagents, have the potential to be used for a variety of direct-write applications. Determining how the structure of the inorganic reagent impacts the chemical transformation will help guide design principles when considering new materials for direct-write applications.

Tin carboxylate complexes have previously been used as model compounds for EUV inorganic resists.[9,10,23] It is thought that these materials undergo loss or decomposition of organic ligands under incident radiation,[25,26,28] leading to cross-linking that produces an insoluble metal oxide network used as a negative tone resist (Scheme 4.1). Previous work has demonstrated that the identity of the ligands and strength of the Sn-ligand bonds impact patterning performance.[9,10] However, little is known about the chemistry involved in the patterning process. Tin carboxylates can be synthesized in a variety of discrete monomeric and <1nm clusters species that can influence this chemistry.[29–34] A systematic study to assess the role of ligand and species core structure on this chemistry would be beneficial in order to understand how structure impacts both patterning performance and the formation of the patterned product. We hypothesize that the extent of preformed metal-oxo bonds within the precursor structure will have an effect on both the efficiency of cross-linking during patterning and on the final film structure that forms.

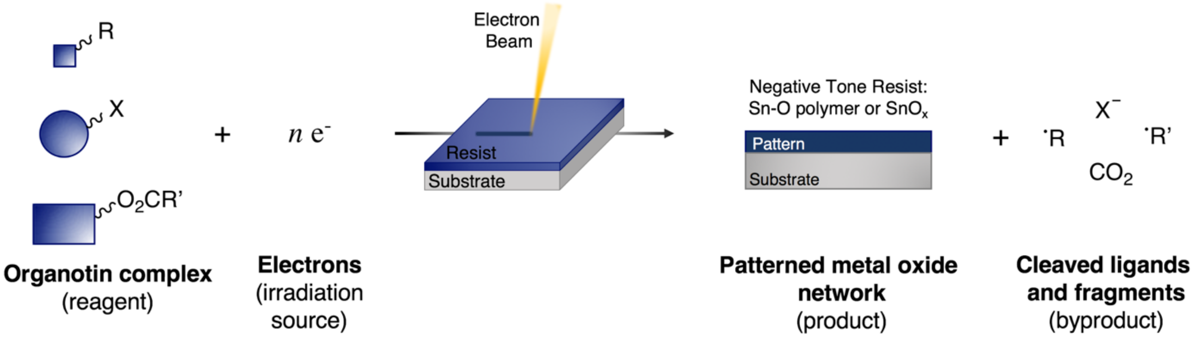

Scheme 4.1. Schematic of the reaction occurring during electron beam patterning of an organotin complex. A given dose of electrons reacts with an organotin complex, causing organic fragments to desorb from the film. The remaining inorganic fragments left behind crosslink to form an insoluble product, consisting of either a tin-oxo polymer or tin oxide. The different shapes of the organotin complexes are meant to represent different core structures and sizes that these species can exhibit.

Here we compare the reactivity of three organotin carboxylate species—two clusters and a monometallic species with varying degrees of preformed metal-oxo bonds—during exposure to electron irradiation. Each species is stabilized by the same ligands in order to elucidate how inorganic structure, rather than ligand identity, contributes to changes in the chemistry resulting from irradiation. We have chosen to use electron irradiation rather than EUV sources because it is possible to expose films to the same energy electrons across multiple analytical techniques: scanning electron microscopy (SEM) and electron stimulated desorption (ESD). We investigate these transformations through analysis at three stages of the reaction: the reaction between the tin carboxylate reagent and the electron beam, the formation of the film product, and the byproducts of the reaction. By either changing the type of tin carboxylate or the flux of electrons (as illustrated by Sch. 4.1) it should be possible to determine how each influences the chemical transformations that occur during direct-write processes. Our results suggest that species structure has a significant impact on the efficiency of the chemical transformation upon electron irradiation. However, the structure does not have a strong influence on the formation of the metal oxide product. In each case, electron irradiation induces cross-linking across the tin carboxylate structures to form a product more similar to a metal-oxo polymer. Thermal annealing is required to produce dense metal oxide films.

Experimental Section

Materials and Methods

All reagents and chemicals were obtained from commercial sources and used without further purification. The football shaped dodecameric cluster, **1**, was synthesized according to Eychenne-Baron et al.[35] while the synthesis of the hexameric drum cluster, **2**, was modified from Holmes et al.[30] and previously reported by our group.[36] The monometallic species dibutyltin diacetate, **3**, was purchased from Sigma Aldrich, checked by NMR and IR spectroscopy to confirm purity (>99%), and used as purchased. ^1H, $^{119}Sn\ \{^1H\}$, and ^1H DOSY NMR spectra were obtained on a Bruker Avance III-HD 600 spectrometer (600.02 MHz for ^1H and 223.61 MHz for $^{119}Sn\ \{^1H\}$) in $CDCl_3$ at 25 °C). Proton resonances are referenced to tetramethylsilane, while tin resonances are referenced to tetramethyltin (external standard). Infrared spectra were recorded using KBr pellets on a Thermo Scientific Nicolet 6700 FT-IR spectrometer. Bulk powders of the two clusters were analyzed using Thermogravimetric Analysis (TGA) on a TA Instruments Thermogravimetric Analyzer, TGA Q500, by ramping from room temperature to 600 °C at a rate of 10 °C per minute under N_2.

Dodecameric n-Butyloxotin Acetate $[(nBuSn)_{12}O_{14}(OH)_6]^{2+}(CH_3COO^-)_2$ **(1)**.

Synthesis of 1a: Butylstannoic acid (6.13 g, 29.3 mmol) was added to 150 mL of toluene under N_2 in a 250 mL 2-necked round bottom flask attached with a Dean-Stark trap and a condenser. *p*-Toluene sulfonic acid monohydrate (1.86 g, 9.78 mmol) was added and refluxed for 48 h. The resulting product solution was centrifuged to remove unreacted starting materials and the supernatant was evaporated to dryness, resulting in a white powder identified as $[(n\text{BuSn})_{12}\text{O}_{14}(\text{OH})_6]^{2+}(\text{OTs}^-)_2$ (**1a**), as verified by ^{1}H and ^{119}Sn NMR spectra consistent with previous reports of this compound.[35]

Synthesis of 1b: A 20% w/w solution of **1a** (2.00 g, 0.719 mmol) in isopropyl alcohol (IPA) (8.00 g, 10.2 mL) was prepared. A second solution containing 65% w/w of 1M tetramethylammonium hydroxide (TMAH) (1.69 g, 18.5 mmol) in IPA (0.71g, 0.90 mL) was prepared and quickly added to the solution containing **1a**. This mixture was stirred at room temperature until fully dissolved. This solution was placed in the freezer and formed a white precipitate after 48 h. This precipitate was washed with acetonitrile and verified by ^{1}H and ^{119}Sn NMR as $[(n\text{BuSn})_{12}\text{O}_{14}(\text{OH})_6]^{2+}(\text{OH}^-)_2$ (**1b**), consistent with previous reports in the literature.[35]

Synthesis of 1: Counteranion exchange of the hydroxide to acetate groups was conducted by taking **1b** (84.3 mg, 0.031 mmol) in 1 mL of tetrahydrofuran (THF) and adding 2 equiv of acetic acid (3.7 mg, 0.062 mmol) in 1 mL of THF. The mixture was stirred at room temperature for 30 min and dried at room temperature on a watch glass. The final product was characterized as $[(n\text{BuSn})_{12}\text{O}_{14}(\text{OH})_6]^{2+}(\text{CH}_3\text{COO}^-)_2$ (**2**) (yield: 83.9 mg, 97%). IR (KBr) cm^{-1}: 2955 (m), 2923 (m), 2870 (w), 1533 (w), 1464 (w), 1384 (s), 617 (m), 538 (m). ^{1}H NMR (CDCl_3) δ 1.89 (6H, s), 1.73 (12H, quin, J=7.5Hz), 1.65-1.50 (24H, m), 1.50-1.42 (12H, m), 1.32 (12H, sex, J=7.4Hz), 1.14 (12H, m), 0.92 (18H, t, J=7.3Hz), 0.86 (18H, t, J=7.3Hz). ^{119}Sn {^{1}H} NMR (CDCl_3) δ -458.85 (s), -282.21 (s).

Hexameric n-Butyloxotin Acetate [$nBuSn(O)O_2CCH_3]_6$ **(2)**.

Butylstannoic acid (1.049 g, 5.023 mmol) was added to 50 mL of toluene under N_2. Acetic acid (0.30 mL, 5.2 mmol) was added and refluxed for 4 h. Upon reflux, the solution became clear. Approximately 25 mL of solvent and water were removed using a Dean-Stark apparatus. The final reaction mixture was left to evaporate, forming large, square-shaped crystals. These were washed with acetonitrile and dissolved in toluene, filtered, and allowed to recrystallize through slow evaporation (yield 1.12 g, 89.0%). IR (KBr) cm^{-1}: 2957 (m), 2928 (m), 2904 (w), 2871 (w), 1599 (s), 1541 (s), 1448 (s), 611 (s). ^1H NMR ($CDCl_3$) δ 2.03 (18H, s), 1.63-1.57 (12H, m), 1.28 (12H, sex, J=7.3Hz), 1.22-1.17 (12H, m), 0.86 (18H, t, J=7.3Hz). $^{119}Sn\ \{^1H\}$ NMR ($CDCl_3$) δ -484.96 (s, with ^{117}Sn satellites, $^2J(^{119}Sn\text{-}O\text{-}^{117}Sn)$ = 246 Hz (single oxo-bridge) and 67 Hz (double oxo-bridge)).

Spin Coating Procedures

One hundred nanometer thermal oxide on p-type (1-100 Ω-cm) {100} silicon was cut into 2 cm x 2 cm squares and cleaned with a mixture of 5 parts 18.2 MΩ water, 1 part NH_4OH, and 1 part 30% H_2O_2 at 80°C for 20 min. The cleaned wafers were rinsed with nanopure water before being plasma cleaned in O_2 plasma for 5 min. For the monometallic species dibutyltin diacetate, **3**, a 13 mg/mL solution in toluene was spin coated onto the plasma cleaned wafers at 3000 rpm for 30 s, giving approximately 20 nm films as measured by ellipsometry. For the acetate hexameric (**2**) and acetate dodecameric (**1**) clusters, the plasma cleaned wafers were vapor treated with HMDS at 120°C for 30 min under standard conditions. An 11 mg/mL solution of **2** in toluene yielded approximately 20 nm films at a spin coating rate of 3000 rpm for 30 s. A 10 mg/mL solution of **1** in toluene yielded approximately 20 nm films at a spin coating rate of 3000 rpm for 30 s. All films were soft baked on a hotplate at 70°C for 1 min to remove residual solvent.

Electron Patterning

a) Exposure for dose arrays: Films of each **1**, **2**, and **3** prepared as described above were patterned in a ZEISS Ultra-55 Scanning Electron Microscope (SEM) utilizing the Nanometer Pattern Generation System (NPGS). Seven-by-seven arrays of 200 x 200 μm^2 boxes with centers spaced 400 μm apart were patterned with accelerating voltages of 2 kV at a half pitch of 30 nm. Each box increased in incremental doses. The minimum dose was 2 $\mu C/cm^2$, increased by increments of 1 $\mu C/cm^2$, and the maximum dose was 50 $\mu C/cm^2$.

b) Exposure for area doses: Larger, 1 x 1 mm^2 squares were patterned on films of **1**, **2**, and **3** prepared as described using a ZEISS Ultra-55 SEM equipped with NPGS. These large areas were patterned specifically for X-ray photoelectron spectroscopy (XPS) and the areas were chosen in order to encompass the X-ray spot size. These larger areas were patterned at low (50 $\mu C/cm^2$) and high (450 $\mu C/cm^2$) doses. A 2kV accelerating voltage was used for both doses and each sample was patterned in triplicate.

c) Development procedure: After patterning the samples were developed in toluene to remove unreacted starting material by sonicating for 1 min or by active spin coating of toluene on the surface of the wafers for 30 s at 3000 rpm. Both methods produced similar development performance.

Electron stimulated desorption procedure

Films of **1**, **2**, and **3** were also prepared on bare n-type (0.0010-0.0055 Ω-cm) {100} silicon. These 1 x 1 cm^2 samples were cleaved from the center of spun 4 x 4 cm^2 samples to remove edge effects. The material was analyzed using electron stimulated desorption (ESD) performed in a Hiden analytical temperature programmed desorption (TPD) workstation (base pressure 1×10^{-9} Torr) which uses a Hiden quadrupole mass spectrometer (QMS) with digital pulse ion counting. The workstation has a Kimball Physics low energy electron gun (ELG-2 gun with EGPS-1022 power supply), where exposure times are controlled with a mechanical shutter. A stage-level Faraday cup (Kimball physics FC-70C) was used to characterize the areal current density profile of the Gaussian electron beam, $E_{kin} = 2$ keV, immediately before each ESD experiment. The average current density in the full width half maximum (FWHM) of the beam was [~0.15 $\mu A/cm^2$]. For ESD experiments the sample was positioned at the focal point of the electron gun, 17 mm below the TPD system's spring loaded pins near the mass spectrometer inlet. The Faraday cup was mounted on a rotatable 3-axis translator. For in-depth comparisons of the desorption kinetics, we monitored mass fragments associated with the parent groups of the butyl and acetate groups, m/z 56 (C_4H_8) and 60 (CH_3CO_2H), respectively. These were chosen in order to separate trends due to each ligand; smaller masses can be associated with either butyl or acetate fragments.

Thermal annealing procedure

Thicker films (60-70 nm) of **1** and **2** were placed in a tube furnace open to air to drive the films toward an oxide as a comparison to the irradiated films. Films were heated from room temperature to 600 °C at a rate of 10 °C per min to match the heating rates of

TGA analysis. The films were allowed to cool to room temperature under atmosphere before being removed from the furnace.

Film Characterization of As-Spun and Treated Organotin Thin Films

Elemental composition was performed using a Thermo Scientific ESCALAB 250 X-XPS with an Al Kα monochromated source at 20 kV. All samples were charge neutralized with an in-lens electron source. Survey spectra of each sample spot were taken along with high-resolution C 1s, O 1s, Sn 3d, Si 2p, and valence band (VB) spectra. The order each high-resolution spectrum was obtained was rotated across the triplicate data sets to confirm that the X-ray beam was not inducing chemistry in the sample. These spectra were calibrated to the C 1s binding energy (284.8 eV). Spectra were peak fit using ThermoScientific Avantage 4.88 software to calculate atomic percentages, which were used for elemental ratio comparisons. Valence Band (VB) XPS spectra were also taken for each film and were referenced to the C 1s binding energy.

X-ray diffraction (XRD) measurements were collected to determine the crystallinity of the thermally treated films. A grazing incidence (GIXRD) geometry was used on a Rigaku SmartLab with a Cu source. The incident angle was 0.5° relative to the sample plane and measurements were taken over a 2θ range of 20° to 80° relative to the sample plane in 0.1° steps. A Ni filter was used to remove Cu Kβ interference and resulting spectra were referenced to bulk SnO and SnO_2.

Surface morphologies for all films and step heights for the dose array patterns were determined using a Bruker Dimension Icon Atomic Force Microscope (AFM) equipped with Fastscan (Figure C5). Thickness was measured with AFM rather than ellipsometry because it was difficult to find an ellipsometric model that would reasonably describe the film. The thicknesses modelled by ellipsometry were inconsistent from pattern to pattern. Additionally, the patterned films were thin (<15 nm), so we felt that AFM would provide the most accurate data as opposed to stylus or optical profilometry. Al coated Si tapping mode probes were used, and images were collected over 1 μm square areas. To determine surface root-means-squared (RMS) roughness, three 1 μm images were taken at different areas across each film and the values averaged. All images had first order flatten fits applied, while third order plane fits were applied to analyze step height measurements.

Finally, selected area electron diffraction (SAED) and high-resolution transmission electron microscope (HRTEM) experiments were performed on a Titan 80-300 TEM at a 300 kV accelerating voltage using patterned films that were prepared directly on lacey carbon coated Cu TEM grids (Ted Pella).

Results and Discussion

Resist Reagents and Reaction Efficiency

The three organotin carboxylate species used as reagents in the patterning reaction are shown in Figure 4.1. These species were chosen because they all contain Sn-O bonds, have the same stabilizing ligands (butyl and acetate groups), and have Sn atoms that begin in the 4+ oxidation state. However, each species possesses a different inorganic core structure and ligand binding modes.

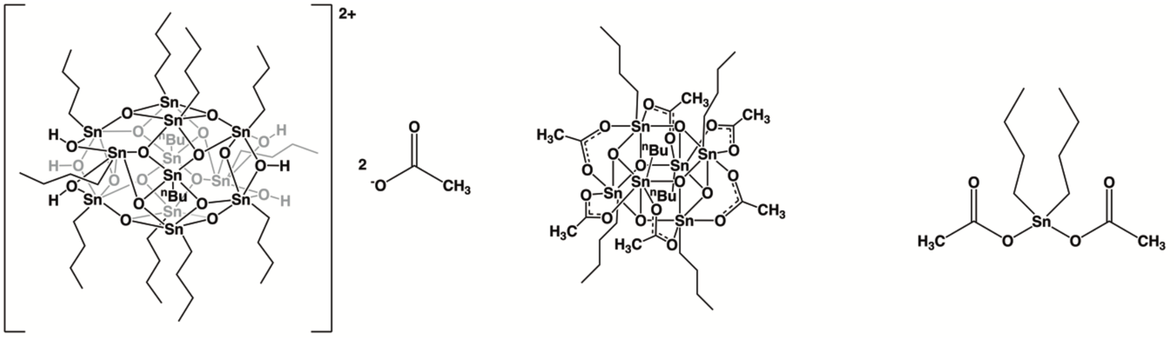

$[(n\text{-BuSn})_{12}O_{14}(OH)_6]^{2+}(O_2CCH_3^{-})_2$
Football Cluster
1

$[n\text{-BuSn}(O)O_2CCH_3]_6$
Drum Cluster
2

$n\text{-Bu}_2Sn(O_2CCH_3)_2$
Monometallic Compound
3

Figure 4.1. The three Sn reagents used in this study. A dodecameric structure stabilized by butyl ligands and acetate counteranions (**1**). A hexameric structure stabilized by butyl ligands and bidentate acetate groups (**2**). A monometallic species stabilized by butyl ligands and monodentate acetate groups (**3**).

The football shaped dodecameric tin cluster, **1**, contains the largest core network of preformed Sn-O-Sn bonds. The Sn atoms along the center of the cluster are each 5-coordinate, while the Sn atoms at the edges of the cluster are 6-coordinate. The drum shaped hexameric structure, **2**, is half the size of the first cluster, and features only 6-coordinate Sn atoms. Dibutyltin diacetate was chosen as the monometallic species, **3**. It does not contain any preformed Sn-O-Sn moieties and only has one 4-coordinate Sn atom. The coordination around each Sn atom is reflected in the ^{119}Sn NMR shifts, shown in Figures C1 – C3. Each species is stabilized by butyl ligands that are covalently bonded to Sn atoms and by acetate ligands. The acetate groups, however, coordinate differently across all three species. In reagent **1**, the carboxylates are outer sphere counteranions stabilizing the positive charge of the central cluster. Reagent **2** has acetates that bind in a bidentate fashion to the cluster core, while reagent **3** features monodentate acetate coordination. We expect that the difference in ligand coordination mode will affect the reaction due to differences in interaction energies, but we also expect differences in reactivity to correlate with the extent of the metal-oxo framework in the cluster core.

We evaluated the reactivity of each tin reagent with varying doses of electrons to determine each species' sensitivity. Sensitivity provides a measure of how efficiently a material can undergo a reaction with incident irradiation.[37] Comparing the relative sensitivities between tin reagents can give an indication of what factors dominate the ability of the radiation induced chemistry to occur. This comparison helps us determine which factor (the ligand coordination mode or the presence of Sn-O-Sn linkages) makes the largest difference on the efficiency of the reaction. To determine sensitivity, we created dose arrays of 200 μm x 200 μm box patterns for each film at 2 kV. After developing the films in toluene, the resulting thickness of each patterned box was measured using AFM (Figure C4) and plotted against the electron dose to create dose curves (Figure 4.2). For each Sn compound, a trend line is drawn between normalized thicknesses of 0.2 and 0.8. These lines can be extrapolated to calculate two important values, d_0 and d_{100}. The value where the extrapolated line crosses the x-axis designates the highest dose where all of the material can still be rinsed away during development, d_0. The value where the extrapolated line crosses a y value of 1, d_{100}, is the lowest dose where the film is completely insoluble during development. The value of d_{100} corresponds to the resist's sensitivity, with lower values designating higher sensitivities. Cluster **1** has the highest sensitivity at a dose of 12 $\mu C/cm^2$, while cluster **2** and compound **3** have lower, but similar sensitivities at doses of 37 and 39 $\mu C/cm^2$, respectively. To understand the factors dominating the contrast chemistry that occurs, we must first consider the factors that influence each step in the resist reaction.

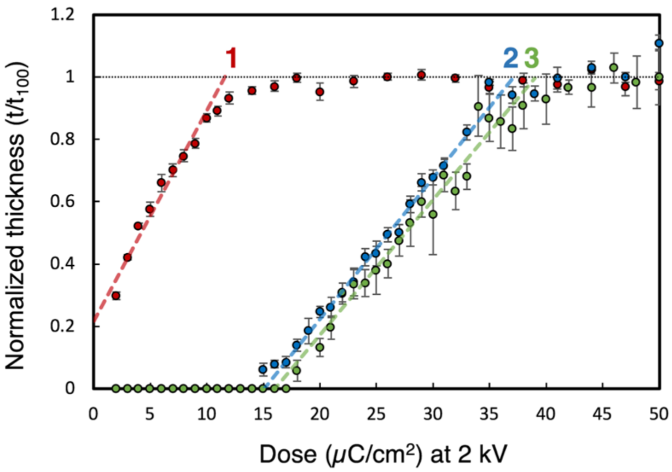

Figure 4.2. Dose curves plotted for each species at a 2 keV accelerating voltage. Cluster **1** is the most sensitive, while cluster **2** and compound **3** are within error of each other and are both less sensitive than **1**. Trend lines fit between normalized thicknesses of 0.2 and 0.8 are extended to meet a y-value of 1, designated by a black dotted line. The dose where the two trendlines hit the y=1 line is d_{100}, the sensitivity of the material. Species **1** is so sensitive to the electron beam that there is a significant pattern at 2 μC/cm^2, the lowest possible dose we could achieve with the SEM at 2 kV.

The first step in the reaction that results in an insoluble material during patterning is decomposition and loss of the stabilizing ligands.[23,25,28] It has been shown that the stronger the Sn-C bond strength of the alkyl group, the more energy it takes to cleave and remove that ligand, and the lower the sensitivity of the material.[9,10] We also expect that the coordination mode of the acetate ligands in our system will affect their rate of decomposition because of energy differences required for bond cleavage, which should correlate to sensitivity. This energy difference is reflected in thermal decomposition data, where the more-weakly bonded acetate groups of **1** decompose at a lower temperature than the bidentate acetates in **2** (TGA, Figure C5). Based on ligand bond strength, it is expected that **1** would require the least amount of energy for loss of the acetate group because it is weakly associated with the cluster as a non-coordinating counteranion. Cluster **2** would require the most energy because it contains the strongest bonds as a bidentate ligand, necessitating the cleavage of two bonds to release the acetate from the core of the cluster. Finally, compound **3**, with monodentate coordination, is stronger than the counteranion but weaker than the bidentate group. By the interaction energies of the ligands alone, we would predict a sensitivity trend of **1** > **3** > **2**.

The second step in the patterning reaction occurs as the inorganic core left behind condenses and cross-links to form a more dense metal-oxo product.[11] The two cluster precursors, **1** and **2**, contain networks of preformed Sn-O-Sn bonds, whereas **3** does not. These metal-oxo networks can theoretically reduce the number of reactions required to crosslink a given area of resist by acting like building blocks. We hypothesize that the larger the preformed core, the less restructuring necessary in order to form the metal oxide product. Considering core structure alone would predict a sensitivity trend of **1** > **2** > **3**.

The experimental sensitivity data shows that **1** is the most sensitive. Cluster **1** has the largest number of preformed Sn-O-Sn bonds and the most weakly coordinated acetate ligands. However, the similar sensitivities of **2** and **3** show that there is a balance between dominating factors: the greater preformed metal-oxo framework in **2** does not outweigh the more weakly bonded acetate groups of **3**, and vice versa. Rather, the lack of a trend in relative sensitivity indicates that both factors, ligand coordination mode and Sn-O-Sn structure, influence the radiation induced chemistry. The structure of the precursor can be tuned in both the ligand shell and the metal-oxo framework in order to enhance reactivity with electrons.

Composition and Structure of the Patterned Product

After determining that both ligand coordination mode and inorganic core structure affect species reactivity, we used XPS to investigate whether these changes in reactivity also influence the composition of the metal oxide structure in the final patterned film products. For comparison, XPS was performed on untreated samples of each material, on samples patterned at both 50 μC/cm^2 and 450 μC/cm^2, and on films of **1** and **2** that were thermally driven to oxides. Separately, we observed that no Sn is removed from the sample through electron irradiation during electron stimulated desorption experiments (ESD, Figure C10). Because the amount of Sn remains constant before and after patterning, we compared ratios of the atomic percentages given by XPS of C_{aliph} (aliphatic C peak at 284.8 eV) to Sn and C=O to Sn to track removal of the butyl and acetate groups, respectively (Table 4.1). At doses of 50 μC/cm^2, where all films are fully insoluble, all species underwent a loss of C_{aliph} signal. Across every species, however, 50% or more of the carbon attributed to butyl ligands was still found in the films. We irradiated films at higher doses (450 μC/cm^2) to see if continued exposure would result in more ligand loss. While the films do continue to lose ligands, the rate of loss is lower (Figure C6). Additionally, for the two clusters, much of the carbon attributed to ligands is still present in the patterned films compared to those that were thermally driven to an oxide: about three times the expected amount of carbon was present for **2** and five times more for **1**. In all films, regardless of core structure and ligand coordination mode, the composition by XPS indicates that a significant amount of organic ligand remains after irradiation.

Table 4.1. Ratios of XPS atomic percentages comparing C=O/Sn and C_{aliph}/Sn for all three species.[a]

	Football Cluster **1**		Drum Cluster **2**		Monometallic Compound **3**	
	C=O/Sn	C_{aliph}/*Sn*	*C=O/Sn*	C_{aliph}/*Sn*	*C=O/Sn*	C_{aliph}/*Sn*
Expected	0.17	4	1	4	2	8
As Spun	0.020 ± 0.015	4.51 ± 0.16	0.798 ± 0.015	5.39 ± 0.12	0.433 ± 0.015	9.01 ± 0.31
50 μC/cm^2	0.047 ± 0.004	3.29 ± 0.28	0.140 ± 0.007	3.27 ± 0.18	0.102 ± 0.001	4.49 ± 0.71
450 μC/cm^2	0.065 ± 0.005	1.89 ± 0.08	0.151 ± 0.003	1.58 ± 0.02	0.161 ± 0.013	2.56 ± 0.08

[a] As spun, the experimental atomic percentages of Sn, O, and C are similar to the atomic percentages expected from the molecules alone. The values for as spun C_{aliph}/Sn are slightly greater than expected, which is expected due to adventitious carbon from air exposure. The values for as spun C=O/Sn are lower than expected in all cases, likely due to a brief initial reaction with x-rays or photoelectrons from irradiation by the Al Kα XPS source (1486.6 eV). C=O is reduced relative to the expected value by 8.3x for the football, 5x for the monomer, and 1.25x for the drum, in a manner consistent with the interaction strength of the acetate groups for these species. After patterning at both 50 μC/cm^2 and 450 μC/cm^2, the ratios of C to Sn remain higher than expected, suggesting that components of the organic ligands remain in the film after exposure.

We performed control measurements to estimate whether carbon deposited during SEM patterning of the films contributed significantly to the elevated C_{aliph}/Sn and C=O/Sn ratios in the patterned films (Figure C7). We compared SiO_2 wafers that were clean with those exposed to the same electron dose as the organotin films. After electron exposure, the C_{aliph} signal increased by less than 5%. In comparison to the high percentages of carbon found in the organotin films after patterning, this suggests that carbon deposition does not significantly inflate these measurements and that the high C_{aliph} values are indicative of ligand remaining in the patterned films. The amount of deposited C=O was also measured and increases by about 1%, which is on the same order of magnitude as the percentages of C=O found in the films and has the potential to affect these values. These controls can explain the slight increases of C=O relative to Sn found in patterned films of **1** and in **2** and **3** at 450 $\mu C/cm^2$.

It is believed that these inorganic resists form metal oxides upon patterning.[11] However, the high content of organic matter left in the film after patterning suggested that a dense metal oxide was not forming as a result of electron irradiation. We analyzed the patterned films using AFM to look at physical changes in surface morphology and Valence Band (VB) XPS to investigate changes in electronic structure in an effort to understand what product actually forms between these tin reagents and incident electrons. For these experiments, films irradiated at both 50 and 450 $\mu C/cm^2$ were compared to untreated films and with thermally treated films.

By AFM, the electron irradiated films retain many similarities to the freshly spin-coated, untreated films. Prior to reaction with electrons, the precursors are approximately a nanometer or less in radius, which is reflected in the RMS roughness of ~1 nm in the untreated films (Figure 4.3). As the electron dose is increased, the RMS roughness of the patterned films decreases. Additionally, surface features found in the untreated precursor films are maintained in the patterned ones. These features are most clearly seen in films of **1**, where long, slightly curved and elevated "hills" are preserved as the electron dose increases. Both the smoothness of the electron patterned films and the preservation of the surface features like these "hills" indicate that changes in the physical film structure are occurring on a local scale.

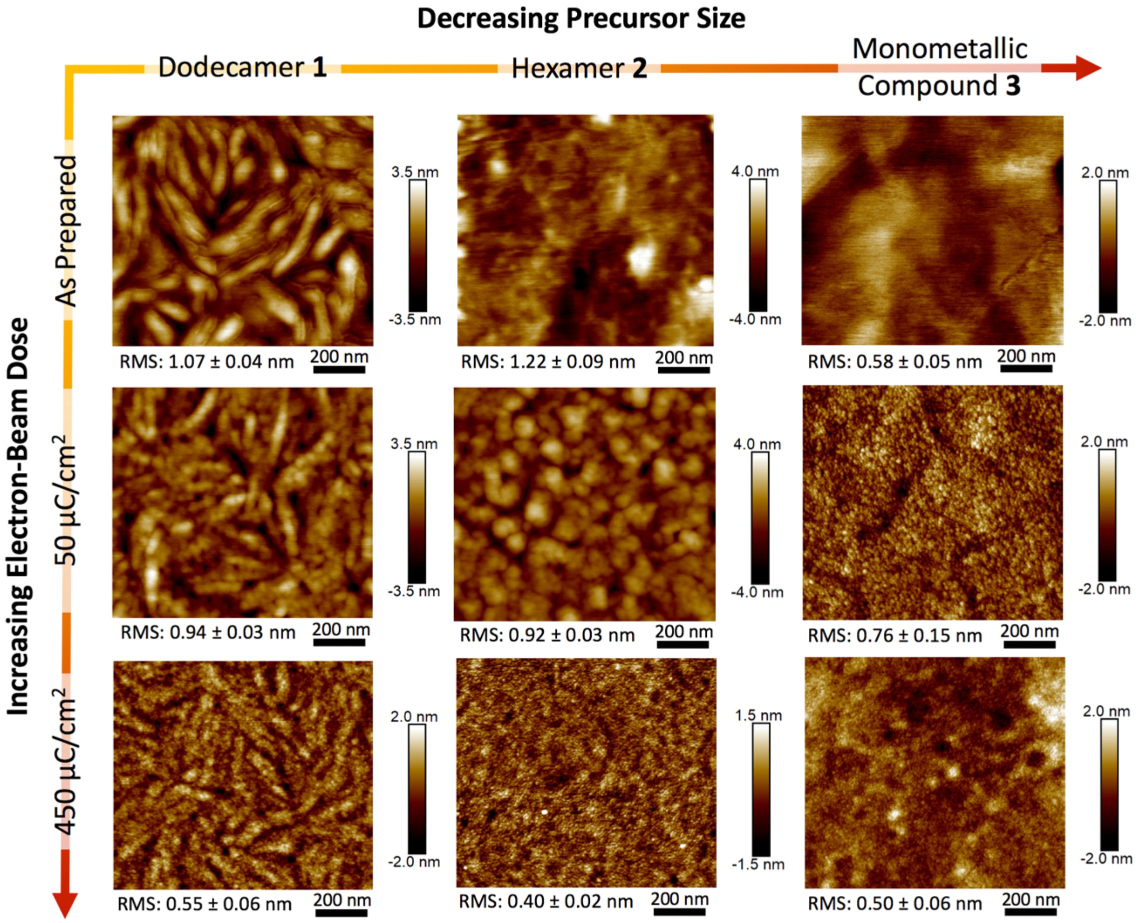

Figure 4.3. Atomic force microscopy images of films used to compare surface roughness and morphology before and after electron exposure. Cluster **1** (left) has a surface morphology that is maintained through both patterned films. Cluster **2** is shown in the center and compound **3** is shown on the right. In general, all species decrease in roughness as they are patterned to higher doses.

Thermal treatment of the precursor films allowed us to directly compare the unknown product of electron irradiation with films that were confirmed as tin oxide. Films of **1** and **2** were thermally driven to crystalline SnO_2 as determined by XRD and show significantly increased surface roughness (Figure C8). Surface features like the "hills" that are present in untreated films of **1** are completely transformed into nanostructures that have an RMS roughness of 4.4 nm. These surface structural changes are indicative of the physical changes that occur within the film when the tin carboxylate reagents transform into an oxide. During thermal processing, atoms and molecular fragments are more mobile, allowing rearrangement into an SnO_2 lattice. On the other hand, the electron beam induced almost no structural change, indicating that the electron beam is crosslinking the clusters together or is not imparting enough energy to cause a significant lattice rearrangement.

AFM revealed few physical changes in the electron irradiated films, but VB XPS (Figure 4.4) allows us to examine electronic changes by assessing the differences in the films' density of states before and after reaction with the electron beam.[38,39] Electronic changes result in differences in overall peak shape of the spectra and in the valence band maximum (VBM) of the spectra. The VBM is a value of merit that is found by extrapolating the slope of the lowest energy peak back to the x-axis for each individual spectrum.[40,41] The slopes were calculated using values between 20% and 90% of each peak's height. This method of analysis aided in removing contributions that arise from the tails that trail off at lower energies in some of the individual spectra. Other individual spectra have slight shoulders on the low energy side of the peak. These shoulders likely arise from a mixture of states as the extended material changes with patterning and were included in the linear fits to calculate the slope.

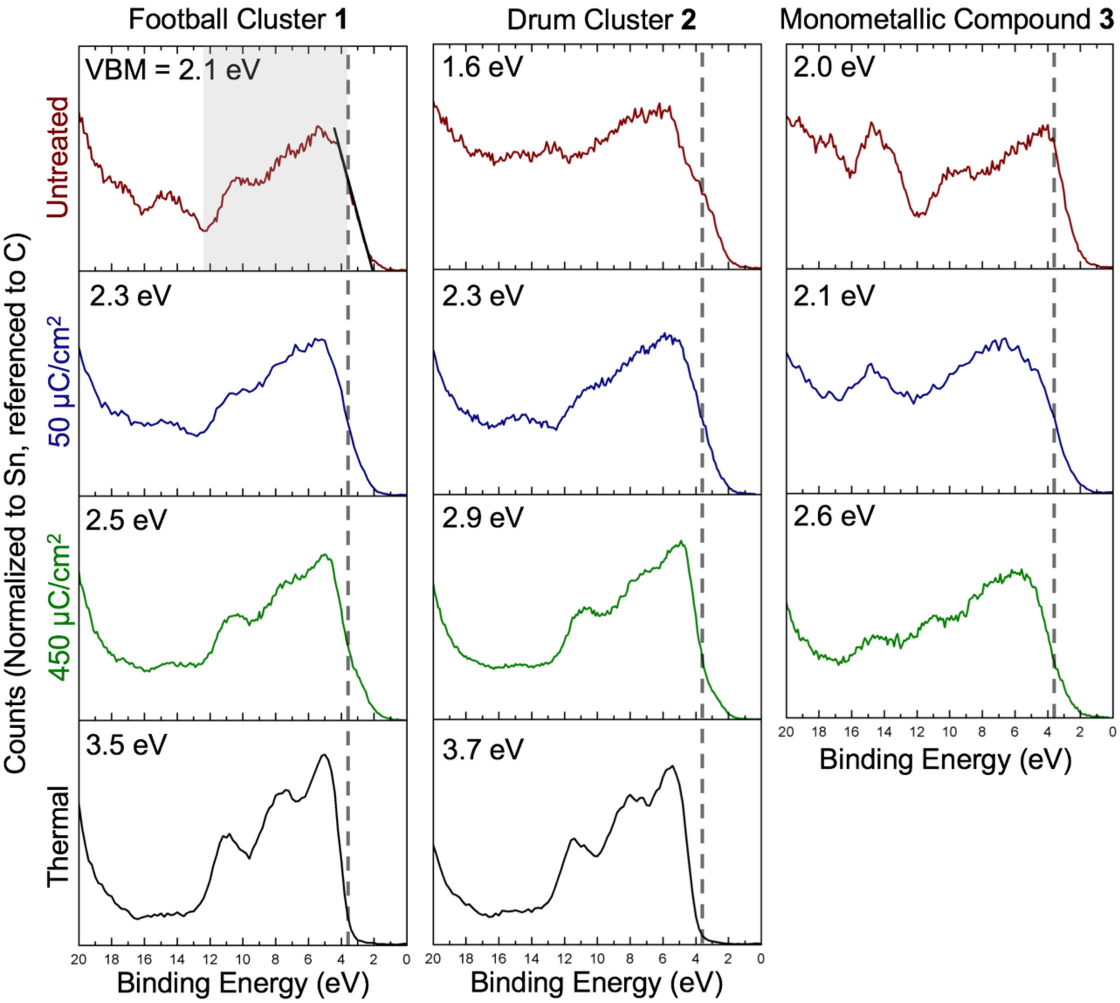

Figure 4.4. Valence Band XPS from each sample after different processing conditions. A dashed line is drawn at 3.7 eV in each column as a guide to the eye, comparing the VBM of each spectrum to the band gap of SnO_2. The top left spectrum displays a linear fit of the lowest energy slope as an example of the extrapolation method used to find the VBM of each spectrum as well as a shaded region between 4 – 12 eV highlighting where the expected three peak shape of SnO_2 occurs. Each spectrum has its calculated VBM listed. Left) The VB spectra for **1** do not change significantly with electron beam exposure, retaining the same shape and the same onset before and after exposure. Center) Cluster **2** undergoes slight shifts with increasing dose, having the same shape as the dodecamer **1** by 450μC/cm^2. Right) Compound **3** undergoes significant shifts toward the three-peak shape but does not transform as readily as the two clusters. The thermally annealed samples at the bottom show peak shapes indicative of SnO_2 formation, with VBMs that approach the band gap of SnO_2.

The overall shape of the VB spectra shifts from an undefined hump in the untreated films to a three-peak shape in the electron patterned films (Figure 4.4). These peaks match theoretically calculated spectra for SnO_2, which are dominated by peaks at binding energies associated with the O 2p nonbonding states (~4-6 eV), a hybridization of Sn 5s – O 2p states (~6-9 eV), and a hybridization of Sn 5p – O 2p states (~9-12 eV).[42,43] These peaks indicate an increase in tin oxide character as the tin carboxylates condense together. In general, the VBM also shifts to higher energies as the films are patterned. However, the values still remain between ~2-3 eV for all species, both untreated and irradiated. The VBM values are reported on each individual spectrum in Figure 4.4.

In comparison, under thermal treatment the VB of the treated films have well-defined three-peak shapes. These films have a VBM that approaches 3.7 eV, the band gap of SnO_2.[40] The differences in VB spectra shape and VBM between the thermally treated films and the electron treated films indicate that the electronic structure of the product formed as a result of the two treatment methods is not comparable. Thermal treatment induces the formation of an SnO_2 lattice (XRD, Figure C8) while also thermally decomposing the organic ligands of the precursors based upon TGA (Figure C5), both of which will affect the material's density of states. On the other hand, the AFM and XPS data indicate that electron irradiation locks the clusters together with a significant amount of carbon in the films. While irradiation does increase the tin oxide character of the films (as indicated by the growth of the characteristic three peaks), the oxide character is not well defined, and the VBM appears more similar to the untreated films than SnO_2.

Small differences in the VB spectra for the three different tin species can still be observed after electron irradiation. The VB spectrum of compound **3** changed the most in shape from untreated to exposed at 450 μC/cm^2, meaning that the monometallic species underwent the most electronic changes during electron exposure. Cluster **1** exhibited the fewest changes in its VB spectrum, indicating that the electronic structure of the dodecamer remains similar before and after patterning. The majority of **3** is ligand, with only a single Sn atom, whereas the majority of **1** is the inorganic Sn-oxo cage. A higher percentage of **3**'s local structure is affected as ligands cleave and the product forms under electron exposure, leading to greater changes in the VB spectrum. At a dose of 450 μC/cm^2, the VB spectra of both clusters **1** and **2** look identical. The VB spectrum of **3** remains less defined at this exposure. The chemical composition of **1** and **2**, determined by XPS, also indicates that their overall atomic ratios of Sn, O, and C are within error of each other by 450 μC/cm^2, despite the precursors beginning in different ratios (Figure C6). The similarities in composition and VB structure suggest that both clusters are trending towards the same product when exposed to electron irradiation, even if they do not go through the same path to get there. These two clusters contain preformed Sn-O-Sn bonds in their inorganic cores. Species **3**, which lacks this core network, does not exhibit the same structural and compositional changes. These experiments indicate that the electron beam is inducing only local changes, which affect the species with higher ligand content more greatly than those with higher metal-oxo content. While these local transformations induce a solubility change, the electronic structure of the product is not significantly altered.

AFM images and VB XPS data indicate that transformations induced by electron exposure cause few physical or electronic changes to the tin oxide matrix, respectively. However, in the case of clusters **1** and **2**, it was still unclear whether the films are amorphous or if the cores of the clusters condense together to form small crystallites of tin dioxide. We therefore performed SAED and HRTEM experiments on films of the two clusters that were prepared directly onto carbon-coated TEM grids. We examined films that were patterned at the highest dose (450 μC/cm^2) because these exhibited the most structural changes compared to non-patterned films. Lack of diffraction spots or rings in the SAED profiles of either film suggest that the products are amorphous. TEM images (Figure 4.5) reveal small crystalline regions; however, these are likely induced by exposure to the high energy electron beam because they continue to grow as long as electron beam exposure continues (Figure C9). While the high beam currents in the TEM do induce crystallization, these currents are much higher than achievable in electron beam patterning experiments. We do not expect higher electron dosages in the SEM to further induce crystallization in the films. The amorphous nature of the electron-patterned films suggests that the clusters are not condensing to form small crystallites during electron beam patterning, but are instead linking together, resulting in an insoluble film. These studies suggest it may be more accurate to consider the electron beam product of the tin reagents to be more reminiscent of an organic cross-linked metal-oxo polymer than a true dense oxide (see section titled *Electron Stimulated Desorption: Determining the Byproducts*).

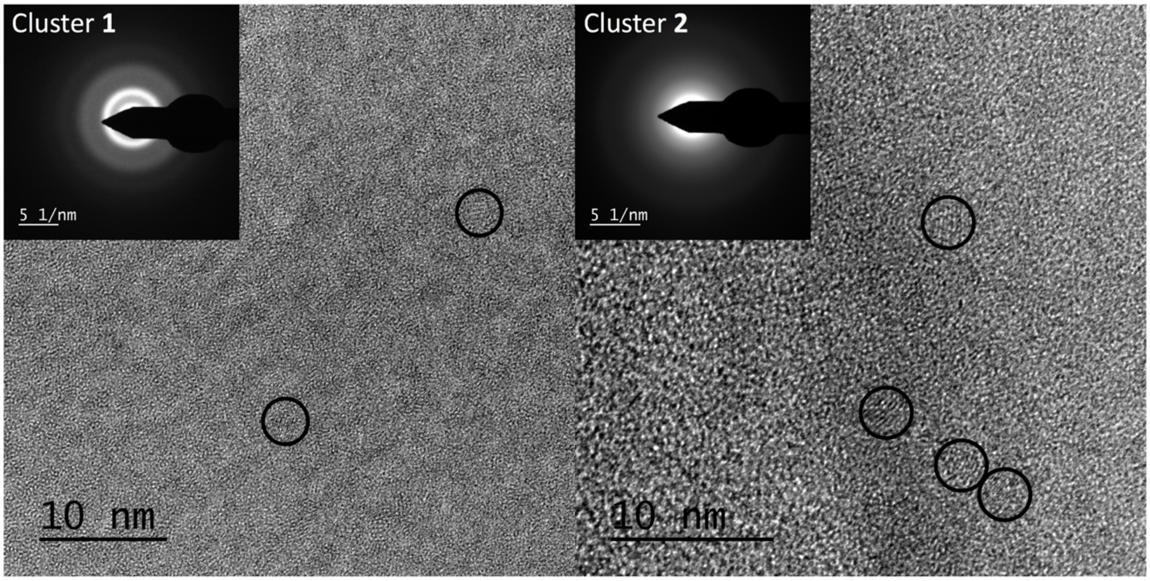

Figure 4.5. TEM images and diffraction patterns associated with clusters **1** and **2** patterned to 450μC/cm^2. The diffraction patterns are diffuse, suggesting a majority of amorphous material. Black circles surround areas of small crystals that grow under continued beam exposure.

Electron Stimulated Desorption: Determining the Byproducts

The fact that >50% of organic ligand remains in all films even after extended electron exposure made us curious about the mechanisms through which the organic ligands decompose and leave the film. Previous gas-phase photofragmentation work by Haitjema et al. on the dodecameric tin-oxo cluster confirmed loss of butyl fragments as the primary photoreaction at UV and vacuum ultraviolet (VUV) exposure energies (4-13.5 eV). They also observed that the fragmentation yield of the butyl groups increased as VUV photon energy increased from 7 to 13.5 eV.[28] XPS characterization by Zhang et al. on EUV (92 eV) patterned films of the same tin-oxo cluster shows high amounts of carbon in irradiated films, suggesting incomplete carbon loss.[44] Recent *in-situ* studies by Frederick et al. on a butyl stabilized β-Keggin tin cluster also show minor decreases in the C 1s XPS signal, from 59% to 55%, after exposure to X-rays (1486.6 eV) under ultrahigh vacuum[24] and from 60% to 45% after exposure to low energy electrons.[26] These reports show behavior similar to what we observe here even though they represent data from a variety of energies and different energy sources. While the literature is clear that butyl loss is the main mechanism determining the solubility change, the extent of ligand loss is not clear.

We used ESD to measure the masses of byproducts leaving the film during the patterning reaction in our reagents to examine the loss of each ligand. For each species, we found a response for a variety of masses upon exposure to 2 keV electrons (Figure C10). These fragments are associated with decomposition products of the butyl and acetate ligands. To provide a better analysis of ligand loss in each reagent, we calculated the total effective desorption cross-sections (a value that is useful for comparing the kinetics of desorption) for each ligand from normalized log-plots of the ESD data. The lower the value of the cross-section, the slower the desorption event. The calculations are described in more detail in Appendix C.[20]

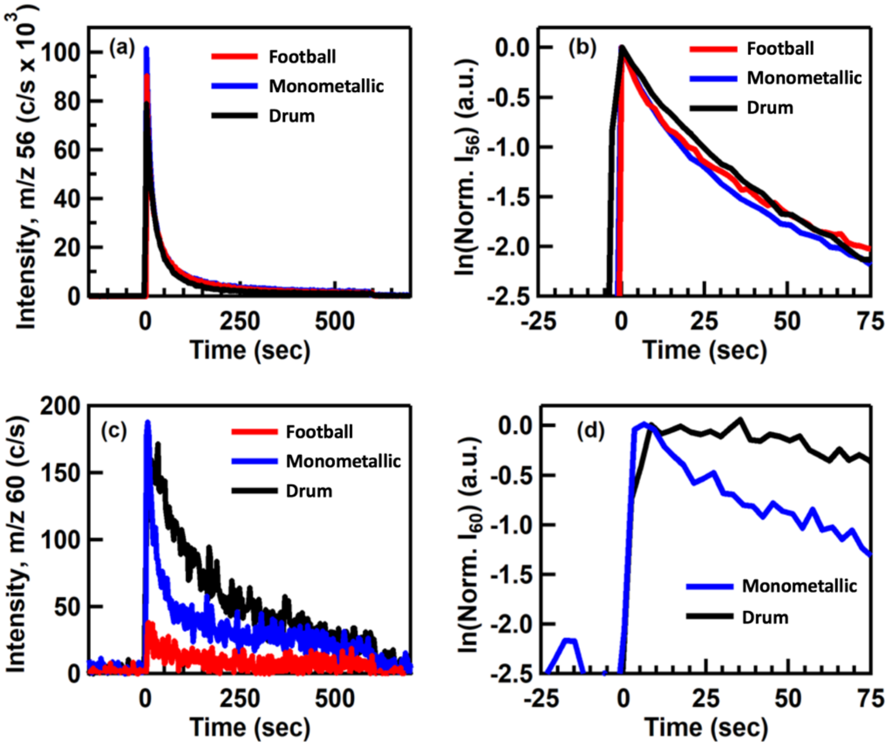

Figure 4.6. ESD data for each tin species showing both raw counts and log plots for m/z fragments associated with the butyl and acetate ligands. a) Raw counts for m/z 56, indicative of butyl ligand decomposition, are similar across all three species. b) The natural log of the normalized intensity from plot (a) shows similar decays across all species, indicating that butyl group desorption occurs at the same rate. c) Raw counts from representative m/z 60 profiles correspond to acetate decomposition. Species **2** releases the highest number of these groups, followed by **3**, followed by **1**. d) The natural log of the normalized intensity from plot (c) indicates desorption from **2**, containing bidentate acetates, is slower than for the monodentate acetates of **3**.

Representative ESD profiles for m/z 56, the fragment representative of the butyl ligand, are plotted for each species in Figure 4.6a. Upon initial exposure to electrons, a significant desorption event is initiated in films of all reagents. As butyl ligands desorb over time, fewer ligands become available for desorption and this intense event decays back to near the baseline. These decays are consistent over triplicate runs. Across all three species, the cross-section values for m/z 56 are ~1.1×10^{-13} cm^2 (Table 4.2). All cross-section values are similar and within error of each other, suggesting that the butyl groups cleave and desorb in a similar fashion despite the structural differences in the inorganic cores across the three precursors. Bond cleavage and desorption are only dependent upon the Sn-C bond, not on the total structure of the Sn reagent.

Table 4.2: Cross-section values (x 10^{-13} cm^2) for butyl and acetate ligands calculated for each cluster from data represented in Figure 4.6.[a]

m/z	*Football Cluster* **1**	*Drum Cluster* **2**	*Monometallic Compound* **3**
56 (butyl ligand)	1.1 ± 0.3	1.0 ± 0.1	1.2 ± 0.1
60 (acetate ligand)	N/A	0.11 ± 0.09	0.42 ± 0.04

[a]Data presented in this table is representative of multiple runs. Cross-sections for m/z 56 were calculated from log plots like those shown in Figure 4.6b, while cross-sections for m/z 60 were calculated from log plots like those shown in Figure 4.6d. All three species have similar cross-section values for m/z 56, suggesting that the butyl groups cleave and desorb in at similar rates. For m/z 60, the value for the **2** is lower than that for **3**, suggesting that bidentate acetate ligands cleave and desorb more slowly than monodentate acetate ligands.

ESD profiles for m/z 60, representative of the acetate groups, are plotted for each tin species in Figure 4.6c. The decay for **2** is notably slower than the decay for **3**, while **1** had a small intensity that was insufficient for cross-section analysis. For the two reagents whose cross-sections could be calculated, **3** had a value of 0.42 × 10^{-13} cm^2, while **2** had a value of 0.11 × 10^{-13} cm^2 (Table 4.2). The chelating acetate ligands in reagent **2** cleave and desorb more slowly than the monodentate-bonded acetate ligands in **3**, again supporting that bond cleavage and desorption is dependent upon bond strength.

The mass fragments that are observed as byproducts of the patterning reaction indicate that the mechanism of ligand loss observed here is consistent with the literature,[25,26,28] where electrons induce bond cleavage, followed by subsequent desorption of the different ligand groups. The cross-section values reported here (Table 4.2) for the acetate groups associated with both tin reagents are lower in value than those for the butyl ligands, indicating that overall, acetate desorption occurs at a lower rate than butyl desorption. This cross-section analysis provides further clarity over the magnitude with which the different ligand types and different ligand coordination modes affect the kinetics of the electron induced ligand loss. Additionally, we find that the desorption kinetics only change insofar as the coordination mode of the ligands change, and do not reflect differences in the structure of the tin precursors.

The presence of excess carbon observed in the XPS data suggests that the decomposition and desorption of the ligands is not complete. We probed the residual carbon in the films using ESD and temperature programmed desorption (TPD) in tandem. We performed a traditional ESD experiment, exposing two separate films to doses of 10 $\mu C/cm^2$ and 450 $\mu C/cm^2$ with 2 keV electrons. After these exposures, we examined the films by TPD (ramping from 25 to 900 °C) to remove the rest of the organic ligands and estimate how much carbon was left in the film after electron exposure. These results were compared to baseline TPD measurements of films that were not exposed to the electron beam. The results of this experiment are presented in Figure C11. After a 10 $\mu C/cm^2$ electron dose, 64 ± 5% of the butyl ligands remained in the film and were subsequently removed using TPD. On exposure to a 450 $\mu C/cm^2$ dose, 52 ± 7% of the butyl ligands remained. These data support the findings from XPS that, while irradiation does decompose the butyl and acetate groups, a significant portion of the ligands remain in the film.

Extensive electron exposure does not continue to drive ligand loss, nor does it significantly alter the composition or structure of the product compared to low electron doses, as indicated by XPS and AFM. The quantity of carbon remaining in the film is still substantial, suggesting that the reaction runs to completion at low doses. The organic ligands are either trapped in the film during patterning or are instead involved in crosslinking the clusters. This latter hypothesis is consistent with reports of patterned nanoparticles, where the main mechanism of insolubility and contrast change is dehydrogenation and subsequent cross-linking of alkyl chains in the ligand shell.[22] Similar contrast mechanisms through polymerization of butyl groups in butyl stabilized β-Keggin tin clusters have also been proposed.[26] The product of the tin reagents and electron irradiation *includes* carbon, supporting the formation of a material that is better described as a metal-oxo polymer rather than a dense, metal oxide.

Implications for Direct-Write Applications

Understanding the fundamental chemistry behind resist formation is imperative to a resist's use in lithographic and direct-write applications. The analyses from the three different stages in the resist reaction studied here can guide performance in these applications. As an inorganic resist, performance is dictated by reaction efficiency, which we have found is controlled by the structure of the inorganic reagent (both the preformed metal-oxo framework and stabilizing ligand shell) and the dose of electrons. In EUVL settings, performance can also be defined by the byproducts that form. Desorption of fragments that decompose during the irradiation reactions can contribute to outgassing that fouls vacuum chambers. These residues reside on mirrors used to focus EUV light, ultimately inhibiting maximum power outputs.[2,15] Using a material that does not lose all of its organic ligands and instead forms crosslinks to render the material insoluble would be beneficial for EUVL. Finally, the product that is formed is important for direct-write applications. While these tin reagents do not form high quality metal oxides under electron irradiation, they do result in a polymeric material with different structural and electronic properties than thermally treated films. In theory, choosing cluster or nanoparticle precursors that vary in size and volume of metal-oxo content could enable a suite of these polymers to be made with tunable electronic properties. The polymeric patterns can also be converted to an oxide by thermally baking the films at 300 °C or through O_2 plasma treatment to remove excess carbon[45] (Figure C12). This enables a two-step method with which to utilize these same precursors for direct-writing of metal oxides. In this case, a more sensitive cluster will improve the efficiency of the pattern creation step, while the annealing step will transform the material into an oxide.

Conclusions

We compared three organotin carboxylate species of varying size but with similar ligands to determine how precursor structure affects chemical transformation during electron patterning. Treating the organotin species and the electrons as reagents in the patterning reaction enabled us to reconsider aspects of the fundamental chemistry that guide the transformation. We examined the reaction at three different stages to gain a more complete picture of how these organotin species transform from precursor to product. Upon electron irradiation, the butyl groups cleave and desorb from the film, followed by the acetate groups in an order that is dependent upon bond strength. However, not all of the ligands are cleaved. The inorganic cores with partial ligand shells remain discrete and are most likely crosslinking together to form a product best described as a metal-oxo polymer, rather than rearranging or condensing to form a dense metal oxide. The structure of the organotin species affects its sensitivity to electron irradiation but does not influence the type of product that forms. The polymer product retains structural aspects of the starting species' inorganic core, introducing a level of tunability for the polymer based on precursor choice. Although these organotin carboxylates make poor quality metal oxides as patterned, they can be driven to oxides through subsequent thermal treatment.

This work demonstrates that it is important to understand the transformations taking place on the molecular scale if we want to utilize these types of materials for direct-write applications. Using irradiation sources that impart low thermal energy will not cause significant lattice rearrangement in the resist. Choosing materials with ligand shells that are sensitive to specific types of energy is imperative to forming dense metal oxides, as materials with organic ligands might crosslink instead of cleaving. While not all inorganic-based cluster or nanoparticle resists are stabilized by organic ligands, the effect of irradiation on the inorganic core cannot be ignored. With low thermal energy input, the structure of the inorganic core will also remain intact. The local structure present after patterning may have an impact on the properties of any amorphous oxide that forms after ligand loss. Understanding the local transformations that occur during patterning can help predict performance and properties because these local reactions determine the structural aspects of the overall thin film.

Bridge to Chapter V

The organotin clusters studied in Chapter IV retain their structure after patterning, suggesting that tunability of the metal-oxo content in the film is possible. Chapter V expands upon this idea, using the cluster precursors as a tunable matrix for patternable nanocomposites materials. In this chapter, two composite systems formed from solutions of clusters with colloidal nanocrystals are explored as precursors for nanocomposite films that are patternable by electron beam lithography. The two systems used are based on the hafnium and tin clusters previously described in Chapters II – IV and mixed with colloidal nanocrystals formed through a slow-injection synthesis, described in Chapter V. These have the potential to be used in printing of electronics and for fundamental investigation of composite properties. Chapter V investigates and discusses the importance of the interface between the nanocrystals and the matrix material, which has a role in the properties of the produced nanocomposites, the solution stability of the composite precursors, and the chemistry of patterning.

CHAPTER V

TOWARDS DIRECT PATTERNING OF FUNCTIONAL NANOMATERIALS AND NANOCOMPOSITES

Note: Portions of this chapter may appear in an upcoming publication authored by Meredith C. Sharps, Raina A. Krivina, Checkers R. Marshall, Brandon M. Crockett, Darren W. Johnson, and James E. Hutchison. B.M.C., M.C.S., J.E.H., and D.W.J. conceptualized the basis for this work. Experimentation was performed by C.R.M., R.A.K., M.C.S., and B.M.C. M.C.S. wrote this chapter with editorial assistance from D.W.J. and J.E.H.

Introduction

The ability to print electronics has recently garnered industry interest for producing devices both at low-cost and in high-volume.[1] Typically, electronic devices are built through multiple lithographic steps combined with vacuum deposition of inorganic materials. Directly printing electronics reduces the number of processing steps necessary to produce a device and relies upon solution processible materials, which significantly reduces the energy input and waste associated with vacuum deposition. Solution processing also opens the door to using flexible substrates for device manufacture, leading to flexible thin film transistors,[2–4] solar cells,[5,6] electrochemical devices,[7] and electronics for biomedical applications. Moreover, many types of nanomaterials are compatible with solution processing, such metallic, semiconducting, and transparent conducting oxide nanoparticles and carbon nanomaterials like nanotubes and graphene. These materials require additional processing after printing to dry, cure, or sinter the nanomaterials, but can be printed with high-throughput methods like screen printing and ink-jet printing. These methods are capable of producing features greater than one micron, but higher resolution features are necessary for integrated circuits and optoelectronics. Printing nanoscale features without a photolithographic step remains a challenge.[8]

Patterning functional inorganic materials directly through lithographic methods has the potential to address this issue. Recently, UV lithography of nanocrystals (NCs) has been investigated as a way to build devices while bypassing the need for a photoresist to define a pattern, ultimately reducing the number of steps necessary to form a functioning device.[9,10] Colloidal metallic and semiconducting NCs, synthesized with photosensitive ligands that decompose under deep UV (DUV) wavelengths, provide a low energy route to making high quality patterns. NCs have previously been studied as resist materials,[11–13] while other inorganic systems based on NCs or inorganic clusters have been utilized to form nanostructures using imprint lithography,[14,15] dip pen lithography,[16] electron beam lithography,[17–20] and inorganic infiltration of polymer-based templates.[21]

The previous chapters in this dissertation have discussed the formation of metal oxides from inorganic clusters, drawing on the utility of precursors that decompose and crosslink under electron beam exposure. These inorganic clusters are similar to polyoxometalates that have been utilized as precursors for the formation of nanocomposites, particularly NCs in glass. Nanostructures in glass have demonstrated a variety of interesting properties, including fast ionic exchange,[22] hardening of bulk glass,[23] optical nonlinearity,[24] and electrochromic effects.[25] The structural interface between the nanostructures and surrounding glassy matrix are attributed to these enhanced properties, but controlling this interface is extremely difficult. Llordés et al. demonstrated that encapsulating transparent conducting oxide (TCOs) NCs in glass was possible in a brick-and-mortar type system by using coordinating polyoxometalates (POMs) as a precursor to the glassy matrix.[25] Through thermal treatment, the POMs condensed to form an amorphous metal oxide network around the NCs. The interfacial structure could be tuned through the volume fraction of POM to NC, allowing a degree of control over the interface.

In Chapter IV, we found that electron beam patterning of organotin clusters formed a metal-oxo polymer material that retained the local structure of the cluster precursor. Controlling the local structure of an extended film through cluster choice inspired us to investigate these clusters as tunable matrices for nanocomposites. Here, we use two different NC-in-cluster systems, an aqueous system and an organic soluble system made from combinations of the cluster species used in Chapters II, III, and IV and Sn-doped In_2O_3 NCs. The aqueous system, formed from the $HafSO_x$ cluster in Chapter II, is most similar to the POM systems used by Llordés et al.[26] The organic soluble system utilizes the organotin carboxylate clusters described in Chapters III and IV.

We investigated the stability of nanocomposite precursor solutions made through mixing clusters and NCs and examined the ability to pattern these mixtures with an electron beam. We found that the interface between the NCs and the clusters has an impact on solution compatibility and patterning capability. The bulk of this chapter addresses issues associated with these interactions, both in the composite solutions and of the nanocomposite as a whole. While changing cluster structures may provide a way to alter and control the local structure of the matrix around the nanoparticles, overcoming instability in the precursor solutions remains a challenge.

Methods and Experimental

We designed two systems to investigate based on the two cluster systems discussed in Chapters II, III, and IV. The nanoparticles used in these systems were 10% Sn-doped In_2O_3 (ITO) NCs synthesized through a slow-injection esterification synthesis.[27–29] These particles, when synthesized in this manner, are stabilized by oleate ligands. The particles used throughout this study were 9 nm in diameter by transmission electron microscopy (FEI Technai G2 Spirit). We chose to use ITO because of its spectroscopic response; we could easily monitor changes in the NCs based on the color and the shift in the localized surface plasmon resonance (LSPR) via UV-vis spectroscopy. These NCs were either used directly or ligand-exchanged and mixed with two different cluster solutions to form both an aqueous cluster/NC composite precursor and an organic soluble cluster/NC composite precursor.

Preparation of the Aqueous Cluster Precursor with Ligand-Stripped NCs (HafSO$_x$/ITO)

We removed the oleate ligands stabilizing the ITO NCs with nitrosonium tetrafluoroborate ($NOBF_4$) according to methods previously described in the literature to form ligand-stripped, or 'bare,' NCs.[30] In this ligand exchange, the oleate-stabilized ITO nanocrystals dispersed in hexanes are mixed with an equal volume of *N,N*-dimethylformamide (DMF) or acetonitrile (ACN). A small scoop of $NOBF_4$ is added to the mixture and vigorously shaken. As the oleate ligands become displaced, the NCs move from the non-polar hexane phase to the more polar (DMF or ACN) phase. The NCs were then washed with hexanes and dispersed in either DMF or ACN.

A hafnium-based cluster ($HafSO_x$, described in Chapter II) was used as the stabilizing cluster in this system. A 1 M stock solution of $HfOCl_2 \bullet 8H_2O$ was prepared by dissolution of the Hf salt in 18 MΩ H_2O. A solution of 2N H_2SO_4 and 30 wt% H_2O_2 was prepared, followed by the addition of the $HfOCl_2$ solution. The final solution was diluted using 18 MΩ H_2O to a final concentration of 0.105 M H_2SO_4, 0.45 M H_2O_2, and 0.15 M Hf. To form the composite solutions, a volume of 0.75 mL $HafSO_x$ (20 mg of Hf) was added to a series of three NC solutions of the same volume (0.75 mL) dispersed in DMF or ACN, containing 5 mg, 25 mg, and 37.5 mg of ITO to form Hf/NC weight ratios of 1:0.25, 1:1.25, and 1:1.9, respectively.

Preparation of the Organic-Soluble Cluster with Oleate Stabilized NCs (Sn Drum/ITO)

The second system utilized the organotin carboxylate clusters discussed in Chapters III and IV. Acetate stabilized drum clusters were synthesized by refluxing butylstannoic acid (5 mmol) with acetic acid (5.2 mmol) in 50 mL of toluene under N_2 for four hours. Upon reflux, the solution became clear, indicating a reaction between the acids. After reflux, the reaction mixture was left to evaporate, forming square-shaped crystals. These crystals were washed with acetonitrile, dissolved in toluene, filtered, and confirmed to be the acetate drum cluster via ^{1}H and ^{119}Sn NMR (Bruker Avance III-HD 600). Composite solutions were formed by mixing a 3:1, 1:1, and 1:3 volume ratio of a 60 mg/mL solution of cluster in toluene with a 100 mg/mL solution of NCs in toluene.

Solution Characterization

For the $HafSO_x$/ITO system, solutions were drop-cast onto lacey carbon-coated

Cu TEM grids and imaged on an FEI Technai G2 Spirit microscope to observe changes in the NCs upon addition to the HafSO$_x$ solution. Changes in the Sn drum/ITO system were studied using dynamic light scattering (DLS) on a Wyatt Mobius instrument and with ^{119}Sn and ^{1}H NMR using a Bruker Avance III-HD 600 spectrometer. The different types of analysis performed on each composite precursor were chosen because of physical changes that occurred upon cluster and NC mixing. For the HafSO$_x$/ITO system, the solutions remained clear but changed in color, indicating that the NCs could be etching. We used TEM to investigate particle morphology before and after mixing. The Sn drum/ITO system exhibited aggregation and precipitation, so DLS was used to monitor the aggregation process and ^{119}Sn NMR used to study changes in the drum cluster.

Film Preparation

P-type {100} silicon (1-100 Ω-cm) with 100 nm of thermal oxide was cut into 1.5 cm x 1.5 cm squares and cleaned with a basic piranha solution (5 parts 18 MΩ water, 1 part NH_4OH, 1 part 30% H_2O_2) heated to 80 °C for 20 min. The cleaned wafers were rinsed with 18 MΩ water before being plasma cleaned in O_2 plasma for 5 min. The HafSO$_x$/ITO solutions were filtered through a 0.2 µm filter and then spin-coated at 3000 rpm for 3 min. The films were soft baked at 80 °C for one minute to remove solvent and to begin densifying the films. For the Sn drum/ITO films, the plasma cleaned films were vapor treated with hexamethyl disilazane (HMDS) for 30 min at 120 °C under standard conditions to make the surface of the films non-polar. The Sn drum/ITO solutions were filtered through a 0.2 µm filter and spin-coated at 3000 rpm for 30 s. These films were soft baked at 70 °C for 1 min to remove residual solvent. These same Sn drum/ITO solutions were also spun onto glass substrates for later observation of the LSPR. Control films containing only Sn cluster and only ITO NCs were also prepared.

Patterning Procedure and Film Analysis

The films prepared on the 100 nm thermal oxide silicon substrates were patterned using a Zeiss Ultra-55 Scanning Electron Microscope (SEM) operating at 30 kV equipped with JC Nabity Nanometer Pattern Generation Software (NPGS). Five by five arrays of 200 μm x 200 μm boxes were patterned with each box exposed to a different electron dose. The first box began at a dose of 75 μC/cm^2 and the final box ends at a dose of 435 μC/cm^2. The HafSO$_x$/ITO films were developed in tetramethylammonium hydroxide (TMAH) and hard baked for 3 min at 350 °C. The Sn drum/ITO films were developed in toluene. The films prepared on glass substrates were thermally treated at 300 °C for 10 min to remove ligand and observe changes in the LSPR of the films.

The composition of the patterned films was studied using X-ray photoelectron spectroscopy (XPS) on a ThermoScientific ESCALAB 250 instrument. The LSPR was observed on the glass slides using a Perkin Elmer Lambda-1050 UV/Vis/NIR spectrophotometer. Cross sections of the films and film thickness were determined using an FEI Helios 600 Dual-Beam FIB-SEM. High resolution (HR) TEM images and selected area electron diffraction (SAED) patterns were acquired on an FEI Titan 80-300 TEM.

Results and Discussion

Aqueous HafSO$_x$/ITO Composite Precursor System

Two ITO NC solutions dispersed in ACN and DMF were mixed with the HafSO$_x$ solution. In ACN, the NCs were unstable and precipitated out of solution immediately. In

DMF, the mixtures remained clear, suggesting that the NCs could be stabilized by the $HafSO_x$ cluster in this solvent. However, after ~3.5 hours, the blue color exhibited by the ITO NCs disappeared and the solutions became clear, suggesting that the NCs were changing in solution. By TEM, the NCs aggregate over time when exposed to the $HafSO_x$ solution and smaller particles can be seen forming away from the aggregates (Figure 5.1). The $HafSO_x$ cluster is stabilized in a piranha solution and it is likely that this acidic solution is etching the ITO NCs over time.

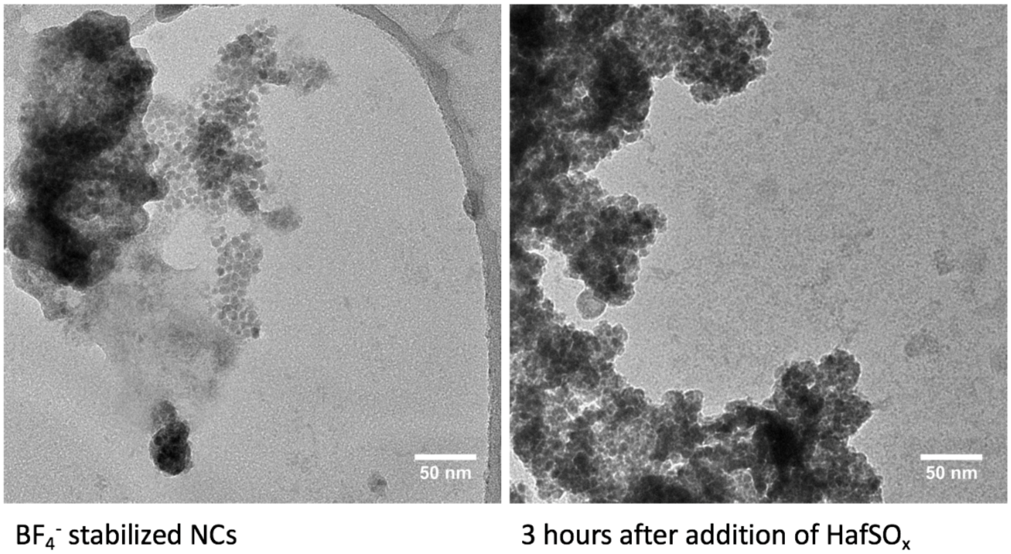

BF_4^- stabilized NCs

3 hours after addition of $HafSO_x$

Figure 5.1. SEM images of $NOBF_4$ ligand stripped ITO NCs are shown on the left. On the right, the NCs are shown 3 hours after the addition of the $HafSO_x$ solution. The NCs have aggregated together and smaller particles have formed away from the aggregates.

Despite NC instability, three solutions of the composite precursor mixture were prepared by adding different concentrations of NCs to a standard solution of $HafSO_x$. These three mixtures contained Hf/NC weight ratios of 1:0.25, 1:1.25, and 1:1.9. In order to reduce etching of the particles prior to patterning, these films were immediately spin-coated after mixing. The films formed from the 1:0.25 and 1:1.25 Hf/NC solutions were patterned with an electron beam at 30 kV. Both films revealed a pattern after development, but the 1:0.25 Hf/NC film was more sensitive to the electron beam than the 1:1.25 Hf/NC film. XPS of the 1:1.25 patterned film indicated that Hf and In were present in a about a 1:1 ratio, but the amount of Sn relative to In was decreased by a factor of 10 in the patterned films compared to the composition of the as-synthesized NCs.

The instability of the NCs in the $HafSO_x$ solution over time and the difference in composition before and after patterning suggest that the NCs are not surviving in the acidic media. The POMs used previously in the literature to make nanocomposite films are stabilized in more basic conditions than those used here, with the most acidic solution at a pH of ~5.5.[25,31,26] In our system, the ligand-exchanged NCs in DMF are stabilized at the surface both by BF_4^- and by DMF molecules prior to $HafSO_x$ addition. The NCs in DMF have a pH between 3-5 and are stable in this range,[30] but the strong oxidant formed in the piranha solution oxidizes organic materials and has been known to etch metal oxides. This reaction may have the effect of etching the NCs and oxidizing the solvating DMF molecules, further destabilizing the NC surface. The compatibility of the cluster solution and the NCs remains an issue if these systems are to be further explored. It is interesting to note, however, that the film with more cluster by weight exhibited higher sensitivity than the film with a 1:1.25 ratio of cluster to NCs. This suggests that the addition of the irradiation sensitive cluster is necessary in order to pattern the BF_4^- stabilized NCs.

Organic Soluble Sn Drum/ITO Composite Precursor System

Solutions of both the ITO NCs in toluene and the drum cluster in toluene were mixed to form solutions with 3:1, 1:1, and 1:3 Sn drum/NC ratios by volume from a 60 mg/mL solution of cluster and a 100 mg/mL solution of NCs. In solutions with greater ratios of cluster, the mixtures showed incompatibility. The 3:1 and 1:1 Sn drum/NC solutions became cloudy upon mixing, while the 1:3 Sn drum/NC solution stayed clear. DLS revealed that the 9 nm ITO NCs aggregated together upon addition of cluster but dispersed again when diluted with excess toluene. A drop of oleic acid added to the solutions improved stability. To check the stability of the cluster, a solution of the drum was studied with ^{119}Sn NMR to observe changes in the Sn peak associated with the drum cluster upon addition of ITO NCs (Figure 5.2). The single Sn peak shifts slightly downfield by ~0.1ppm upon addition of ITO NCs, indicating that there is a deshielding effect and possibly some interaction between the two species. However, no new peaks arise in the ^{119}Sn spectrum, strongly indicating that the Sn environment is retained and that the cluster is staying intact upon mixing with the NCs.

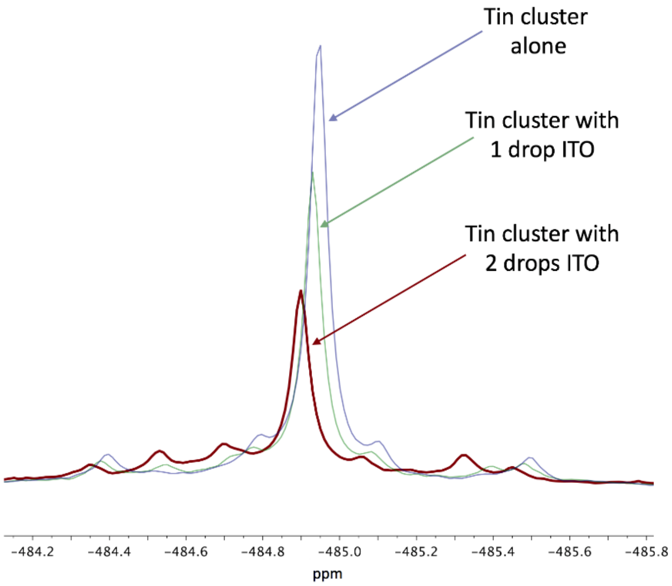

Figure 5.2. ^{119}Sn NMR of a solution of the tin drum cluster (blue) showing the single Sn environment shared by the six Sn atoms in the cluster. Upon addition of ITO to the NMR tube, the peak shifts slightly. No new peaks arise, suggesting that the cluster remains intact. The decrease in peak intensity is due to dilution in the NMR tube as NCs are added.

Each of the solutions, along with a 100% cluster solution and 100% NC solution, were spin coated onto cleaned glass slides and on 100 nm thermally grown SiO_2 on silicon. The films were thermally treated at 300 °C for 10 min under N_2 to remove solvent and a majority of the organic ligands associated with the tin clusters. These films were then studied with UV/Vis/NIR to determine the LSPR of each composite ratio (Figure 5.3). The LSPR of the films shifted slightly in the nanocomposite films compared to the 100% ITO films, but did not continue to shift with increasing concentration of the tin cluster. The tin cluster by itself did not exhibit an LSPR. The films on SiO_2 were cleaved and observed by SEM to determine film thickness and NC dispersity of cross-sections. SEM cross-sections showed that the 1:3 Sn drum/NC film exhibited well dispersed NCs with similar density to the 100% NC films, but areas of the 1:1 and 3:1 Sn drum/NC films showed clustering of NCs in certain areas of the film. We confirmed the presence of a nanocomposite through HRTEM and SAED of the cross-sections, which shows densely packed crystalline NCs that are surrounded by an amorphous matrix (Figure 5.4). By XPS, the composition has a 1:1 Sn to In ratio, confirming that Sn content from the cluster is present in the films. Smaller loadings of the NCs in the cluster matrix remains difficult due to previously mentioned aggregation at lower concentrations of NCs.

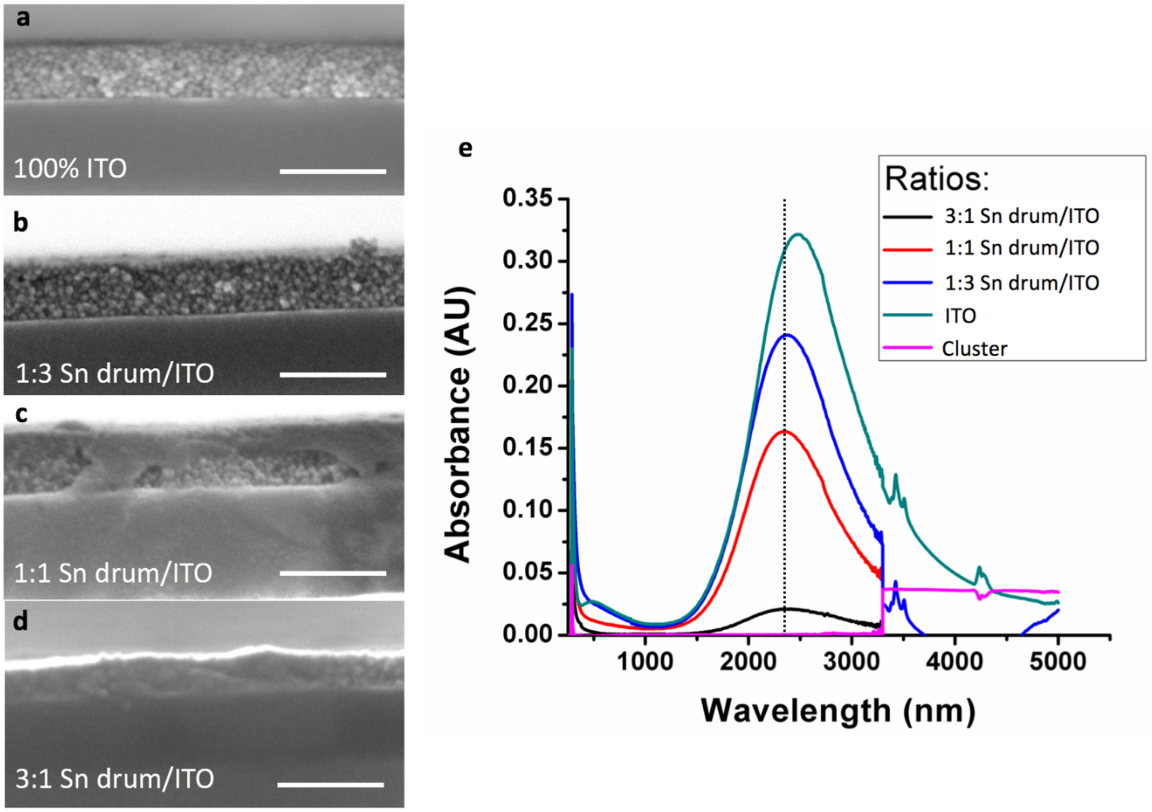

Figure 5.3. Cross sections of 100% ITO (a) and 1:3 (b), 1:1 (c), and 3:1 (d) Sn drum/ITO films by SEM. Each scale bar is 100 nm. The 100% ITO and 1:3 films look similar by density of NCs, and the NCs appear well dispersed. Upon greater addition of cluster, the NPs can be seen separating into aggregates. The LSPR (e) of these films exhibits a slight shift upon addition of cluster but does not continue to shift as cluster becomes a higher percentage of the film. A dotted line is provided to guide the eye.

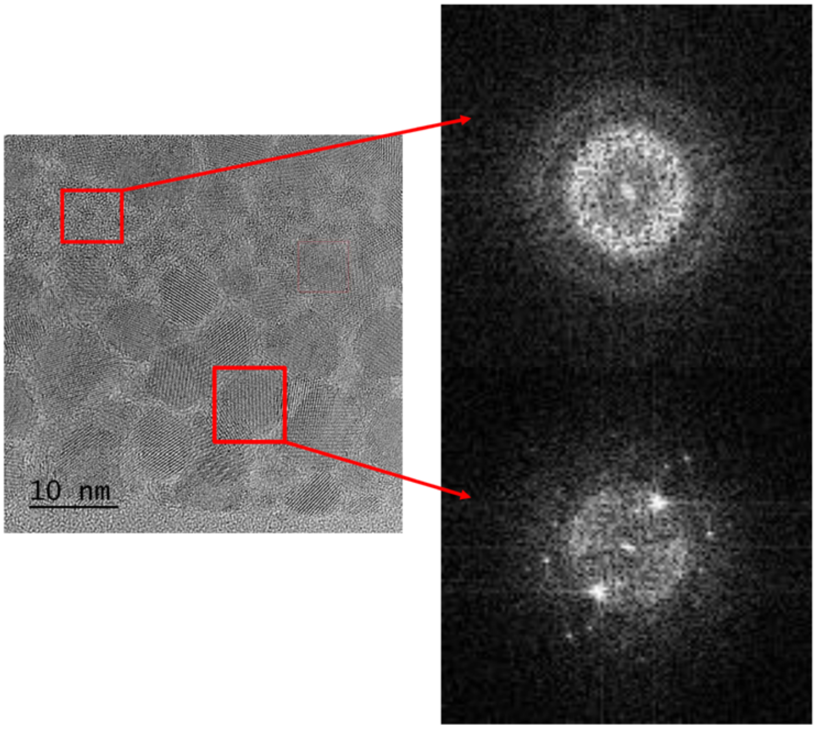

Figure 5.4. HRTEM image of the 1:3 Sn drum/ITO film is shown on the left. Corresponding SAED patterns are shown on the right. The crystalline NCs are densely packed in the film but do appear to be surrounded by an amorphous matrix suggesting the formation of a brick-and-mortar system.

The 1:3 Sn drum/NC film appeared to be the most well-dispersed, so we prepared this particular composite ratio for patterning along with a film of only ITO NCs to compare as a control. Both films were sensitive to the electron beam, but upon development we were surprised to find that the NC film was much more sensitive to the electron beam than the composite film (Figure 5.5). Previous reports have shown that NCs with long organic ligands can be patterned with electron beam and X-ray sources through dehydrogenation and crosslinking of the aliphatic groups.[17] NCs with longer aliphatic chains exhibited greater sensitivity due to a higher probability of crosslinking. We report in Chapter IV that the product of patterning the organotin clusters is a crosslinked polymer rather than a metal oxide. If a similar crosslinking mechanism occurs through the butyl chains in the drum cluster, the cluster would exhibit lower sensitivity. In the composite film, the NCs are separated from each other by the cluster matrix, and so sensitivity would be dictated by the length of the cluster ligands rather than the NC ligands.

In Chapter IV we also determined that both the composition of the ligand shell and the size of the inorganic core are important factors in the electron beam patterning reaction efficiency. Here, however, we see that the ability of the ligands to crosslink outweighs the size of the NCs. Both the 1:3 Sn drum/NC (Fig. 5.3b) and 100% NC films (Fig. 5.3a) have similar densities of NCs. Adding just a small amount of cluster, even if that cluster is known to be irradiation sensitive, reduces sensitivity because it changes the number of reactions that must occur in order for the film to crosslink.

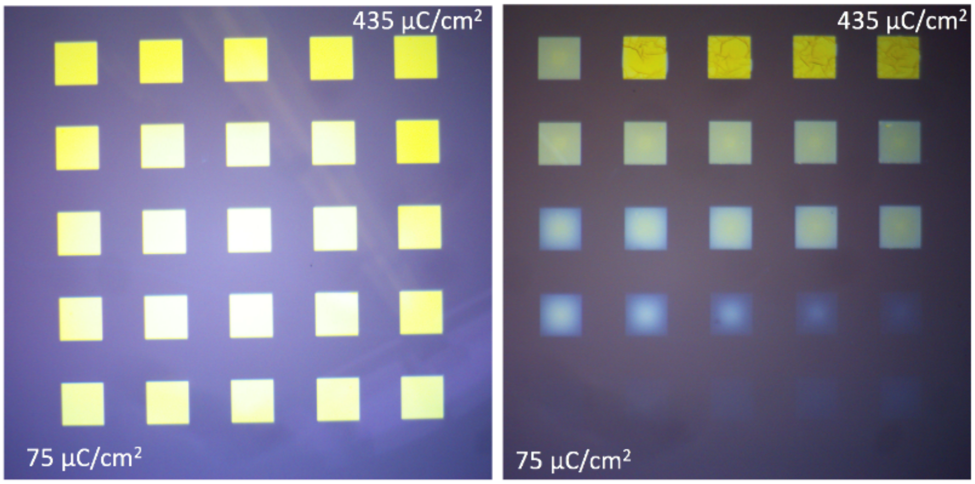

Figure 5.5. Optical micrographs of the dose arrays created from a 100% NC film (left) and a 1:3 Sn drum/NC composite film (right). The lowest dose begins in the bottom left-hand corner and continues to the right in a snake-like fashion that moves upwards. Each box increases in dose by 15 μC/cm^2 increments until the final dose of 435 μC/cm^2 in the top right-hand corner. The NC film exhibits high sensitivity, even at the lowest dose, and the films patterned look uniform and smooth. The composite films exhibit lower sensitivity and begin cracking at the highest doses. Each box in the pattern is 200 μm x 200 μm.

Because the NCs by themselves were so sensitive to the electron beam, we attempted to pattern thinner films of NCs alone. However, we found it difficult to remove thinner (<100 nm) layers of NCs from the film after patterning. Studies of the NCs spin coated onto silicon over time suggest that they adhere to the surface (Appendix D). We found the correct developing solution to mitigate the adhesion of NCs by adding a few drops of oleic acid to toluene and heating the solution to 80 °C.[32] While it is difficult to remove all of the adsorbed NCs, this method provides a way to visualize the patterns created and removes most of the non-patterned NCs from the surface of the film.

It has been shown that areas of patterned NCs show unique properties compared to non-patterned areas. Patterned areas show self-orientation and equal spacing compared to prepared monolayer films,[33] a phenomenon we also observed in patterned, thin (<20 nm) layers. Cross-linking of the long aliphatic chains is thought to stabilize the particles, as patterned areas of NCs have shown more stability when exposed to water and air[34] and impermeability to cation exchange.[35] Because of the stability that the patterned NCs show, a secondary development step, perhaps with a weakly acidic solution, could potentially be used to remove the rest of the non-patterned particles from the surface.

Conclusions and Future Outlook

In each of the systems described above, the ligand shell is a large contributor to the ability of the materials to be patterned. The interaction between the surface of the NCs and the cluster solution plays a role in both stability and in the sensitivity of the cross-linking reaction. Our goal in this work was to combine the properties of patternable inorganic resists with nanoparticles to create unique nanocomposites in a brick-and-mortar system. We found that, depending upon the system, the addition of cluster can improve or reduce material sensitivity to the electron beam based on changes to the surface of the NCs.

In the aqueous system, sensitivity was enhanced upon the addition of more HafSO$_x$, but the acidity of the solution ultimately destroyed the NCs over time. In the organic soluble system, adding a small amount of the Sn cluster inhibited sensitivity because it affected the number of reactions that had to occur in order for the overall film to crosslink. When designing composite systems through this solution-based method, it is important to determine the compatibility of the materials prior to mixing. For making brick-and-mortar nanocomposites, synthesizing the clusters and/or NC precursors with compatible ligands may enable stabilization prior to patterning. This stabilization will impact the ability to control NC loading on films while still allowing for the study of local matrix structure on film properties.

While the clusters are not necessary for electron beam patterning of NCs, they may be useful for UV patterning because NCs with aliphatic chains are not sensitive to UV sources on their own. Further understanding the reactivity of the NCs alone could lead to high resolution patterning of lines of NCs, formation of single, isolated NCs on surfaces, or construction of interesting architectures based on layered films of different types of NCs. Additionally, the enhanced stability of patterned NCs is still not well understood. There is much opportunity to study changes in both the ligand shell and the core material of NCs during exposure, expanding our understanding of the requirements necessary to design new functional materials for direct patterning applications.

Bridge to Chapter VI

Chapters II through V have discussed the formation of metal oxide nanomaterials through direct-write, electron beam lithography. These nanostructures are formed from inorganic cluster precursors that undergo a reaction with the electron beam. Chapters II and III looked at the tunability of the reagents (both the electron beam and inorganic cluster materials), Chapter IV examined the chemistry of the reaction, and Chapter V expanded upon the utility of direct-write materials. The nanostructures formed in these chapters are synthetic, but metal oxide nanomaterials also exist in nature and the formation process of some of these nanostructures is also not well understood. Chapter VI performs a nanoscale analysis on naturally forming manganeous oxide varnish that is growing as a thin film on the Smithsonian Institution Building, commonly known as the Castle. This building is considered cultural heritage and also happens to be one of the few instances of a manganeous oxide varnish growing on architectural stone. This chapter uses electron microscopy not as a fabrication tool, but rather as an analysis tool to look at the structure and composition of the oxide layer in an effort to better understand the origin of formation.

Focused ion beam (FIB) preparation for electron microscopy studies is not often performed on cultural heritage materials because it is considered a destructive technique. On appropriate samples, however, FIB preparation can be used to study structural aspects that other microanalytical techniques cannot access. Chapter VI uses TEM of SEM/FIB-prepared samples of the Smithsonian Castle to investigate varnish thickness, local nanoscale composition, and mineralogical phase. By comparing the results of these analyses with samples of known origin, varnish genesis on the Castle is better informed. This chapter presents an example of how SEM/FIB-preparation can be used to answer questions about cultural heritage, with implications for astrobiology, geology, and paleoclimate studies.

CHAPTER VI

A NANOSCALE ANALYSIS OF MANGANEOUS OXIDE ROCK VARNISH ON THE SMITHSONIAN CASTLE, WASHINGTON, DC: DETERMINING STRUCTURE AND COMPOSITION

Note: This chapter is expected to appear in an upcoming publication authored by Meredith C. Sharps, Edward P. Vicenzi, and Carol A. Grissom. M.C.S. and E.P.V. performed experiments on samples provided by C.A.G. The chapter is written by M.C.S. with editorial assistance from E.P.V. and C.A.G. E.P.V. conceptualized the basis for this work.

Introduction

The evolution of nanoscience has led to innumerable new materials and processes that enable the technologies on which our daily lives run. With the advent of modern nanotechnology, characterization of materials on the nanoscale has consequently improved and continues to do so with each passing year. Improvements in these characterization techniques, such as electron microscopy, electron microprobe analyses, and X-ray spectroscopies, have not only led to a deeper understanding of how we use and design new materials, but also how we investigate and understand old ones. Properties of materials, whether novel or ancient, arise from their chemical structure, and the ability to investigate structure on the nanoscale is imperative in determining how and why these properties arise. In cultural heritage, the ability to glean nanoscale structural and compositional information that cannot be obtained from bulk measurements provides insight into the durability of ancient materials, the methods that were used to produce them, how best to preserve and maintain artifacts, and even how present materials will age and change as they become the artifacts of our future.[1]

Scanning electron microscopy (SEM) and transmission electron microscopy (TEM), particularly paired with energy dispersive x-ray spectroscopy (EDS), have become important tools in analyzing morphology, structure and composition in cultural heritage.[2] While the study of cultural heritage relies heavily on non-destructive methods, developments such as focused ion beam (FIB) preparation of thin (<150 nm) cross-sections can provide a wealth of information from small (tens of microns) amounts of material. Although this method is destructive in nature, cases where FIB/TEM can been used, either on a sample of an artifact or on a material analogue to an artifact, have answered key problems about micro and nanostructure that in turn help identify provenance, material condition, historical processes used to create artifacts, or methods of future preservation.[3–6] Here, we turn to FIB/TEM to answer questions about the origin of rock varnish growing on the Smithsonian Castle, a piece of architecture important to the history of the United States.

The Smithsonian Institution Building, commonly known as the “Castle”, was completed in 1855 as the first home for the Smithsonian Institution in Washington, D.C. Designed by James Renwick Jr. in a Romanesque style, the Castle housed exhibits, laboratories, lecture halls, and also served as the residence for the Smithsonian’s first Secretary, Joseph Henry. The Castle is still the signature building of the Institution, currently housing both the main administration offices and the visitor center. Perched midway between the United States Capitol and the Washington Monument on the National Mall, the Smithsonian Castle stands out due to its distinctive red stone color and architectural style. The building is comprised of red Seneca sandstone, an arkosic micaceous sandstone, from the Bull Run Quarry in Seneca, MD. The stone was chosen for its durability, color, and price.[7] The raising of the Castle coincided with the beginning of the "brownstone decades," five decades of popularity for this reddish-brown sandstone in D.C. and in other east coast U.S. cities. Recently, it was recognized as a heritage stone due to its significance and prominence in early American architecture.[8]

In 2013, portable x-ray fluorescence (XRF) field measurements of dark discoloration on the surface of the Castle indicated elevated levels of manganese, a signature consistent with rock varnish.[9] Energy dispersive x-ray spectroscopy (EDS) confirmed these findings. Rock varnish is a dark surface coating characterized by accumulated levels of manganese oxide and iron oxide that mix with and cement clay minerals to host rock surfaces.[10,11] Rock varnish was first observed over two centuries ago[12] and has been studied throughout a wide variety of fields due to its importance in understanding anthropology,[13,14] paleoclimate and paleoenvironment,[15] geological dating,[16,17] and astrobiology.[18,19] It is considered the slowest growing sedimentary deposit, with growth rates estimated between 1-40 μm every 1000 years on subaerial rock surfaces.[20] Only recently has it been observed in urban environments on architectural stone,[21,22] but we note that similar discoloration is observed on other buildings and structures around Washington, D.C. that are composed of the same sandstone. Despite being studied for over two centuries, the genesis of varnish formation is still debated because of its slow growth and because it is ubiquitous: it occurs in a variety of climates and locations all over the world.[23,24]

Clay minerals are the dominant phase of rock varnish, comprising about 70% of the total composition.[10] These minerals arrive to rock surfaces via atmospheric transport[10,25,26] and are then slowly cemented to the surface through manganese oxide and iron oxide formation.[11] It has long been debated how manganese enhancement occurs in the varnish, as it is typically found in a >50x increase over manganese concentrations in the underlying rock or soil. The manganese phases in varnish are typically poorly-crystalline but are predominantly layered or tunneled oxide structures related to the birnessite and todorokite phases of Mn minerals.[27] Three main hypotheses exist to explain manganese enhancement in varnish genesis: 1) enhancement occurs abiotically through local physicochemical changes at the surface of the host rock, oxidizing Mn (II) to Mn (IV),[28,29] 2) enhancement occurs through biological mediation, where microbes or fungi produce birnessite-family minerals at the surface of the stone,[30,31,32] or 3) the polygenetic model, combining aspects of both the abiotic and biotic hypotheses.[11]

The rock varnish on the Smithsonian Castle offers a unique opportunity to study a sample of varnish growing on architectural stone in an urban area and one that is young in formation, as the Castle was erected less than 165 years ago, compared to samples that have had millenia in which to form. In 2017, a microanalytical study of a SEM/FIB cross-section of Castle varnish was completed using a combination of techniques to look at nanostructure and elemental distribution.[23] The study's aim was to characterize a variety of rock varnish samples in order to classify differences based on region and environment. The Castle varnish exhibited a structureless matrix and contained high amounts of Pb, consistent with proximity to urban areas. An in-depth microscale analysis of varnish on the Enid A. Haupt Garden gateposts, which were erected across from the Castle in 1987, determined that the varnish on the Seneca sandstone deposited in two different forms: as a discontinuous nanoscale thin film <<1 μm thick and as nanoparticles that embedded along grain boundaries, extending up to 250 μm into the sandstone.[21] The varnish is poorly crystalline, lacks microstratigraphy, and is much thinner than typical varnishes, likely due to the shorter timeline of formation.

Each of these previous studies indicate that a wealth of information lies within the nanoscale structure of the rock varnish, which can help better determine varnish genesis. In the study presented here, we perform a nanoscale analysis of the varnish on the Smithsonian Castle using TEM of SEM/FIB-prepared samples in combination with other spectroscopies. The structural and compositional data gleaned from these studies revealed that the varnish is thin, <1 μm on the surface of the sandstone, is high in concentration of Mn rather than being intimately mixed with clays, and is primarily composed of birnessite, a layered Mn oxide. This study also informed the nanostratigraphy, revealing the relative timeline of formation within the past ~170 years. The ability to perform this nanoanalysis reveals differences in composition and structure that were not clear from bulk examination and which highlight the benefits of using SEM/FIB preparation to examine cultural heritage materials, when appropriate to do so.

Methods and Experimental

We analyzed a sample of the west-facing façade of the Smithsonian Castle that was well-covered with varnish. The surface of the sandstone is rough, with areas ranging in height up to ~1mm. Images of the sample were first acquired with a HIROX optical microscope prior to being carbon coated and imaged using a Hitachi S3700N tungsten source scanning electron microscope (SEM) equipped with a backscattering detector. Four-image reconstructions of SEM images were created with the Digital Surf MountainsMap software to map out the topography of the sample. These images were used to locate areas that were relatively flat (~10s of microns) compared to the roughness of the total sample and that had good coverage of varnish.

In order to find areas that were thickly covered with varnish, we probed atomic composition with EDS-based X-ray analysis on the same Hitachi SEM (equipped with a 10 mm^2 Bruker XFlash 4010 SDD) at accelerating voltages ranging from 5-20 kV. Because the Mn is concentrated at the surface, we determined at what voltage the signal from Mn dropped off and was overwhelmed by signal from the sandstone substrate. The data was modeled in DTSA-II software from NIST, approximating the varnish on sandstone as a thin film of MnO_2 with a density of ~3 g/cm^3 (the density of birnessite) on an SiO_2 substrate. Using this method, we estimated varnish layer thickness to be between 1.7-2.3 μm and chose areas for FIB removal that were in this range. The same Hitachi SEM instrument is equipped with a Bruker μ-X-ray fluorescence (μ-XRF) system that was used to probe the atomic composition of bulk Seneca sandstone sourced from the quarry in Seneca, MD.

Ultrathin cross-sections were prepared on previously identified areas using an FEI Helios Nanolab 600i FIB-SEM. As the lamellae approached electron transparency, low energy milling was used to avoid excessive gallium implantation and to avoid damaging any crystallinity in the sample. The prepared samples were imaged using an FEI Titan 80-300 TEM in high angle annular dark field (HAADF) STEM mode and in bright field

(BF) mode at 300kV. Each cross-section was then examined using STEM-EDX analysis to probe composition, selected area electron diffraction (SAED) to determine crystallinity, and high resolution (HR) TEM to observe structure. These measurements were taken at the Center for Advanced Materials Characterization in Oregon (CAMCOR), located at the University of Oregon.

Results and Discussion

Nanoscale Structure and Crystal Phase Determination

Four FIB cross-sections were taken from a sample of the west façade of the Smithsonian Castle from an area that was darkly coated in varnish, shown in Figure 6.1.

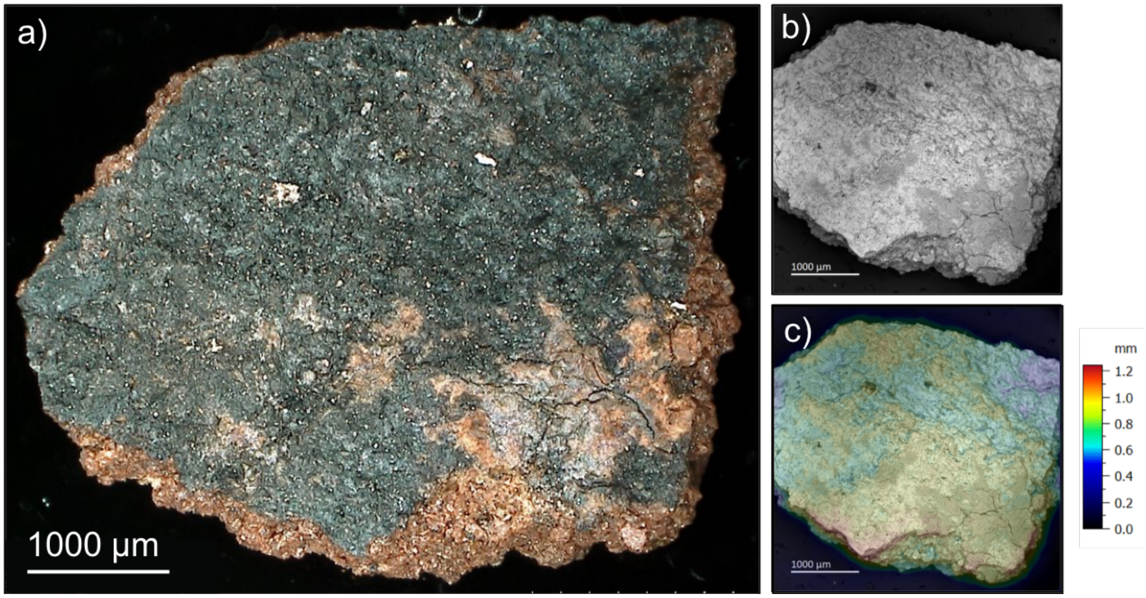

Figure 6.1. a) RBG optical microscope image of the sample analyzed. The dark surface coating can be seen in contrast to the red Seneca sandstone underneath. b) Backscattered scanning electron microscope image of the same sample. The areas that are lighter in contrast correspond to the areas rich in Mn. c) Three-dimensional image overlaid on the backscattered electron image. Areas in red correspond to the tallest areas on the sample, while areas in blue correspond to the lowest areas. The 3D image was created through a four-image reconstruction using MountainsMap software from Digital Surf.

The varnish layer is clearly visible upon first imaging the FIB cross-sections with SEM (Figure 6.2a). To determine the crystal phase of the material, we first took SAED measurements at 27 different points in the varnish layer across all four FIB lamellae. Rock varnish and naturally formed manganese oxides in general are typically poorly crystalline and are difficult to observe through bulk x-ray diffraction,[33] but we observed a consistent, diffuse, three-ring pattern (Figure 6.2b). The ring pattern indicates that the varnish layer is polycrystalline on the nanoscale. These SAED patterns were indexed to average lattice spacings of 1.4, 2.4, and 3.5 Å. Figure 6.3 shows a high resolution (HR) TEM image of the varnish film. Defined layers with spacings ~7 Å apart can be seen throughout the varnish film. This 7 Å distance, along with the distances indexed in the diffraction patterns, are consistent with the birnessite phase of manganese oxide, shown in the example crystal structure in Figure 7c. We did not observe measurements indicative of todorokite or other phases commonly found in rock varnish literature, neither did we find tunneling structures present in the manganese film. The consistency of the diffraction patterns and the layered spacings indicate that the birnessite phase is relatively pure across the four lamellae analyzed.

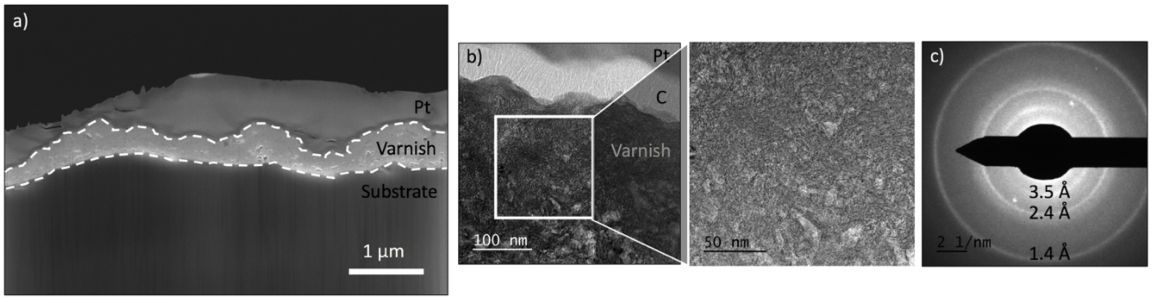

Figure 6.2. a) Secondary electron image of a FIB cross-section of the varnish layer. A thin layer of carbon and a layer of platinum were deposited on top of the surface. These are labeled in the image. b) Bright field TEM image of the top area of the varnish. The inset shows the area that was taken for the corresponding diffraction pattern. c) The three ring in the SAED pattern can be indexed to birnessite.

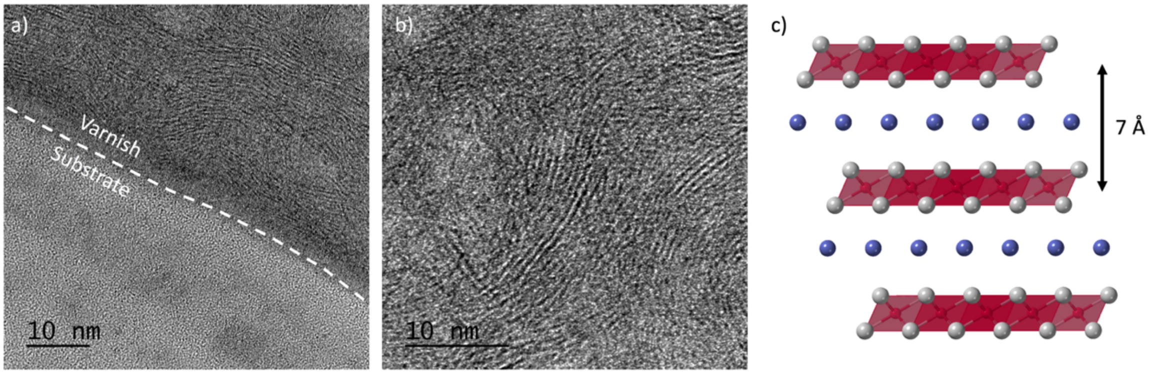

Figure 6.3. High resolution TEM images. a) The interface where the varnish layer meets the substrate, in this case a grain of quartz (SiO_2). b) A higher magnification image of the layering in the varnish layer alone, showing the visible layers that are spaced ~7Å apart. c) Structure of birnessite, showing Mn sheets spaced 7Å apart with cations in the interlayer spacing. Mn (red), O (grey), arbitrary cation (blue).

Composition and Varnish Disposition

We analyzed the composition of the varnish film using STEM-EDX of the FIB cross-sections. The varnish layer shows high atomic percentages of Mn, with only about 1% coming from each Fe, Si, and Al (Table 6.1). This was surprising, as we expected more of a mixture of clays with Mn based on other representative varnish samples throughout the literature.[11] Mapping analysis (Figure 6.4) revealed that the most abundant element in the Mn-rich layer besides Mn and O is Ca, suggesting that the major phase of the varnish is a Ca-rich birnesssite. This Ca enrichment is consistent with observed correlations by Raymond et al. and common among many different classes of varnish as confirmed by Macholdt et al.[23,34] Calcium can reside as an adsorbed species between the layered Mn oxide and also sit at octahedral sites in the matrix. Although Ca is the most abundant interlayer element observed throughout the Mn matrix, we also found many different trace elements distributed uniformly, including Si, Al, P, S, Fe, Mg, Na, Ba, K, Pb, and Zn. These elements also likely sit between the Mn oxide sheets, in Mn octahedral vacancies, or at edge sites.

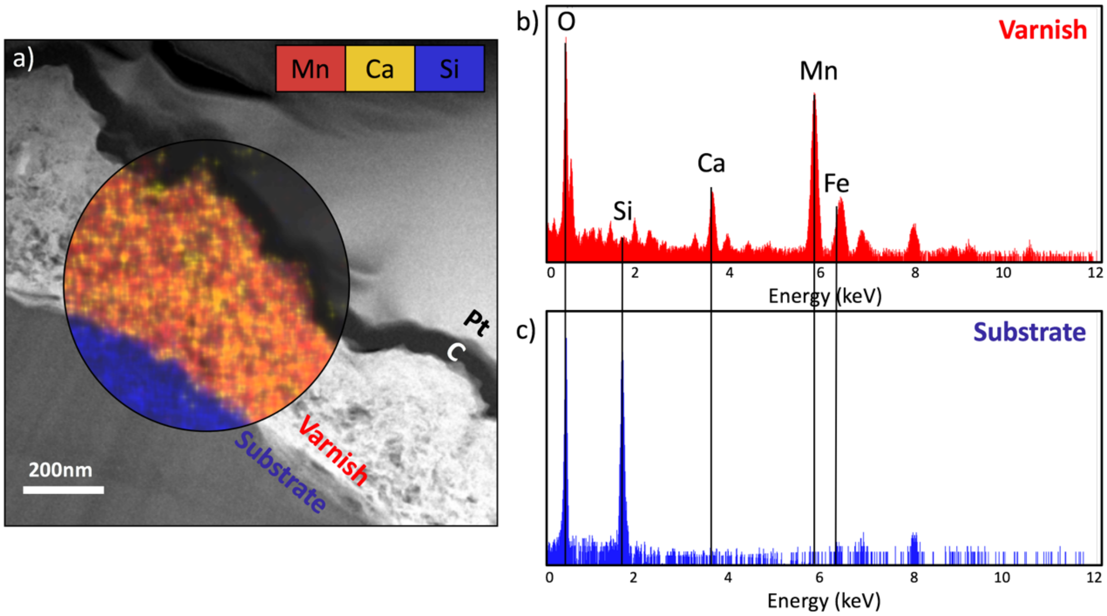

Figure 6.4. a) High angle annular dark field (HAADF) STEM image of a FIB lift-out cross-section. The encircled area represents a composite X-ray overlay of Mn, Ca, and Si. b-c) Corresponding EDX spectra are shown for the varnish layer and for the substrate layer. Corresponding X-ray spectra integrated across b) the Mn-rich varnish layer (red-filled) and c) the silica substrate (blue-filled). Lines are drawn as a guide to the eye to show where elements O, Si, Ca, and Mn are located in energy. Atomic percentages for elements found in the varnish layer are shown in Table 6.1.

Table 6.1. STEM-EDX analysis for elements found in the Mn-rich layer of the SEM/FIB cross sections. Values are reported as atomic percentages.

Element	O	Mn	Ca	Fe	Si	Al	Ba	Pb	S	P	K	Zn	Mg	Na
Site 1a	58.4	30.7	5.1	1.4	0.3	0.9	0.2	0.1	0.3	1.5	0.5	--	0.7	--
Site 1b	59.1	29.0	4.9	0.9	1.2	1.1	0.3	0.2	0.6	1.0	0.5	0.1	0.6	0.1
Site 1c	54.0	29.0	4.0	1.6	0.7	0.7	0.1	0.1	0.3	1.0	0.4	0.1	0.4	0.1
Site 2a	58.8	28.8	5.1	0.3	1.2	1.2	0.6	0.1	1.4	1.4	0.3	0.1	0.4	0.1
Site 2b	58.3	28.5	5.1	0.4	2.1	1.2	0.4	0.1	1.2	1.4	0.2	0.2	0.5	0.2
Site 2c	59.3	28.7	5.2	0.4	1.6	1.2	0.3	0.1	0.9	1.3	0.3	0.2	0.4	0.1
Site 2d	56.6	30.0	5.3	0.5	2.2	1.2	0.4	0.1	1.0	1.4	0.3	0.2	0.5	0.1
Site 3a	61.3	28.5	4.1	0.3	0.5	1.2	0.3	0.1	0.6	1.3	0.3	0.2	0.7	0.1
Site 3b	57.5	29.8	3.8	0.4	1.1	1.3	0.3	0.1	0.3	1.1	0.3	0.2	0.6	3.1
Site 3c	61.3	27.7	4.3	0.4	1.0	1.4	0.5	0.1	0.8	1.2	0.3	0.2	0.6	0.3
Site 4a	60.6	27.0	5.3	0.5	1.2	1.3	0.2	--	0.9	1.4	0.4	0.1	0.5	--
Site 4b	60.0	28.2	5.5	0.4	0.7	1.4	0.1	0.1	1.0	1.2	0.4	--	0.4	0.2
Average	**58.8**	**28.8**	**4.8**	**0.6**	**1.2**	**1.2**	**0.3**	**0.1**	**0.8**	**1.3**	**0.4**	**0.2**	**0.5**	**0.4**
St. Dev.	2.1	1	0.6	0.4	0.6	0.2	0.1	0.03	0.4	0.2	0.1	0.1	0.1	0.1

STEM-EDX mapping also revealed that many of these elements were contained in separate, nanoscale phases that are incorporated into the Mn-rich matrix. Area analysis of these nanoscale phases indicated elemental signatures associated with hematite (Fe_2O_3), gypsum ($CaSO_4$), and barium sulfate ($BaSO_4$), which in some cases colocalized with Pb and Sr (Figure 6.5). Barium is often present in rock varnishes to a varying degree based on type of varnish and location where the varnish is found.[23] Cationic Ba^{2+} typically resides in interlayer or inter-tunnel sites in the Mn oxides due to its large atomic radius and in this cationic phase is thought to stabilize tunneled structures associated with todorokite.[31] We do find trace Ba in the Mn matrix observed here, however we only observed the sheet structure associated with birnessite by HRTEM. We also find that the presence of Ba is unique to the Mn-enriched surface layer. A series of μ-XRF measurements across a sample of the bulk sandstone taken from the Seneca Quarry show that no Ba is present. Garvie et al. hypothesized that the presence of $BaSO_4$ is indicative of diagenesis: the dissolution of Ba-bearing Mn oxides and subsequent reformation as $BaSO_4$.[35] Here, however, we do not observe other evidence of diagenesis, and so hypothesize that the presence of $BaSO_4$ as a nanoscale phase in the surface layer is arriving as particulate matter from the atmosphere, rather than as Ba^{2+}. This is supported by recent analysis of particulates found in the atmosphere around the Castle, which indicate that a likely source of Ba comes from a "vehicle-related" class of particles.[36] $BaSO_4$ is commonly found as a filler in brake pads of automobiles[37] and can be released into the atmosphere through frictional wear.[38,39]

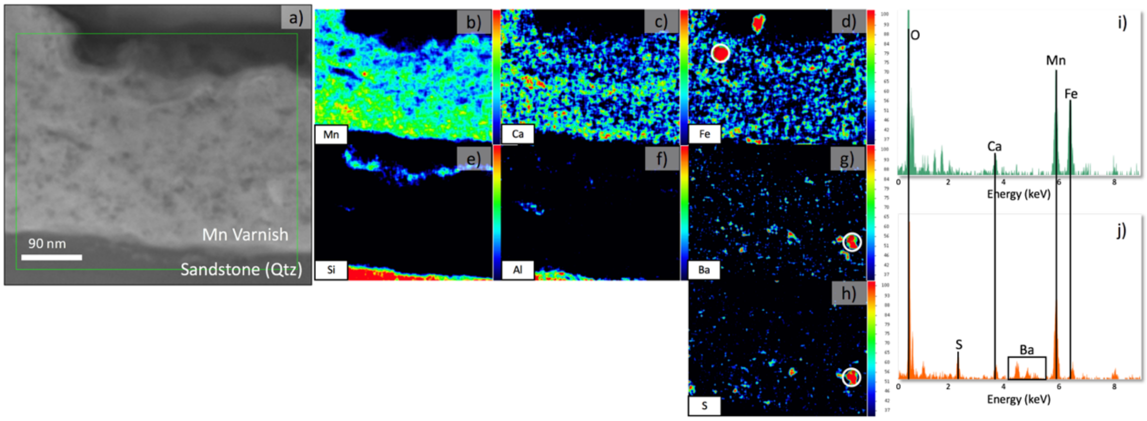

Figure 6.5. a) STEM image of a representative section of the varnish layer. Single element EDX maps showing high concentrations of Mn and Ca (b,c) and low concentrations of Si and Al (e,f). A thin, silica glaze is apparent in e). Fe, Ba, and S are shown in d), g), and h), respectively. These demonstrate the nanoscale pockets of each element. i) EDX spectra of the area circled in d), showing an iron-rich particle. j) EDX spectra of the areas circled in g) and h), a $BaSO_4$ particulate.

Nanostratigraphy and Timeline of Formation

Prior to cross-sectional TEM, our estimation of layer thickness based on plan-view EDS and stochastic modeling with DTSA-II software was between 1.7 and 2.6 µm. The cross-sections of these areas, however, revealed that across all four FIB lamellae, the film is <1µm thick, ranging from ~150 nm at its thinnest to ~900 nm at its thickest. This difference between our estimation and experimental measurements likely arises from assumptions about material density and the thin film model approximation. It is important to note, however, that the FIB lamella taken by Macholdt et al. from the same façade of the Smithsonian Castle shows a much thicker layer of varnish (~4 µm),[23] so there is a large range of film thickness across the sandstone and the thinner films observed in this study are due to the limited analysis from the sections of material available.

Of the four lamellae we took, two samples are films on top of quartz or feldspar grains and two are on layers of sediment. STEM-EDX analysis of this sedimentary deposit reveal nano- and micro-scale granules of quartz, feldspar, hematite, gypsum, clays, and barites (Figure 6.6). From the μ-XRF analysis, we know that Ba is not present in the underlying rock. The Ba-rich areas in the sediment point towards aeolian deposition, and its location underneath the Mn-rich matrix implies that it deposited prior to Mn oxide formation. This further supports our hypothesis that $BaSO_4$ is arriving from an atmospheric source. Additionally, the mapping image in Figure 4 shows a thin layer of silica forming on top of the birnessite layer, suggestive of a silica glaze. This nanostratigraphy points towards relative timeline of formation: the sediment with Ba-rich areas must have been deposited through aeolian processes from the environment surrounding the Castle first, followed by formation of the Ca-rich birnessite layer. The most recent stage in deposition on the surface of the Castle is a thin silica glaze.

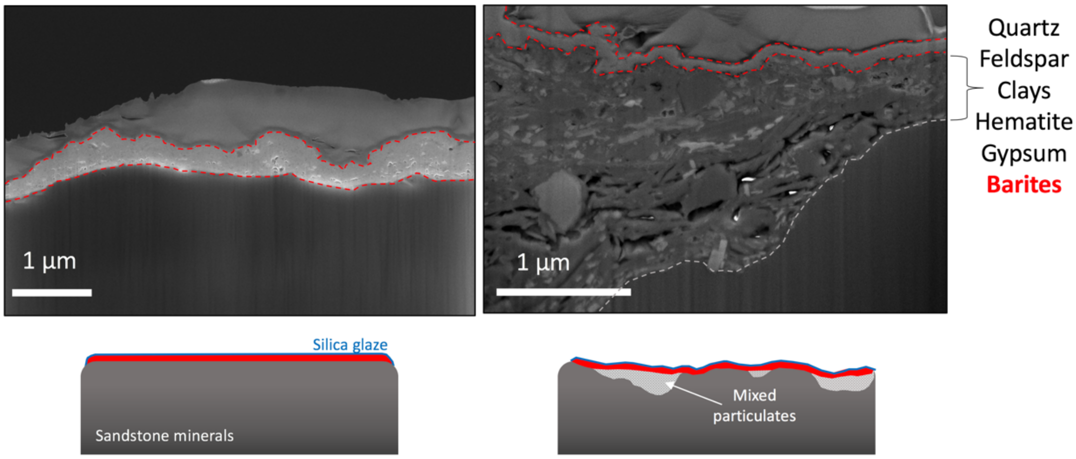

Figure 6.6. SEM images of the two types of layers seen in the FIB sections. On the left, a relatively thick (~900 nm) film sits on top of an SiO_2 grain. On the right, a thinner layer of the Mn-rich film sits on top of particulates that contain quartz, feldspar, clays, hematite, gypsum, and barites. Below each SEM is a cartoon demonstrating the relative nanostratigraphy.

Reclassifying the Varnish as a Manganese Skin

The incredible enhancement of Mn in this discolored surface layer of the Castle (>100x over the underlying Seneca sandstone) and the intensity of Mn over clay minerals indicates a departure from traditional rock varnish. The overwhelming dominance of Mn suggests the formation of a manganese skin, as opposed to rock varnish which by definition is dominant in clays.[40] Manganese skins are the most common type of heavy metal skins, which are rock coatings composed primarily of heavy metals derived from either natural or anthropogenic sources. Despite the difference in classification based on major elemental component, manganese skins and rock varnishes have many commonalities, including in mineralogy and the ability to scavenge other heavy metals, in morphology, and in origin of formation. Compared to rock varnishes, manganese skins are found more often in wetter climates and locations, such as caves, streams, beaches, springs, and glaciers.[40] This has led researchers to hypothesize that manganese skins have a primarily biological origin because these wetter areas are usually in neutral to acidic pH environments and therefore unlikely to undergo physicochemical oxidation. However, abiotic methods of formation have not been disproven, and are thought to be the dominant formation pathway only in certain environments, such as at junctions where sea water and freshwater mix, or ground water mixing with stream water.

It is difficult to determine the growth rate of the Mn-rich film on the Seneca sandstone due to vast differences in thickness and an unknown timeline of when formation began. As reported here and in Macholdt et al., the growth on the west façade of the Castle is ranges from ~150 nm to 4 µm.[23] The presence of barites suggests that the Mn film is younger than the age of the Castle. Additionally, this layer is present on the Enid A. Haupt Garden Gateposts, which were erected just over 30 years ago.[21] If the Mn-rich film is as young as ~30-50 years, then the growth rate is at the high end or much faster than the reported 1-40 µm/millenia. This is consistent with reports of varnish that accumulates in wetter environments and of manganese skins. Manganese skins can form in as little as 25 years, and within a single year in certain environments.[40] If the Mn film is as old as the Castle itself, then the growth rate falls to the low range of the accepted literature range.

Evidence based on relative timeline and composition of the Mn-rich film on the Castle suggests that formation is unlikely completely abiotic in origin. The Washington, D. C. area is considered a humid, sub-tropical zone. The average rain pH is between 4.2-4.4, more acidic than rain in unpolluted environments.[41] In these conditions, it is unlikely that physicochemical oxidation of Mn^{2+} is the main mechanism of Mn oxide formation, unless autooxidation is occuring.[32] The purity of the birnessite phase of the oxide and the enhancement of Mn are also unlikely to occur from physicochemical processes alone. However, there is still no clear evidence for biological activation of the material. Unlike other reports, we did not find casings of bacteria or bacterial remains in the SEM/FIB cross-sections taken that point towards Mn oxide producing bacteria.[42,18] We did observe bacterial remains, in the form of filaments, but these were few and far between on the surface of the Mn-rich layer and were not encrusted in Mn. The filaments are similar to the bacteria seen on the Enid A. Haupt Garden gateposts,[21] which also appear to have occurred after the formation of the Mn-rich layer, rather than attributing to it. It is difficult to pinpoint what organisms are responsible for Mn enhancement without direct evidence for biological production of birnessite, which cannot be observed without controlled laboratory experimentation. It is interesting to note that similar dark bluish-black surface coatings have been forming on other buildings specifically composed of Seneca sandstone throughout D.C. and the surrounding region. While dark surface coatings also plague other pieces of architectural stone in the area, not all are due to Mn accumulation and can instead be attributed to gypsum deposits or biofilms.[41,43] The preference for varnish or heavy metal skins formation on the Seneca sandstone alone may be another hint at its origin.

For the Smithsonian, a biotic hypothesis of origin means that remediation may not inhibit continued growth of Mn oxide at the surface of the Castle. Laser pulse cleaning has been used successfully to remove some discolored areas of the Mn rich layer, but if the Mn enhancement is due to bacteria or fungi that continue to thrive on the stone surface, it is unlikely that Mn oxide accumulation will stop.

Conclusion

We have investigated the Mn-rich varnish accumulating on the Smithsonian Castle using a combination of nanoscale analysis with electron microscopy and x-ray spectroscopy, specifically utilizing SEM/FIB for subsequent TEM analysis. The primary mineralogical phase of the varnish is Ca-rich birnessite, a layered phyllomanganate. The Mn-rich film observed in cross sections of the Castle is less than 1 μm in thickness in the areas studied and contain only trace quantities of Fe, Si, and Al. The richness of Mn, over 100x enhancement relative to the underlying Seneca sandstone, and relative scarcity of Si and Al within the same layer indicates that the varnish should be classified as a heavy metal skin. Evidence of nanoscale $BaSO_4$ particulates, both in the Mn-rich film and within particulate matter underneath the film, are indicative of deposition from an atmospheric source because Ba is not found in the underlying Seneca sandstone. Therefore, the presence of $BaSO_4$ in particulate matter underneath the Mn film reveals a relative timeline of film growth, indicating that the film is likely younger than the age of the Castle. The purity of the birnessite phase, the richness of Mn with few other silicates and clays, and the wet climate in which the film is forming all suggest that an abiotic hypothesis of origin is unlikely; however, we did not find evidence that supports a biotic origin of formation.

Bridge to Chapter VII

Chapter VI used TEM on SEM/FIB-prepared samples to investigate a nanoscale metal oxide forming naturally on architectural stone. This chapter provided an example of the importance of understanding nanoscale structure in cultural heritage. Although the exact genesis of the manganese layer is still unknown, the nanoscale structural and compositional knowledge gained from this study better informed the identity of the layer and points towards a hypothesis of formation. Chapter VII concludes this dissertation by wrapping together the key ideas that this work poses towards using nanotechnology to both advance the future and understand the past.

CHAPTER VII

CONCLUSION

Concluding Remarks

Nanotechnology has the potential to provide solutions to global problems thanks to the unique properties that nanomaterials exhibit. Curiosity has long driven our discovery of these properties and our creativity in how to utilize them. While the history of man-made nanotechnology implies that nanotechnology is ancient, the ways in which we now synthesize nanomaterials deliberately, rather than empirically, makes it modern. Some discoveries will certainly continue to be serendipitous, but the more knowledge about structure-guided properties that we have, the more that nanomaterials will continue to be designed to address specific needs and applications.

This dissertation examined the formation process of metal oxide nanomaterials made through direct-write electron beam processes and natural processes, highlighting the importance of modern characterization techniques in both fabrication and analysis. For direct-write processes, the ability to control structure through synthesis opens the door to investigating new structure driven properties, such as the synergistic properties exhibited by nanocomposites. Knowledge of the chemistry behind the transformation is key to designing structure and therefore controlling properties. As analysis and fabrication techniques continue to develop, they will aid the purposeful design of new nanomaterials. However, inspiration for future nanotechnology is also gained from looking to our past and observing materials in nature. Nanomaterials made by ancient civilizations as well as those made by nature have only been discovered because of the characterization techniques we now have that allow us to see them. These studies not only give us a glimpse into the world around us but also inspire creative design of materials that can be harnessed for new technology. As methods of characterization improve, more information about the synthetic history of our world will surely be revealed, changing our understanding of both the current world we live in and the future one we imagine.

APPENDIX A

SUPPORTING INFORMATION FOR CHAPTER II: SUB-30 KEV PATTERNING OF HAFSOX RESIST: EFFECTS OF VOLTAGE ON RESOLUTION, CONTRAST, AND SENSITIVITY

Three distinct artifacts were observed when patterning. The first is a small dot in the upper right hand corner of the desired pattern. This is believed to be the resting position of the beam due to the spherical nature of the artifact. The second artifact is a bar along the top of the field of view and is proportional to the horizontal field width. The third artifact is a box that appears anywhere in the field of view and is also proportional in size to the horizontal field width. All three of these artifacts are seen when the stage is moved to a new location and patterning is performed without any prior unblanking of the electron beam. This is most likely due to a lack of a fast beam blanker, but can be overcome by making the horizontal field width large and diluting the unintentional dose to less than the energy required for condensation within the film. To reduce the impacts from these artifacts, the horizontal field width was expanded to 61 μm, and the pixel size was set to 10 nm at a field resolution of 6k. This removed all defects except the dot, which is related to the parking position of the beam during patterning. These strategies were only successful for high-resolution patterns that used 10 keV or higher; otherwise the film was so sensitive that the artifacts persisted. Patterning high-resolution features under 10 keV was not possible due to the large horizontal field width required to no longer see the artifacts.

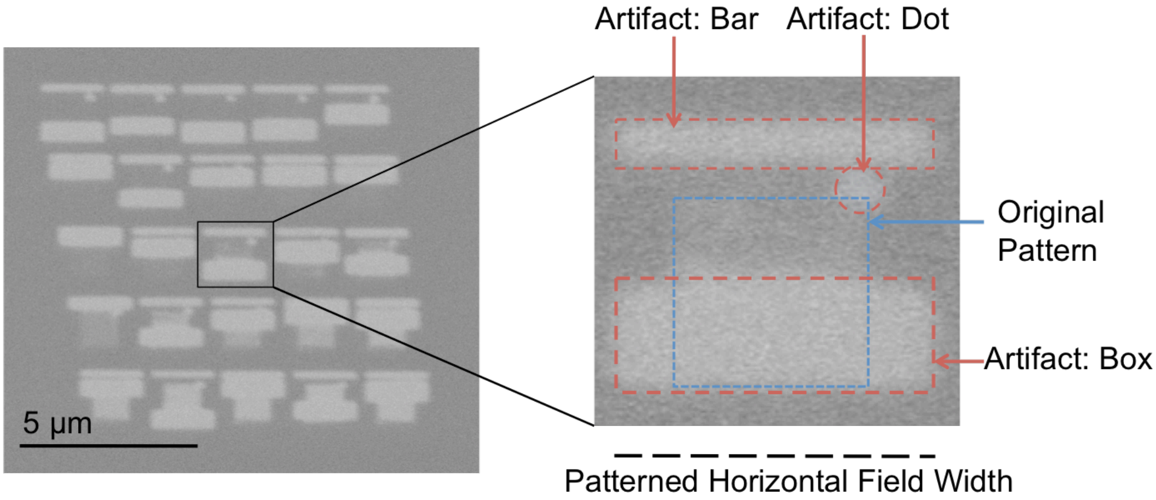

Figure A1. Artifacts from electron beam lithography.

APPENDIX B

SUPPORTING INFORMATION FOR CHAPTER III: IMPLICATIONS OF CRYSTAL STRUCTURE ON ORGANOTIN CARBOXYLATE PHOTORESISTS

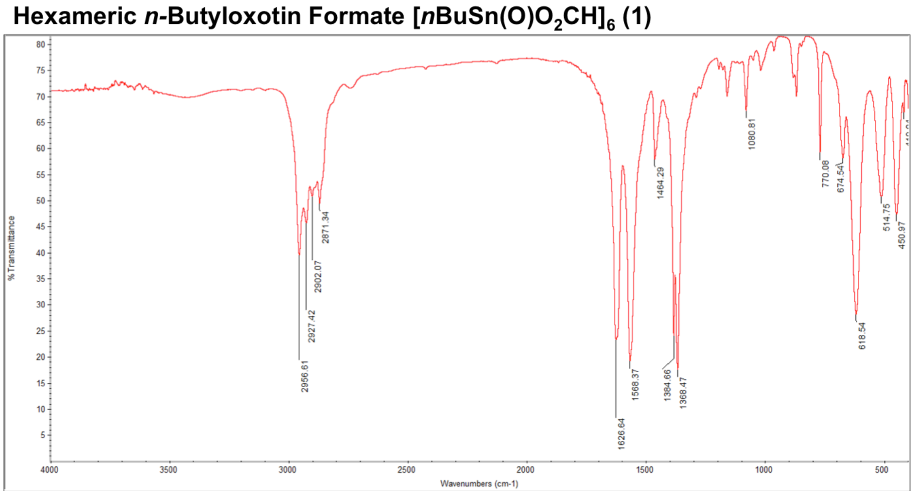
Hexameric *n*-Butyloxotin Formate [nBuSn(O)O$_2$CH]$_6$ (1)

Figure B1: IR (KBr) spectrum for 1.

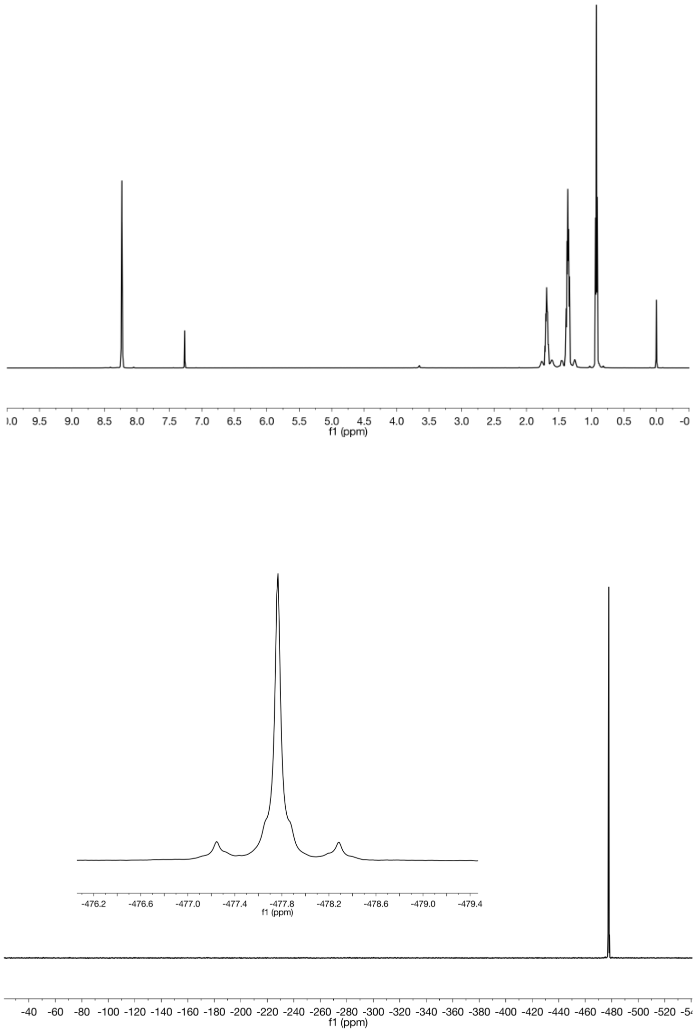

Figure B2: Top, proton NMR for 1 referenced to TMS. Bottom, ^{119}Sn {^{1}H} NMR for 1. Insert shows peak splitting.

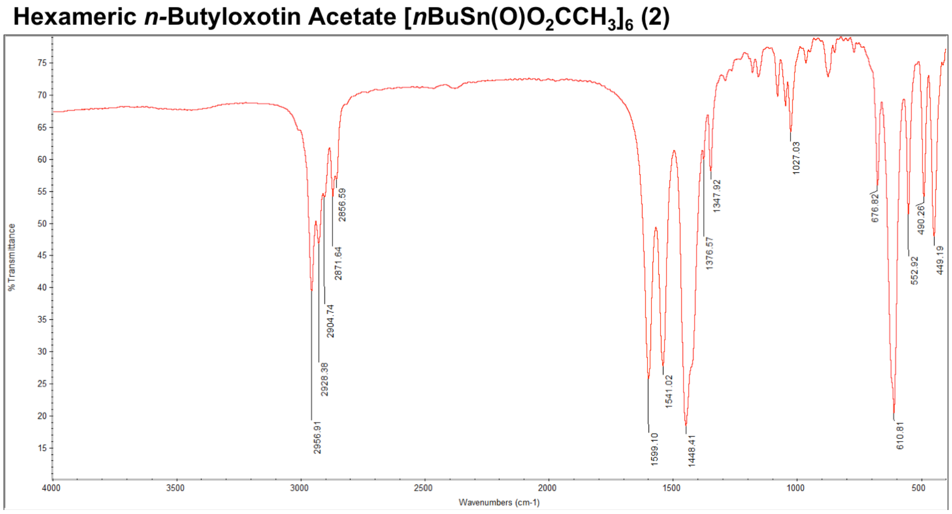

Figure B3: IR (KBr) spectrum for 2.

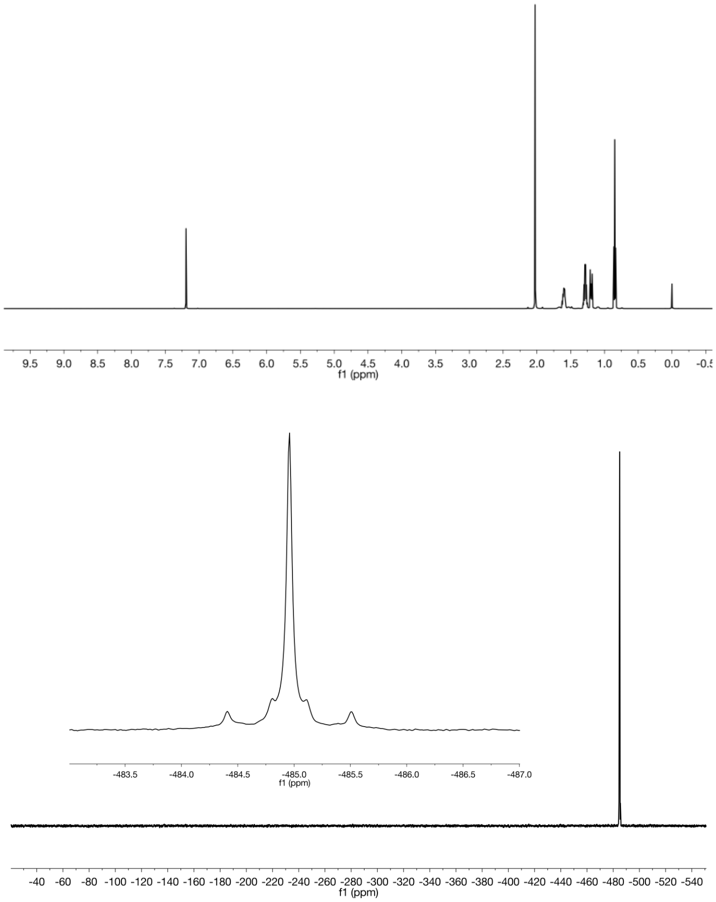

Figure B4: Top, proton NMR for 2 referenced to TMS. Bottom, ^{119}Sn $\{^1H\}$ NMR for 2. Insert shows peak splitting.

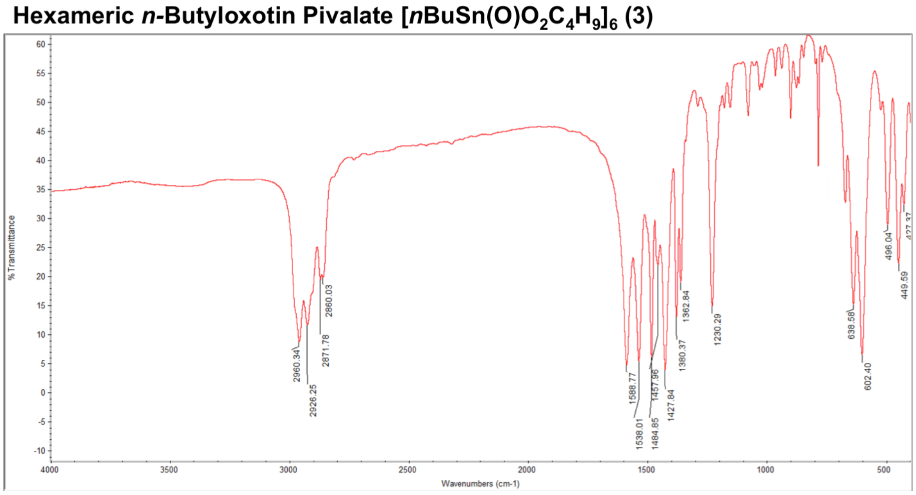

Figure B5: IR (KBr) spectrum for 3.

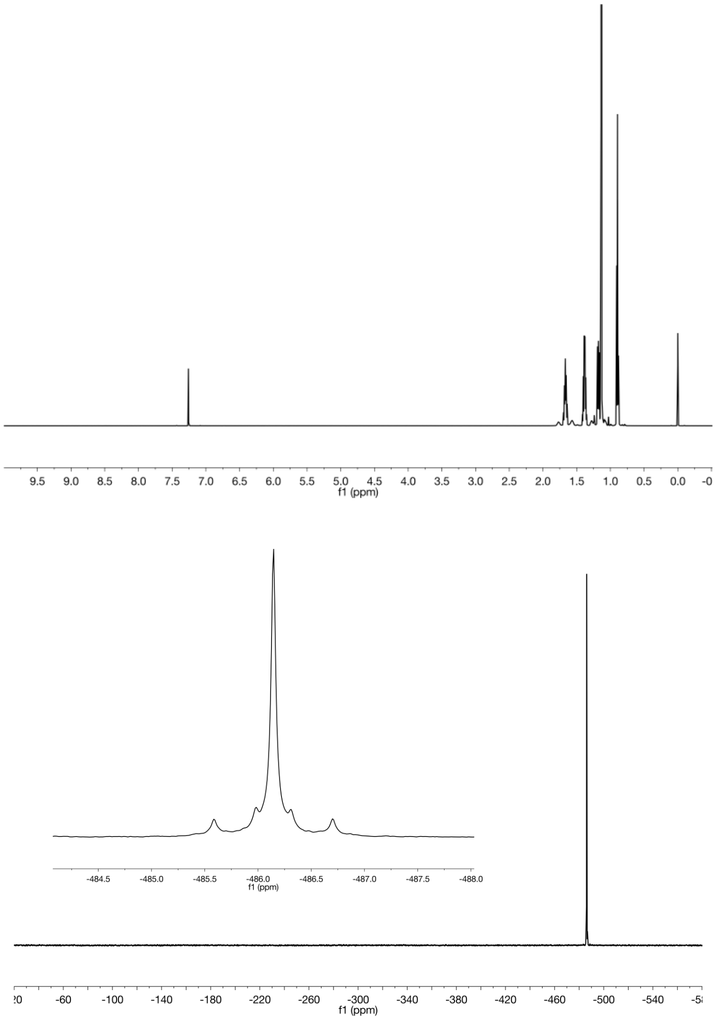

Figure B6: Top, proton NMR for 3 referenced to TMS. Bottom, ^{119}Sn {^{1}H} NMR for 3. Insert shows peak splitting.

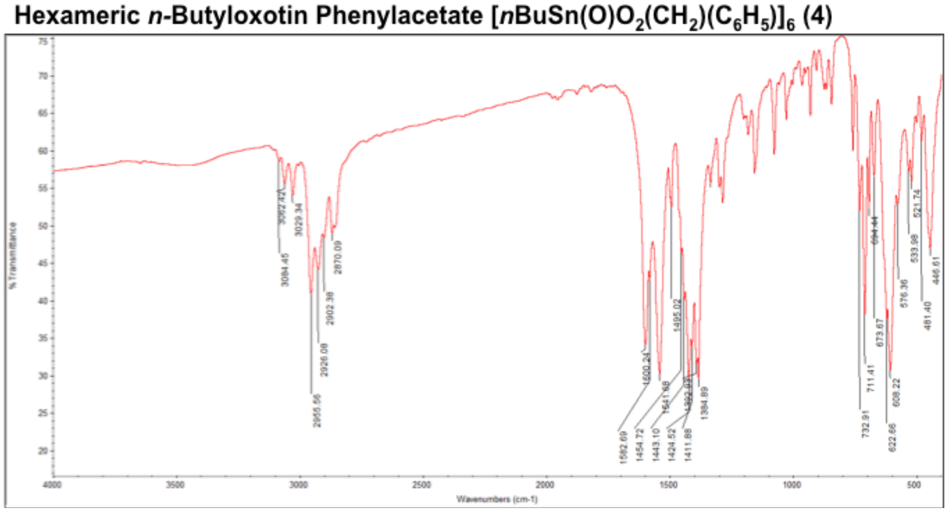

Figure B7: IR (KBr) spectrum for 4.

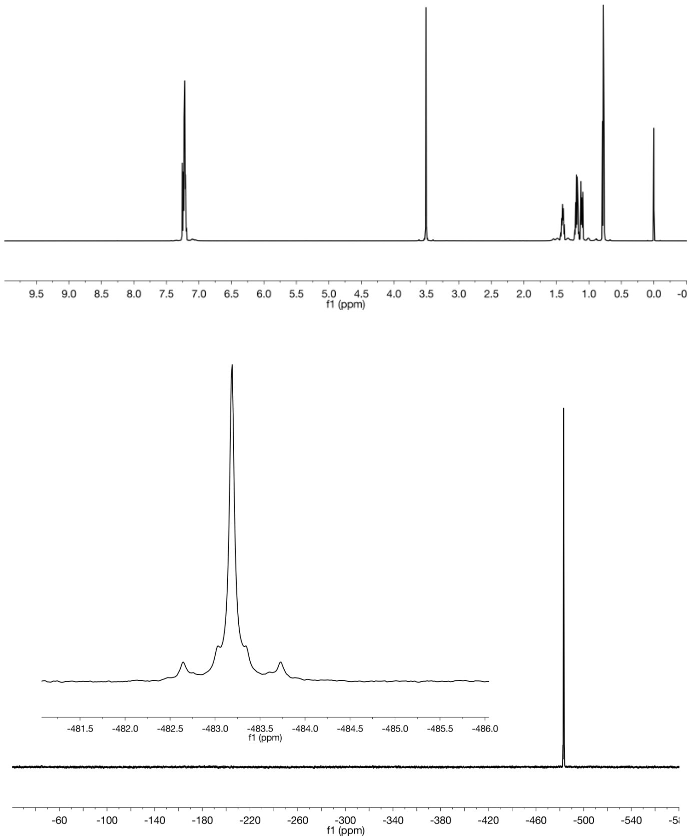

Figure B8: Top, proton NMR for 4 referenced to TMS. Bottom, ^{119}Sn {^{1}H} NMR for 4. Insert shows peak splitting.

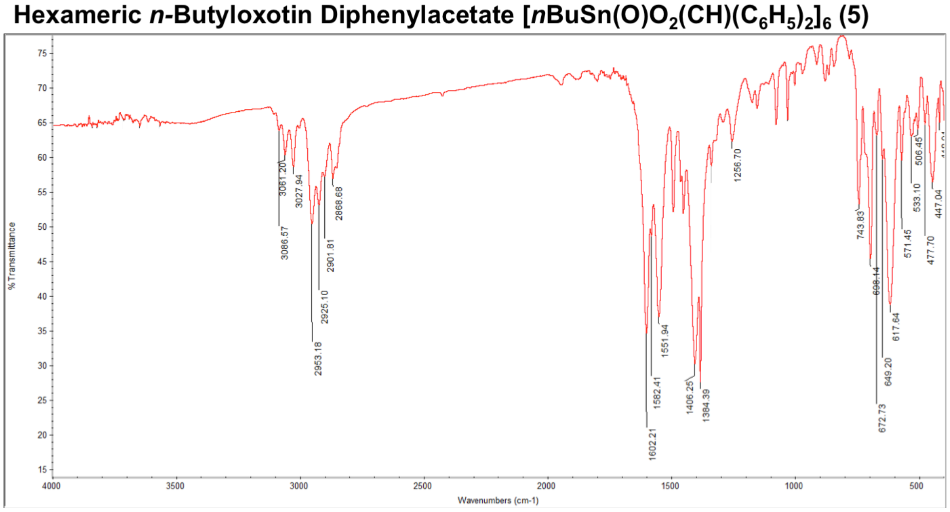

Figure B9: IR (KBr) spectrum for 5.

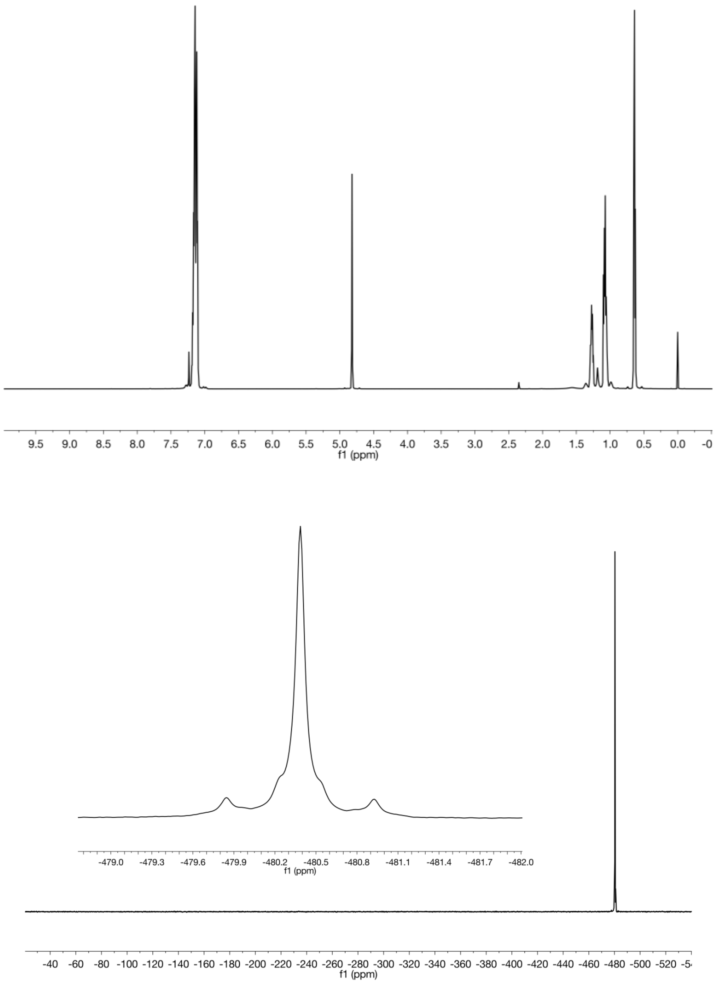

Figure B10: Top, proton NMR for 5 referenced to TMS. Bottom, ^{119}Sn {^{1}H} NMR for 5. Insert shows peak splitting.

APPENDIX C

SUPPORTING INFORMATION FOR CHAPTER IV: ORGANOTIN CARBOXYLATE REAGENTS FOR NANOPATTERNING: CHEMICAL TRANSFORMATIONS DURING DIRECT-WRITE ELECTRON BEAM PROCESSES

NMR and IR for Football Cluster

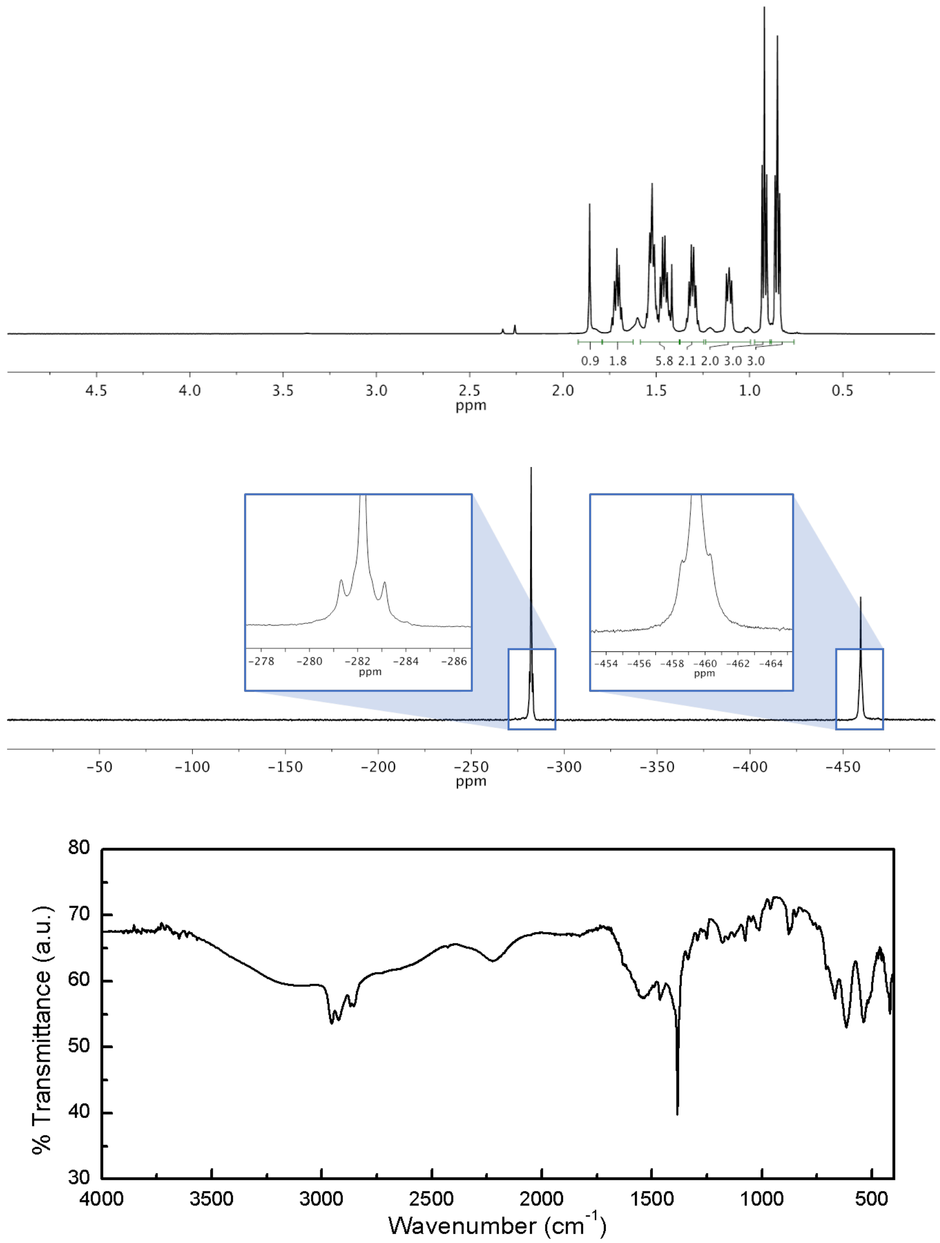

Figure C1. Top) ^{1}H NMR for the football cluster. Middle) ^{119}Sn NMR for the football cluster, with each peak magnified to display splitting. The two different tin peaks reflect the 5-coordinate and 6-coordinate environments for the football cluster. Each peak integrates to 1. Bottom) Transmission IR (KBr) for the football cluster.

NMR and IR of Drum Cluster

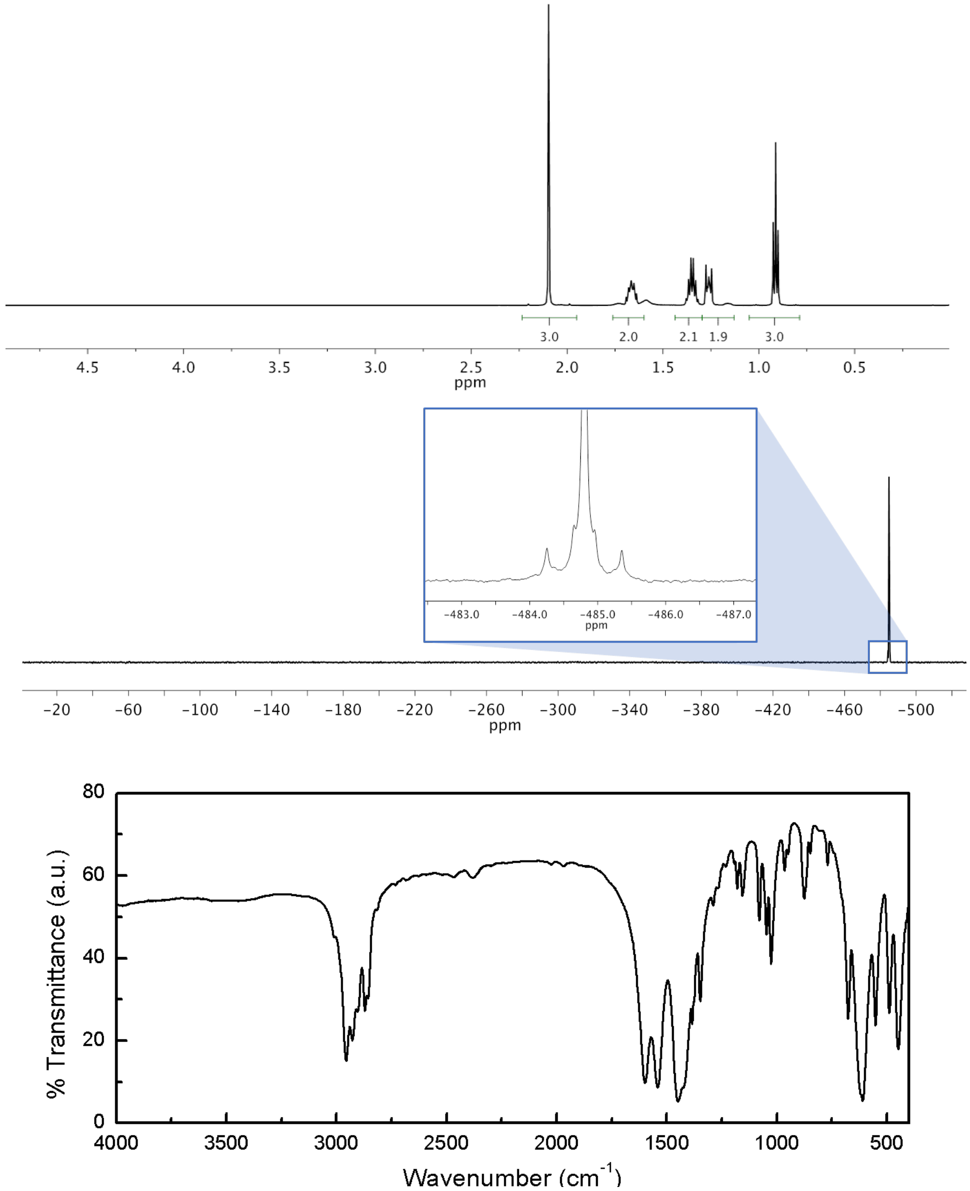

Figure C2. Top) ^{1}H NMR for the drum cluster. Middle) ^{119}Sn NMR for the drum cluster, with the peak magnified to display splitting. Bottom) Transmission IR (KBr) for the drum cluster.

NMR and IR for Dibutyltin Diacetate

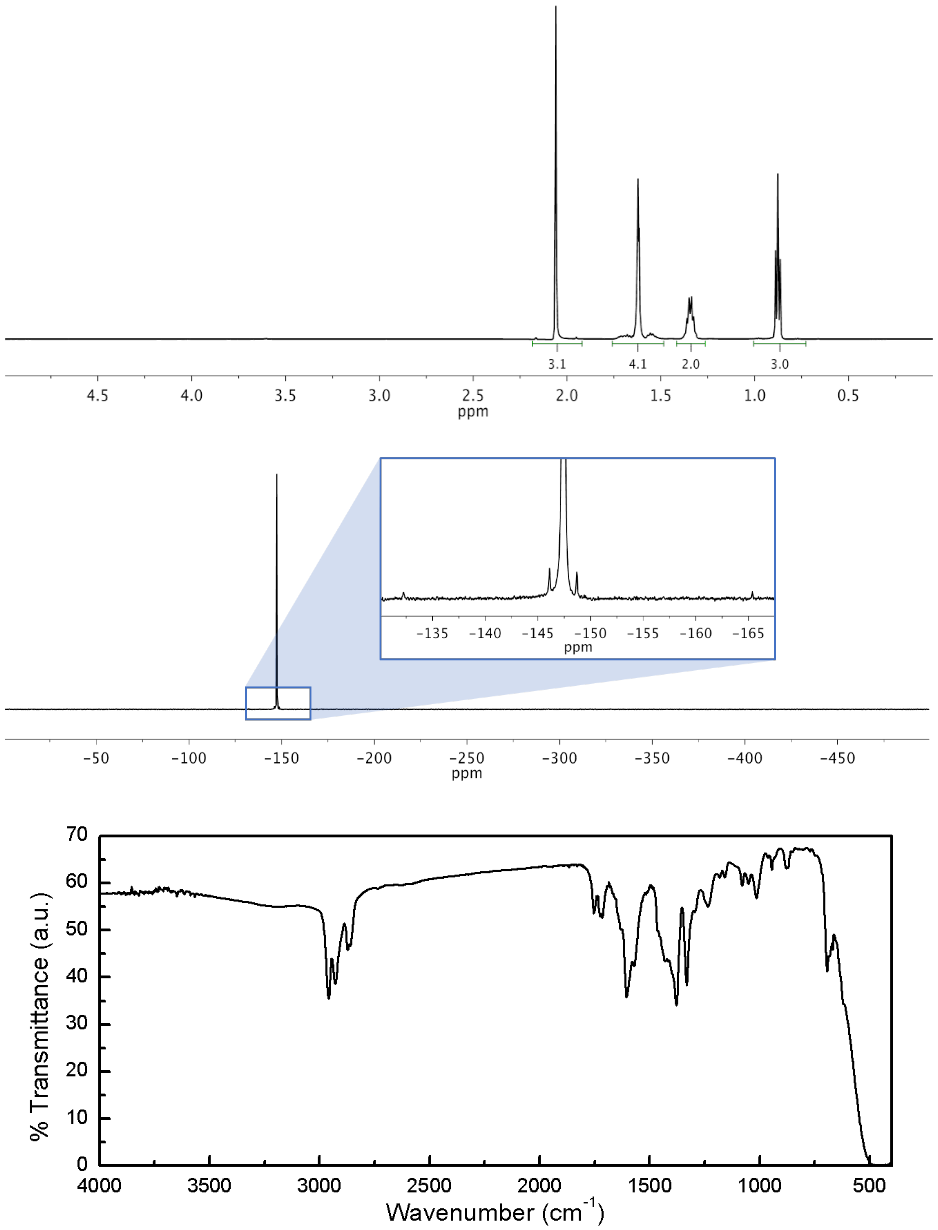

Figure C3. Top) ^{1}H NMR for the monomer, dibutyltindiacetate. Middle) ^{119}Sn NMR for the monomer, with the peak magnified to display splitting. Bottom) Transmission IR (neat) for the monomer.

AFM Dose Array Step Height Measurement Procedure

The step heights of each box in the dose array relative to the silicon substrate surface was measured with AFM by taking an image at the edge of each box in the dose arrays. To obtain data for the sensitivity curves, the resulting images were analyzed using Nanoscope Analysis, version 1.8. Each image was first plane-fit to the flat area of the silicon substrate. The slice tool was then used to measure six or more random places across the image. These values were then averaged and the standard deviations in step height are reported as variation in thickness.

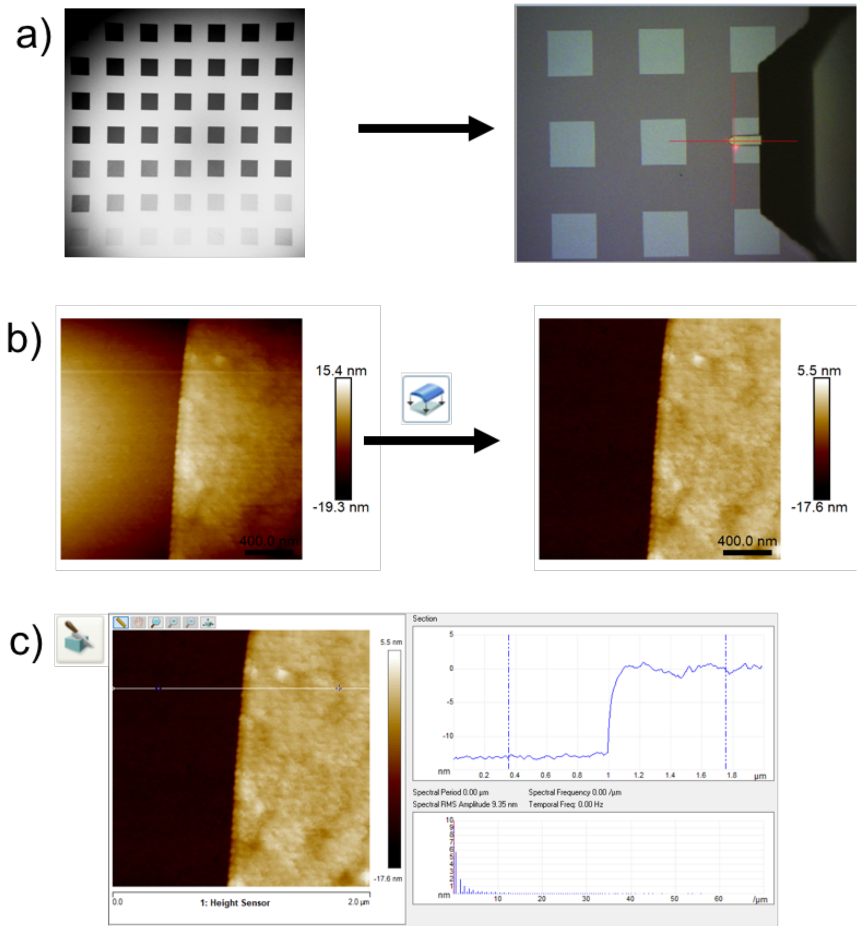

Spectral Period 0.00 µm
Spectral Frequency 0.00 /µm
Spectral RMS Amplitude 9.35 nm
Temporal Freq: 0.00 Hz

Figure C4. a) SEM image of the dose arrays, followed by an image of the AFM tip at the edge of one of the patterned boxes. b) AFM images of the edge of a box before and after the plane fit. The plane was fit to the left area of the image under the assumption that the silicon substrate is flat. c) Example of a slice taken across the plane fit image.

TGA for Football and Drum clusters

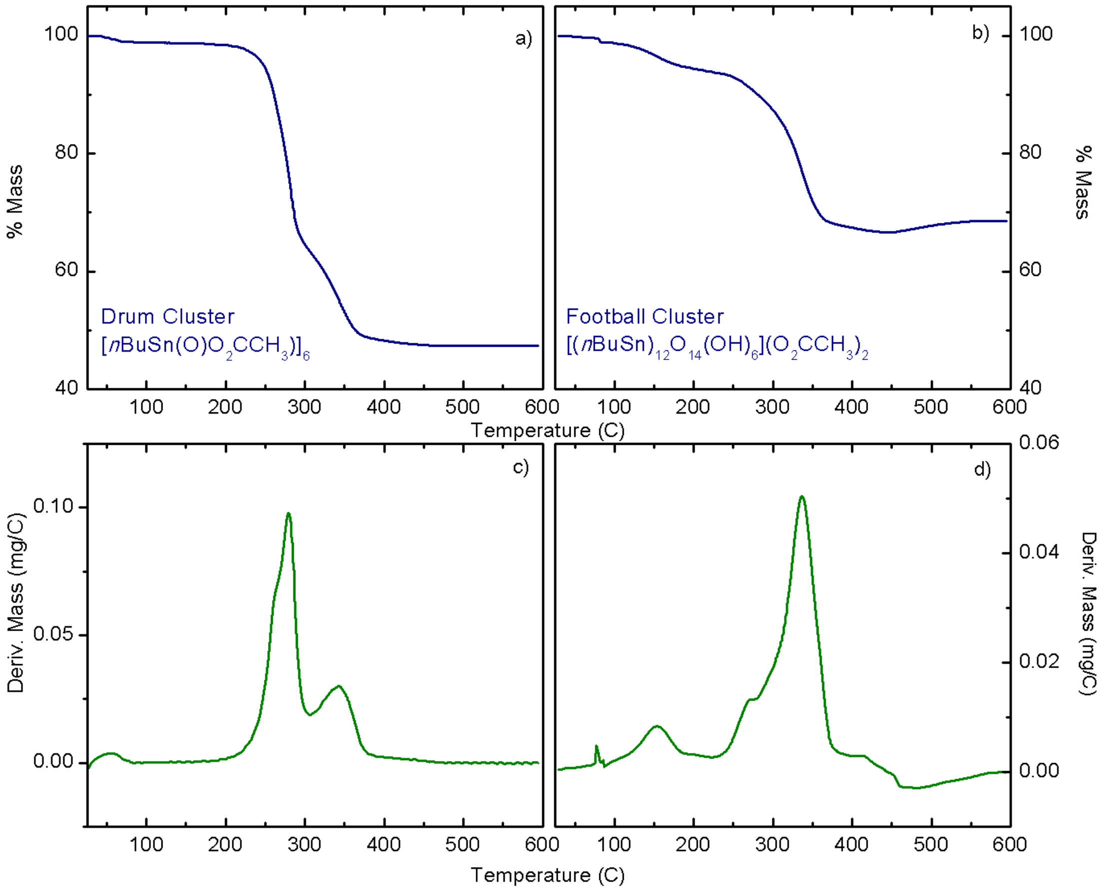

Figure C5. a,b) TGA traces for the drum and football cluster species, with corresponding derivatives of the mass loss traces below (c,d). Each trace was taken under N_2 and both clusters conclude the majority of their mass loss by 400 °C. The football cluster undergoes a first, small loss around 150 °C which corresponds by mass to the coordinating acetate groups. The second, larger loss around 320 °C corresponds by mass to the butyl groups. The peaks in c) for the drum cluster overlap and cannot easily be attributed to one ligand or the other, but it is important to note that mass loss does not occur until ~250 °C. The acetate groups of the football cluster decompose more quickly than those in the drum cluster. We were unable to measure the thermal decomposition of the monomer species because its boiling point is below its decomposition temperature.

XPS values: Relative rates of C decrease as a function of dose

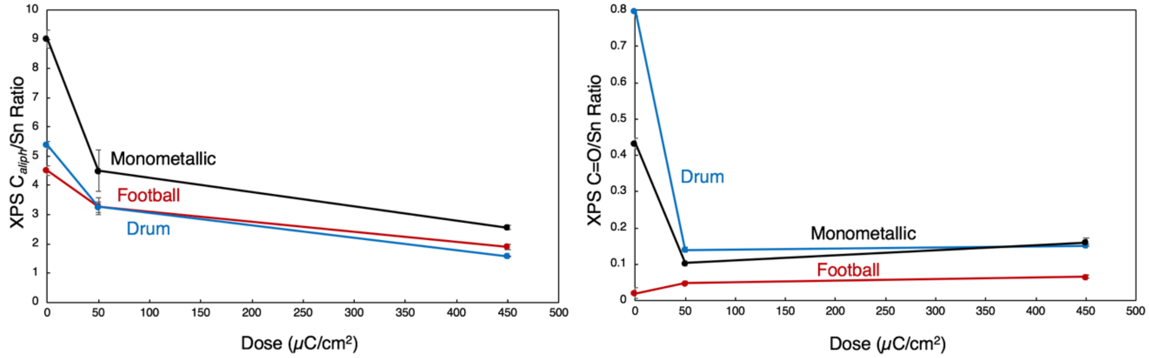

Figure C6. Left) XPS C_{aliph}/Sn ratio as a function of dose, showing an initial large decrease from the non-patterned film to the 50μC/cm^2 film, followed by a slower rate of decrease to the 450 μC/cm^2 dose. Right) XPS C=O/Sn ratios as a function of dose, showing an initial decrease for the monometallic species and the drum followed by a slight increase. The ratios increase slightly for the football cluster.

XPS Control Studies to Understand SEM Carbon Deposition

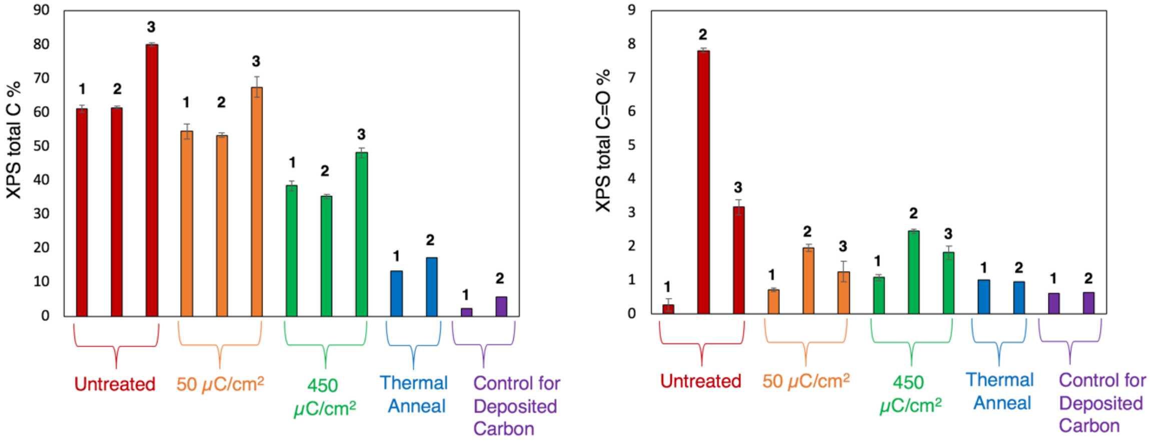

Figure C7. Left) Bar graph showing total atomic percentages for carbon in all three species. Red are untreated films, orange are films treated at 50 μC/cm^2, green are films treated at 450 μC/cm^2, blue are thermally annealed films, and purple are the percentage found from controls for deposited carbon. Each species is individually labeled with its corresponding number above each bar. The amounts of deposited carbon found are not large enough to significantly influence the values of the patterned films. Right) The same graph showing total atomic percentage of C=O found in the films. While the amount of C=O found in the control films is small, it is still within a percentage of the values found in many of the other films and is significant enough to influence the data of the patterned films.

Thermally Annealed Cluster Films

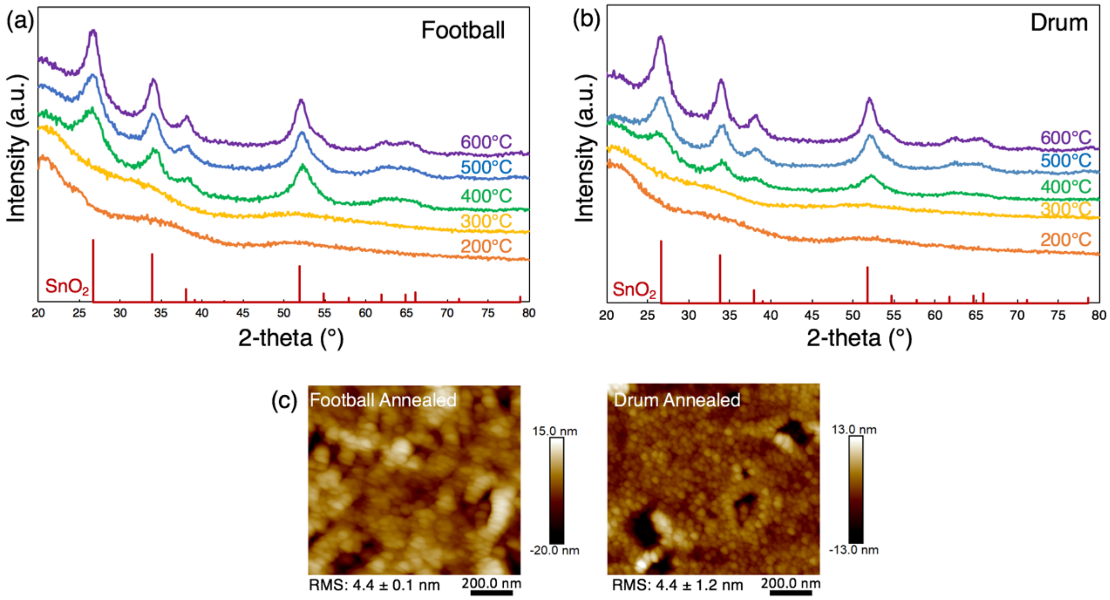

Figure C8. (a) Grazing incidence x-ray diffraction data of a series of thermally annealed films of the cluster **1** in air. The film is amorphous through 300 °C and starts showing characteristic peaks associated with the crystal structure of SnO_2 by 400 °C. A reference to SnO_2 is shown in red. (b) GIXRD data for a series of thermally annealed films of cluster **2**. This film shows similarities to the larger cluster in that it becomes crystalline at 400 °C. (c) AFM images showing the surface morphology of the thermally annealed films at 600 °C. The RMS roughness values are much higher than patterned films and it is clear that the morphology has changed.

TEM Induced Crystallization of Patterned Films

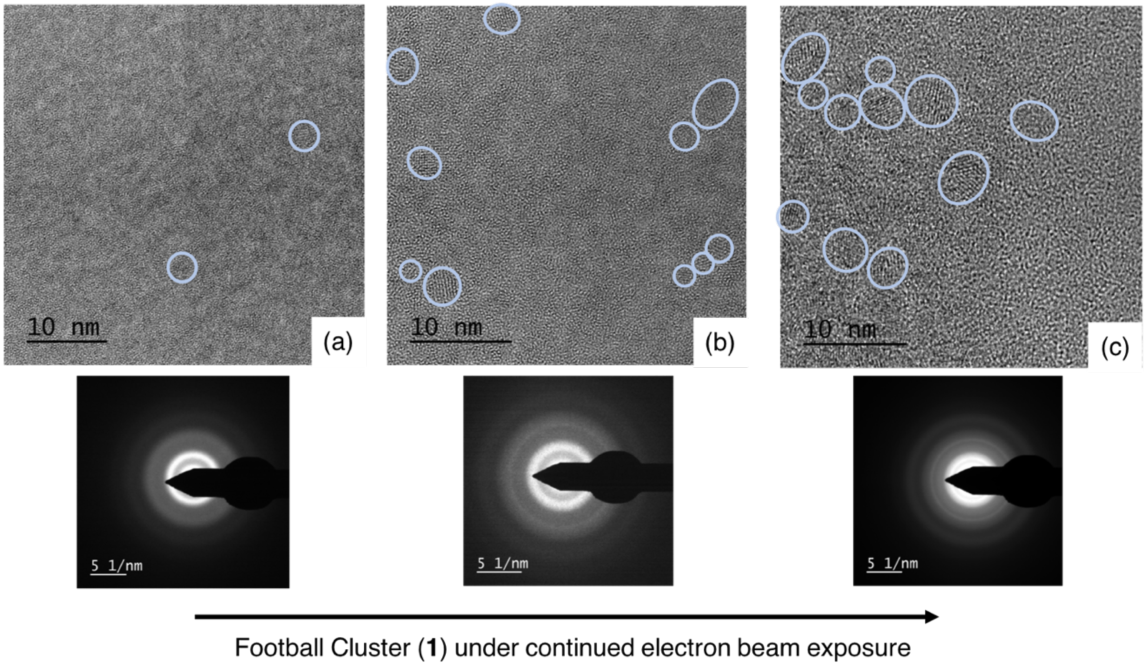

Figure C9. High-resolution TEM images and selected area diffraction patterns of films of the football cluster at three different beam exposures. Circled blue areas show crystallization of the material. In a) the image was taken quickly after moving to a fresh area of the film. b) shows more small crystals forming as the electron beam sits on an area and c) shows both more and larger crystallites after minutes of exposure. The rings in the diffraction patterns become more defined over time, confirming continued formation of crystallites as a function of exposure to the high voltage electron beam.

Electron Stimulated Desorption (ESD) Snapshot Spectra of Football, Drum, and Monomer Films

On exposure to E_{kin} = 2000 eV electrons, each film type demonstrated an immediate response in the mass spectrometer. The survey spectra were consistent with the desorption of butyl ligands observed previously,[1] as well as with minor desorption of the acetate groups and the solvent. Due to the length required for each cycle of the survey spectra (10s of seconds) versus the fast desorption kinetics, more detailed survey snapshots were collected for the first full cycle after opening the shutter to the electron gun. Shown below in Figure C10 are (a) the full survey for baseline masses in the Hiden ESD system prior to electron exposure, and the first full cycle after electron exposure of (b) football, (c) drum, and (d) monomer films. The main species observed from the films include m/z = 12, 15, 16, 18, 28, 41, 43, 44, 45, 56, 58, 59, 60, 71, 85, and 114.

The baseline signal in the ESD system primarily shows water (m/z 18), attributed to water adsorbed to the analysis chamber, as well as low-level carbon monoxide and carbon dioxide indicated by m/z 28 and 44, respectively. The intensity of the baseline species in the mass spec is less than the intensity of species observed during electron exposure. Intense signals attributed to butyl ligand loss, m/z 56, 41, 43, are observed in all film types on exposure to electrons. M/Z 28, 44 are also mainly attributed to butyl fragmentation (though could also be the result of oxygenate species CO, $CO_{2,}$ respectively). There is an increase in water, m/z 18, that is significantly above the baseline in the monomer film. The monomer is more moisture sensitive than the cluster species, so an increase in the water signal for this film could be due to increased water content that is then reflected in the desorption data. There is also minor desorption of m/z 71 and 85, likely due to the loss of some incorporated toluene from the spincoating solvent.

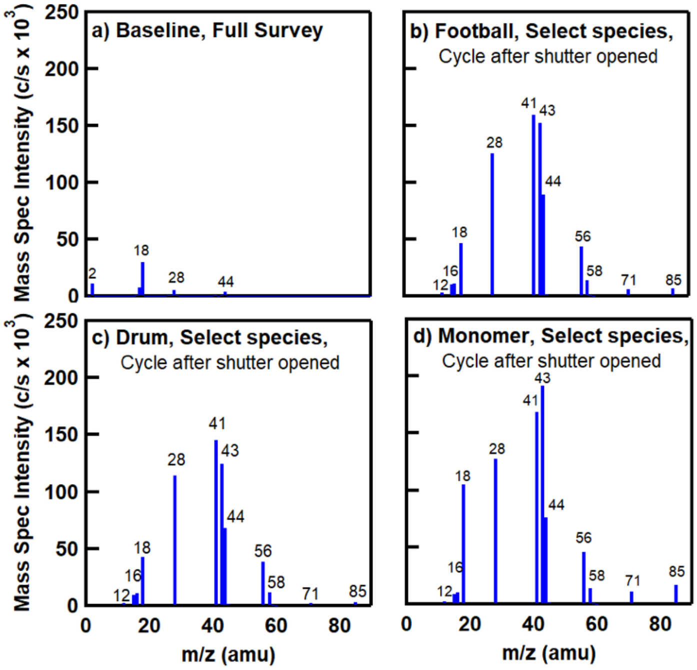

Figure C10. Spectra for (a) the full survey of the Hiden ESD system's baseline and select-mass spectra for the first full cycle after opening the 2000 eV electron gun onto samples of (b) the football film, (c) the drum film, and (d) the monomer film.

ESD cross section analysis

The kinetics of desorption from the thin film resist were determined using a method described previously.[2] Briefly, we take Equation 1, which describes the change in coverage of the radiation sensitive species, σ, over time, t, due to electron beam exposure with current, J, and electron charge, ε, as it relates to the total desorption cross section of the system, Q.[3,4] This is rearranged, as has been done previously for mass spectrometer desorption quantification,[3,4] to arrive at Equation 2. As the current density of our electron beam was non-constant, a MATLAB program was used to create ln(i) vs. t ESD profiles for the electron beam profile array, J, that was measured immediately before each experiment. The value of Q was varied until the ln(i) vs. t for a given Q matched to the experimental data. We anticipate a larger number of daughter electrons to be generated from the initial 2000 eV electrons, and so the value of these cross sections represent the total effective desorption from our initial impinging beam through the film, inflated by many cascade events.

$$-\frac{d\sigma}{dt} = \frac{\sigma Q J}{\epsilon} t \qquad (1)$$

$$\log\left(\frac{i(t)}{i_0}\right) = -\frac{QJ}{\epsilon} t \qquad (2)$$

ESD/Temperature Programmed Desorption (TPD) Analysis of football cluster organic groups

Samples were run with TPD, either for an as deposited sample, or were first subjected to the electron beam within the instrument to a specified dose to induce an electron induced chemical reaction before subsequently undergoing TPD to determine what still desorbs after the electron induced desorption / film reactions. For the as-deposited film, Figure C11a, the most prominent peaks are from m/z ratios associated with fragments cleaved from the butyl groups during thermal treatment. For TPD done on the football cluster film after 10 μC/cm^2 of exposure with E_{kin} = 2000 eV electrons, there is a reduction in the signal of these butyl fragments. Normalized by film volume, 64% ± 5% of organic components are left over after dosing to 10 μC/cm^2. These peaks are representative of desorption from organic content that remains in the film after patterning. The signal of the alkyl fragments is also reduced after the film is irradiated to 450 μC/cm^2. Normalized by film volume, 52% ± 7% of the organic components are left over after dosing to 450 μC/cm^2. There is a much greater reduction in the signal between unexposed and 10 μC/cm^2 compared with the move from 10 μC/cm^2 to 450 μC/cm^2. This suggests that irradiating these films with a much greater dose does not necessarily drive a more complete reaction than at low doses, and organic content cannot be fully removed from electron patterning alone.

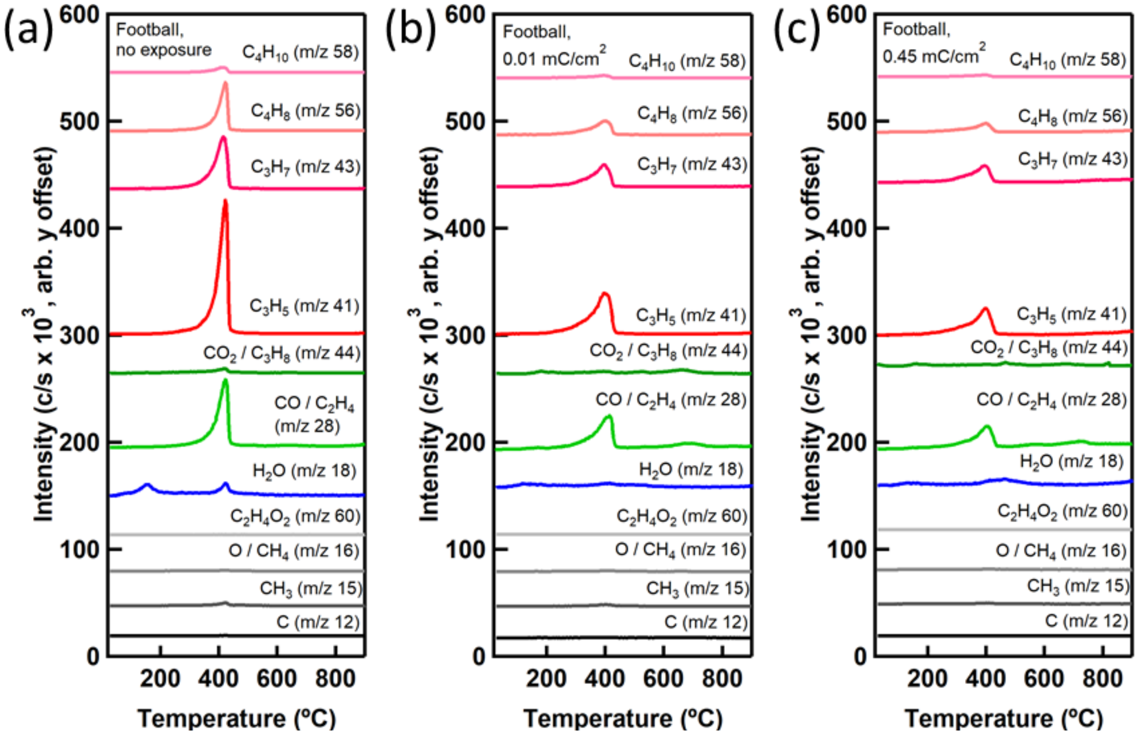

Figure C11. Temperature programmed desorption (ramp rate = 10 °C/min) profiles for a variety of masses expected to desorb from the football cluster on heating, including butyl and carboxylate fragments, as well as water. (a) On an as-deposited film of the football cluster. (b) After whole-film irradiation with 10 μC/cm^2 electrons, E_{kin} = 2000eV. (c) After whole-film irradiation with 450 μC/cm^2 electrons, E_{kin} = 2000eV.

Post-Treatment of Patterned Films

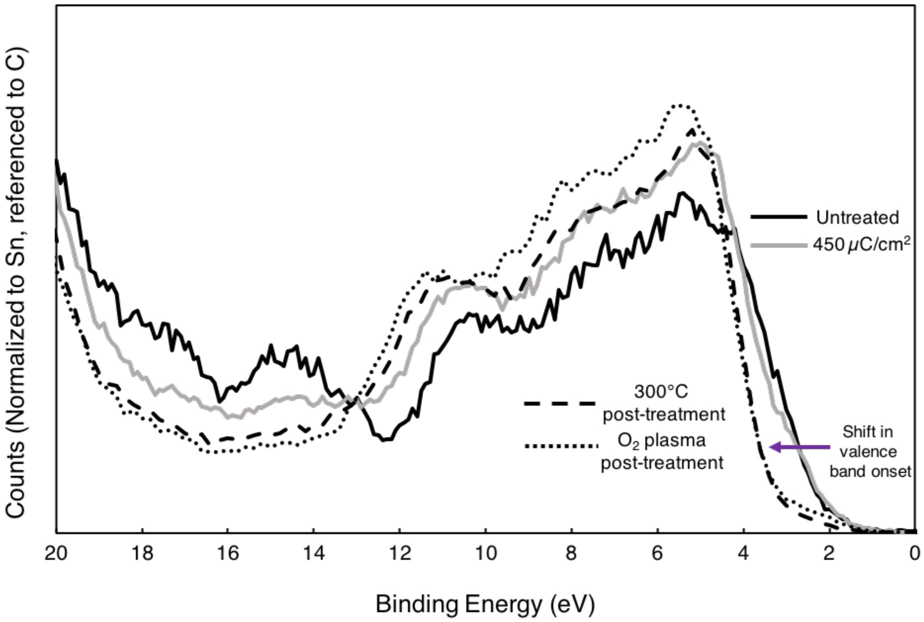

Film Type	*Atomic % C by XPS*
Untreated	61.1 ± 1.1
Patterned to 450 μC/cm^2	38.4 ± 1.4
Thermally Annealed	13.2
Patterned and Post-Treated by Annealing at 300°C	25.9
Patterned and Post-Treated with O_2 Plasma	13.6

Figure C12. Valence band XPS of the football cluster showing shifts in the VBM as the films are post-treated. Each spectra is referenced to carbon (284.8 eV). The graph shows that the film patterned at 450μC/cm^2 has a valence band onset similar to the untreated film. After the patterned film is treated either by heating on a hotplate at 300 °C for 10 minutes or exposed to O_2 plasma for 10 minutes, the VBM shifts closer to ~3.7 eV, the band gap of SnO_2. The table compares the atomic percentages of C found by XPS on an untreated film, a film patterned at 450 μC/cm^2, and a film driven to SnO_2 through thermal annealing compared to post-treated films. Both thermal treatment and O_2 plasma treatments of patterned films reduce the amount of carbon found in the films.

APPENDIX D

SUPPORTING INFORMATION FOR CHAPTER V: TOWARDS DIRECT PATTERNING OF FUNCTIONAL NANOMATERIALS AND NANOCOMPOSITES

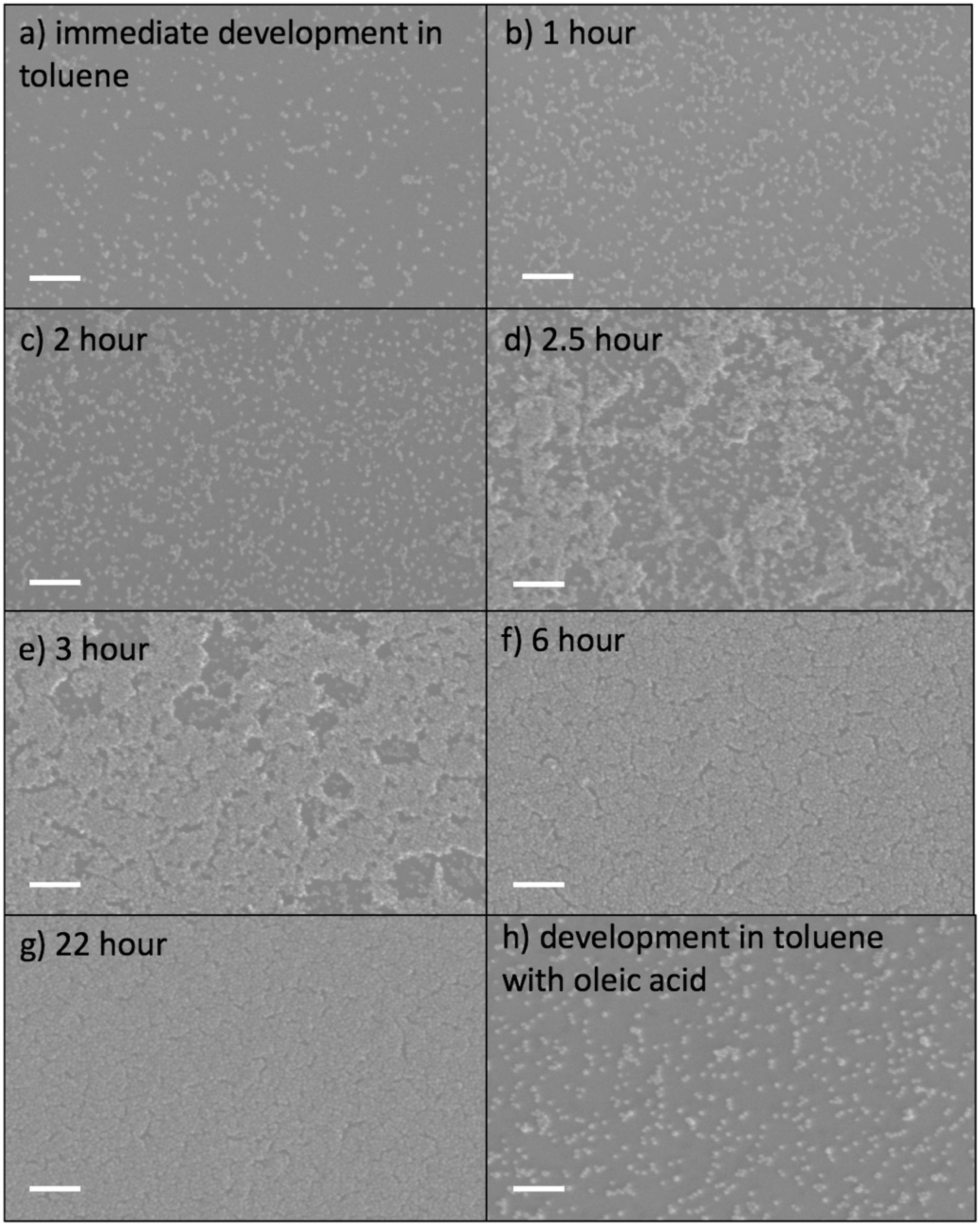

Figure D1. Development of a series of NC films spin-coated onto silicon over time. Seven films of NCs were spun onto silicon substrates and developed in warm (70 °C) toluene. Immediately after spin-coating (a) the NCs rinse off well. Films that were developed after a specified amount of time (b-g) exhibit greater adhesion of the NCs to the film, despite being developed in the same solvent. To mitigate adhesion, a drop or two of oleic acid can be added to the developing solution (h) and the NCs can be better rinsed off, regardless of time spent on the film before development. All scale bars are 100 nm.

REFERENCES CITED

Chapter I

(1) Fahlman, B. D. What Is “Materials Chemistry”? In *Materials Chemistry*; Springer Netherlands: Dordrecht, 2018; pp 1–21.

(2) Rai, R. S.; Subramanian, S. Role of Transmission Electron Microscopy in the Semiconductor Industry for Process Development and Failure Analysis. *Prog. Cryst. Growth Charact. Mater.* **2009**, *55* (3–4), 63–97.

(3) Schwab, K. The Fourth Industrial Revolution. *Encyclopædia Britannica*; Encyclopædia Britannica, Inc., 2018.

(4) Hodson, R. Digital Revolution. *Nature* **2018**, *563* (7733), S131.

(5) Brinkman, W. F.; Haggan, D. E.; Troutman, W. W. A History of the Invention of the Transistor and Where It Will Lead Us. *IEEE J. Solid-State Circuits* **1997**, *32* (12), 1858–1865.

(6) Sze, S. M.; Lee, M. K. *Semiconductor Devices, Physics and Technology*, 3rd ed.; Wiley: Hoboken, N.J, 2012.

(7) Moore, G. E. Cramming More Components onto Integrated Circuits. *Electronics* **1965**, *38* (8).

(8) Waldrop, M. M. The Chips Are down for Moore’s Law. *Nature* **2016**, *530* (7589), 144–147.

(9) Feynman, R. P. There's Plenty of Room at the Bottom. *Engineering and Science* **1960**, *23* (5), 22-36.

(10) Bogner, A.; Jouneau, P.-H.; Thollet, G.; Basset, D.; Gauthier, C. A History of Scanning Electron Microscopy Developments: Towards “Wet-STEM” Imaging. *Micron* **2007**, *38* (4), 390–401.

(11) Toumey, C. Plenty of Room, Plenty of History. *Nat. Nanotechnol.* **2009**, *4*, 783.

(12) Shew, A. Nanotech’s History: An Interesting, Interdisciplinary, Ideological Split. *Bull. Sci. Technol. Soc.* **2008**, *28* (5), 390–399.

(13) Drexler, E. K. *Engines of Creation.* Anchor Press/Doubleday: Garden City, NY, 1986.

(14) Schaller, R. R. Moore’s Law: Past, Present and Future. *IEEE Spectr.* **1997**, *34* (6), 52–59.

(15) Chen, Y. Nanofabrication by Electron Beam Lithography and Its Applications: A Review. *Microelectron. Eng.* **2015**, *135*, 57–72.

(16) Wu, B.; Kumar, A. Extreme Ultraviolet Lithography and Three Dimensional Integrated Circuit—A Review. *Appl. Phys. Rev.* **2014**, *1* (1), 011104.

(17) Mojarad, N.; Gobrecht, J.; Ekinci, Y. Beyond EUV Lithography: A Comparative Study of Efficient Photoresists' Performance. *Sci. Rep.* **2015**, *5* (1).

(18) Marty, J. D.; Mauzac, M. Molecular Imprinting: State of the Art and Perspectives. In *Microlithography · Molecular Imprinting*; Springer Berlin Heidelberg: Berlin, Heidelberg, 2005; Vol. 172, pp 1–35.

(19) Cardineau, B.; Del Re, R.; Marnell, M.; Al-Mashat, H.; Vockenhuber, M.; Ekinci, Y.; Sarma, C.; Freedman, D. A.; Brainard, R. L. Photolithographic Properties of Tin-Oxo Clusters Using Extreme Ultraviolet Light (13.5nm). *Microelectron. Eng.* **2014**, *127*, 44–50.

(20) Brainard, R. L.; Barclay, G. G.; Anderson, E. H.; Ocola, L. E. Resists for next Generation Lithography. *Microelectron. Eng.* **2002**, *61–62*, 707–715.

(21) Lio, A. EUV Resists: What's Next? *Proceedings SPIE 9776, Extreme Ultraviolet (EUV) Lithography VII.* 2016; p. 97760V.

(22) Stowers, J. K.; Telecky, A.; Kocsis, M.; Clark, B. L.; Keszler, D. A.; Grenville, A.; Anderson, C. N.; Naulleau, P. P. Directly Patterned Inorganic Hardmask for EUV Lithography. *Proceedings SPIE 7969, Extreme Ultraviolet (EUV) Lithography II*. 2011; p. 796915.

(23) Oleksak, R. P.; Ruther, R. E.; Luo, F.; Fairley, K. C.; Decker, S. R.; Stickle, W. F.; Johnson, D. W.; Garfunkel, E. L.; Herman, G. S.; Keszler, D. A. Chemical and Structural Investigation of High-Resolution Patterning with HafSO$_x$. *ACS Appl. Mater. Interfaces* **2014**, *6* (4), 2917–2921.

(24) Oleksak, R. P.; Ruther, R. E.; Luo, F.; Amador, J. M.; Decker, S. R.; Jackson, M. N.; Motley, J. R.; Stowers, J. K.; Johnson, D. W.; Garfunkel, E. L.; et al. Evaluation of Thermal and Radiation Induced Chemistries of Metal Oxo–Hydroxo Clusters for Next-Generation Nanoscale Inorganic Resists. *ACS Appl. Nano Mater.* **2018**, *1* (9), 4548–4556.

(25) Frederick, R. T.; Amador, J. M.; Goberna-Ferrón, S.; Nyman, M.; Keszler, D. A.; Herman, G. S. Mechanistic Study of HafSO$_x$ Extreme Ultraviolet Inorganic Resists. *J. Phys. Chem. C* **2018**, *122* (28), 16100–16112.

(26) Del Re, R.; Sortland, M.; Pasarelli, J.; Cardineau, B.; Ekinci, Y.; Vockenhuber, M.; Neisser, M.; Freedman, D.; Brainard, R. L. Low-LER Tin Carboxylate Photoresists Using EUV. *Proceedings SPIE 9422, Extreme Ultraviolet (EUV) Lithography VI.* 2015; p.942221.

(27) Haitjema, J.; Zhang, Y.; Ottosson, N.; Brouwer, A. M. Photoreactions of Tin Oxo Cages, Model EUV Photoresists. *J. Photopolym. Sci. Technol.* **2017**, *30* (1), 99–102.

(28) Haitjema, J.; Wu, L.; Giuliani, A.; Nahon, L.; Castellanos, S.; Brouwer, A. M. Photo-Induced Fragmentation of a Tin-Oxo Cage Compound. *J. Photopolym. Sci. Technol.* **2018**, *31* (2), 243–247.

(29) Zhang, Y.; Haitjema, J.; Baljozovic, M.; Vockenhuber, M.; Kazazis, D.; Jung, T. A.; Ekinci, Y.; Brouwer, A. M. Dual-Tone Application of a Tin-Oxo Cage Photoresist Under E-Beam and EUV Exposure. *J. Photopolym. Sci. Technol.* **2018**, *31* (2), 249–255.

(30) Frederick, R. T.; Diulus, J. T.; Hutchison, D. C.; Olsen, M. R.; Lyubinetsky, I.; Nyman, M.; Herman, G. S. Surface Characterization of Tin-Based Inorganic EUV Resists. *Proceedings SPIE 10586, Advances in Patterning Materials and Processes XXXV*. 2018; p. 1058607.

(31) Frederick, R. T.; Saha, S.; Diulus, J. T.; Luo, F.; Amador, J. M.; Park, D. H.; Garfunkel, E. L.; Keszler, D. A.; Herman, G. S. Thermal and Radiation Chemistry of Butyltin Oxo Hydroxo: A Model Inorganic Photoresist. *Microelectron. Eng.* **2019**, *15*, 26–31.

(32) Frederick, R. T.; Diulus, J. T.; Hutchison, D. C.; Nyman, M.; Herman, G. S. Effect of Oxygen on Thermal and Radiation Induced Chemistries in a Model Organotin Photoresist. *ACS Appl. Mater. Interfaces* **2019**, *11*, 4514-4522.

(33) Diulus, J. T.; Frederick, R. T.; Li, M.; Hutchison, D. C.; Olsen, M. R.; Lyubinetsky, I.; Árnadóttir, L.; Garfunkel, E. L.; Nyman, M.; Ogasawara, H.; et al. Ambient-Pressure X-Ray Photoelectron Spectroscopy Characterization of Radiation-Induced Chemistries of Organotin Clusters. *ACS Appl. Mater. Interfaces* **2019**, *11* (2), 2526–2534.

(34) Li, L.; Liu, X.; Pal, S.; Wang, S.; Ober, C. K.; Giannelis, E. P. Extreme Ultraviolet Resist Materials for Sub-7 Nm Patterning. *Chem. Soc. Rev.* **2017**, *46*, 4855-4866.

(35) Jiang, J.; Chakrabarty, S.; Yu, M.; Ober, C. K. Metal Oxide Nanoparticle Photoresists for EUV Patterning. *J. Photopolym. Sci. Technol.* **2014**, *27* (5), 663–666.

(36) Jiang, J.; Zhang, B.; Yu, M.; Li, L.; Neisser, M.; Sung Chun, J.; Giannelis, E. P.; Ober, C. K. Oxide Nanoparticle EUV (ONE) Photoresists: Current Understanding of the Unusual Patterning Mechanism. *J. Photopolym. Sci. Technol.* **2015**, *28* (4), 515–518.

(37) Wang, Y.; Fedin, I.; Zhang, H.; Talapin, D. V. Direct Optical Lithography of Functional Inorganic Nanomaterials. *Science* **2017**, *357* (6349), 385–388.

(38) Ganesan, R.; Dumond, J.; Saifullah, M. S. M.; Lim, S. H.; Hussain, H.; Low, H. Y. Direct Patterning of TiO_2 Using Step-and-Flash Imprint Lithography. *ACS Nano* **2012**, *6* (2), 1494–1502.

(39) Palazon, F.; Prato, M.; Manna, L. Writing on Nanocrystals: Patterning Colloidal Inorganic Nanocrystal Films through Irradiation-Induced Chemical Transformations of Surface Ligands. *J. Am. Chem. Soc.* **2017**, *139* (38), 13250–13259.

(40) Grenville, A.; Anderson, J. T.; Clark, B. L.; De Schepper, P.; Edson, J.; Greer, M.; Jiang, K.; Kocsis, M.; Meyers, S. T.; Stowers, J. K.; et al. Integrated Fab Process for Metal Oxide EUV Photoresist. *Proceedings SPIE 9425, Advances in Patterning Materials and Processes XXXII*. 2015; p. 94250S.

(41) Sciau, P. Transmission Electron Microscopy. In *Advances in Imaging and Electron Physics*; Elsevier, 2016; Vol. 198, pp 43–67.

(42) *Non-Destructive Microanalysis of Cultural Heritage Materials*, 1. ed.; Janssens, K. H. A., Barceló, D., Wilson, C. L., Eds.; Wilson & Wilson's comprehensive analytical chemistry; Elsevier: Amsterdam, 2004.

(43) McMullan, D. Scanning Electron Microscopy 1928-1965. *Scanning* **2006**, *17* (3), 175–185.

(44) Schreiner, M.; Melcher, M.; Uhlir, K. Scanning Electron Microscopy and Energy Dispersive Analysis: Applications in the Field of Cultural Heritage. *Anal. Bioanal. Chem.* **2007**, *387* (3), 737–747.

(45) Angelini, I.; Artioli, G.; Bellintani, P.; Diella, V.; Gemmi, M.; Polla, A.; Rossi, A. Chemical Analyses of Bronze Age Glasses from Frattesina Di Rovigo, Northern Italy. *J. Archaeol. Sci.* **2004**, *31* (8), 1175–1184.

(46) Sciau, P. Nanoparticles in Ancient Materials: The Metallic Lustre Decorations of Medieval Ceramics. In *The Delivery of Nanoparticles*; Hashim, A. A., Ed.; InTech, 2012.

(47) Freestone, I.; Meeks, N.; Sax, M.; Higgitt, C. The Lycurgus Cup — A Roman Nanotechnology. *Gold Bull.* **2007**, *40* (4), 270–277.

(48) Barber, D. J.; Freestone, I. C. An Investigation of the Origin of the Colour of the Lycurgus Cup by Analytical Transmission Electron Microscopy. *Archaeometry* **1990**, *32* (1), 33–45.

(49) Leonhardt, U. Invisibility Cup. *Nat. Photonics* **2007**, *1*, 207-208

(50) Cai, W.; Chettiar, U. K.; Kildishev, A. V.; Shalaev, V. M. Optical Cloaking with Metamaterials. *Nat. Photonics* **2007**, *1* (4), 224–227.

(51) Polette-Niewold, L. A.; Manciu, F. S.; Torres, B.; Alvarado, M.; Chianelli, R. R. Organic/Inorganic Complex Pigments: Ancient Colors Maya Blue. *J. Inorg. Biochem.* **2007**, *101* (11–12), 1958–1973.

(52) Micó-Vicent, B.; Martínez-Verdú, F. M.; Novikov, A.; Stavitskaya, A.; Vinokurov, V.; Rozhina, E.; Fakhrullin, R.; Yendluri, R.; Lvov, Y. Stabilized Dye-Pigment Formulations with Platy and Tubular Nanoclays. *Adv. Funct. Mater.* **2018**, *28* (27), 1703553.

(53) Dong, J.; Wang, Q.; Zhang, Y.; Zhu, Z.; Xu, X.; Zhang, J.; Wang, A. Colorful Superamphiphobic Coatings with Low Sliding Angles and High Durability Based on Natural Nanorods. *ACS Appl. Mater. Interfaces* **2017**, *9* (2), 1941–1952.

(54) Reibold, M.; Paufler, P.; Levin, A. A.; Kochmann, W.; Pätzke, N.; Meyer, D. C. Carbon Nanotubes in an Ancient Damascus Sabre. *Nature* **2006**, *444* (7117), 286–286.

(55) Verhoeven, J. D.; Pendray, A. H.; Dauksch, W. E.; Wagstaff, S. R. Damascus Steel Revisited. *JOM* **2018**, *70* (7), 1331–1336.

(56) Bassim, N.; Scott, K.; Giannuzzi, L. A. Recent Advances in Focused Ion Beam Technology and Applications. *MRS Bull.* **2014**, *39* (04), 317–325.

Chapter II

(1) Michael, J. R. High Resolution at Low Beam Energy in the SEM: Resolution Measurement of a Monochromated SEM. *Scanning* **2011**, *33* (3), 147–154.

(2) Phifer, D.; Tuma, L.; Vystavel, T.; Wandrol, P.; Young, R. J. Improving SEM IMaging Performance Using Beam Deceleration. *Microsc. Today* **2009**, *17* (4), 40–49.

(3) *Low Voltage Electron Microscopy: Principles and Applications*; Bell, D. C., Erdman, N., Eds.; Wiley, Published in association with the Royal Microscopical Society: Chichester, West Sussex, United Kingdom, 2013.

(4) Suga, M.; Asahina, S.; Sakuda, Y.; Kazumori, H.; Nishiyama, H.; Nokuo, T.; Alfredsson, V.; Kjellman, T.; Stevens, S. M.; Cho, H. S.; et al. Recent Progress in Scanning Electron Microscopy for the Characterization of Fine Structural Details of Nano Materials. *Prog. Solid State Chem.* **2014**, *42* (1–2), 1–21.

(5) Schatten, H.; Sibley, L. D.; Ris, H. Structural Evidence for Actin-like Filaments in Toxoplasma Gondii Using High-Resolution Low-Voltage Field Emission Scanning Electron Microscopy. *Microsc. Microanal. Off. J. Microsc. Soc. Am. Microbeam Anal. Soc. Microsc. Soc. Can.* **2003**, *9* (4), 330–335.

(6) Chen, Y. Nanofabrication by Electron Beam Lithography and Its Applications: A Review. *Microelectron. Eng.* **2015**, *135*, 57–72.

(7) Delachat, F.; Constancias, C.; Reche, J.; Dal'Zotto, B.; Pain, L.; Le Drogoff, B.; Chaker, M.; Margot, J. Determination of Spot Size and Acid Diffusion Length in Positive Chemically Amplified Resist for E-Beam Lithography at 100 and 5 KV. *J. Vac. Sci. Technol. B Nanotechnol. Microelectron. Mater. Process. Meas. Phenom.* **2014**, *32* (6), 06FJ02.

(8) Manfrinato, V. R.; Cheong, L. L.; Duan, H.; Winston, D.; Smith, H. I.; Berggren, K. K. Sub-5keV Electron-Beam Lithography in Hydrogen Silsesquioxane Resist. *Microelectron. Eng.* **2011**, *88* (10), 3070–3074.

(9) Liu, C.-H.; Ng, P. C. W.; Shen, Y.-T.; Chien, S.-W.; Tsai, K.-Y. Impacts of Point Spread Function Accuracy on Patterning Prediction and Proximity Effect Correction in Low-Voltage Electron-Beam–Direct-Write Lithography. *J. Vac. Sci. Technol. B Microelectron. Nanometer Struct.* **2013**, *31* (2), 021605.

(10) Rio, D.; Constancias, C.; Saied, M.; Icard, B.; Pain, L. Study on Line Edge Roughness for Electron Beam Acceleration Voltages from 50 to 5 KV. *J. Vac. Sci. Technol. B Microelectron. Nanometer Struct.* **2009**, *27* (6), 2512.

(11) Tilke, A.; Vogel, M.; Simmel, F.; Kriele, A.; Blick, R. H.; Lorenz, H.; Wharam, D. A.; Kotthaus, J. P. Low-Energy Electron-Beam Lithography Using Calixarene. *J. Vac. Sci. Technol. B Microelectron. Nanometer Struct.* **1999**, *17* (4), 1594.

(12) Oh, S. H.; Kim, J. G.; Kim, C. S.; Choi, D. S.; Chang, S.; Jeong, M. Y. The Fabrication of 3-D Nanostructures by a Low- Voltage EBL. *Appl. Surf. Sci.* **2011**, *257* (9), 3817–3823.

(13) Oleksak, R. P.; Ruther, R. E.; Luo, F.; Fairley, K. C.; Decker, S. R.; Stickle, W. F.; Johnson, D. W.; Garfunkel, E. L.; Herman, G. S.; Keszler, D. A. Chemical and Structural Investigation of High-Resolution Patterning with HafSO$_x$. *ACS Appl. Mater. Interfaces* **2014**, *6* (4), 2917–2921.

(14) Anderson, J. T.; Munsee, C. L.; Hung, C. M.; Phung, T. M.; Herman, G. S.; Johnson, D. C.; Wager, J. F.; Keszler, D. A. Solution-Processed $HafSO_x$ and $ZircSO_x$ Inorganic Thin-Film Dielectrics and Nanolaminates. *Adv. Funct. Mater.* **2007**, *17* (13), 2117–2124.

(15) Telecky, A.; Xie, P.; Stowers, J.; Grenville, A.; Smith, B.; Keszler, D. A. Photopatternable Inorganic Hardmask. *J. Vac. Sci. Technol. B Microelectron. Nanometer Struct.* **2010**, *28* (6), C6S19.

(16) Stowers, J.; Keszler, D. A. High Resolution, High Sensitivity Inorganic Resists. *Microelectron. Eng.* **2009**, *86* (4–6), 730–733.

(17) Demers, H.; Poirier-Demers, N.; Couture, A. R.; Joly, D.; Guilmain, M.; de Jonge, N.; Drouin, D. Three-Dimensional Electron Microscopy Simulation with the CASINO Monte Carlo Software. *Scanning* **2011**, *33* (3), 135–146.

(18) Schaffer, M.; Schaffer, B.; Ramasse, Q. Sample Preparation for Atomic-Resolution STEM at Low Voltages by FIB. *Ultramicroscopy* **2012**, *114*, 62–71.

(19) Stowers, J. K.; Telecky, A.; Kocsis, M.; Clark, B. L.; Keszler, D. A.; Grenville, A.; Anderson, C. N.; Naulleau, P. P. Directly Patterned Inorganic Hardmask for EUV Lithography. *Proceedings SPIE 7969, Extreme Ultraviolet (EUV) Lithography II.* 2011; p. 796915.

(20) Cui, Z. *Nanofabrication: Principles, Capabilities and Limits*; Springer: New York, NY, 2008.

(21) Phifer, D.; Tuma, L.; Vystavel, T.; Wandrol, P.; Young, R. J. Improving SEM Imaging Performance Using Beam Deceleration. *Microsc. Today* **2009**, *17*, 40-49.

Chapter III

(1) Lambourne, H. CCCI.—Derivatives of Methylstannonic Acid; Their Bearing upon Its Constitution. *J. Chem. Soc. Trans.* **1922**, *121* (0), 2533–2540.

(2) Chandrasekhar, V.; Schmid, C. G.; Burton, S. D.; Holmes, J. M.; Day, R. O.; Holmes, R. R. New Drum and Ladder Organooxotin Carboxylates. *Inorg. Chem.* **1987**, *26* (7), 1050–1056.

(3) Day, R. O.; Chandrasekhar, V.; Swamy, K. C. K.; Holmes, J. M.; Burton, S. D.; Holmes, R. R. Organotin Clusters. 3. Novel Drums and Mixed-Drum Organooxotin Clusters from Carboxylic, Phosphinic, and Phosphoric Acids. *Inorg. Chem.* **1988**, *27* (16), 2887–2893.

(4) Holmes, R. R.; Swamy, K. C. K.; Schmid, C. G.; Day, R. O. Organotin Clusters. 4. Cubic, Butterfly, and Oxygen-Capped Clusters of N-Butyloxotin Phosphinates. A New Class of Organotin Compounds. *J. Am. Chem. Soc.* **1988**, *110* (21), 7060–7066.

(5) Holmes, R. R. Organotin Cluster Chemistry. *Acc. Chem. Res.* **1989**, *22* (5), 190–197.

(6) Ribot, F.; Banse, F.; Diter, F.; Sanchez, C. Hybrid Organic-Inorganic Supramolecular Assemblies Made from Butyltin Oxo-Hydroxo Nanobuilding Blocks and Dicarboxylates. *New J. Chem.* **1995**, *19*, 1145–1153.

(7) Banse, F.; Ribot, F.; Toledano, P.; Maquet, J.; Sanchez, C. Hydrolysis of Monobutyltin Trialkoxides: Synthesis and Characterizations of $\{(BuSn)_{12}O_{14}(OH)_6\}(OH)_2$. *Inorg. Chem.* **1995**, *34* (25), 6371–6379.

(8) Eychenne-Baron, C.; Ribot, F.; Steunou, N.; Sanchez, C.; Fayon, F.; Biesemans, M.; Martins, J. C.; Willem, R. Reaction of Butyltin Hydroxide Oxide with *p*-Toluenesulfonic Acid: Synthesis, X-Ray Crystal Analysis, and Multinuclear NMR Characterization of $\{(BuSn)_{12}O_{14}(OH)_6\}(4\text{-}CH_3C_6H_4SO_3)_2$. *Organometallics* **2000**, *19* (10), 1940–1949.

(9) Abbas, S. M.; Ali, S.; Hussain, S. T.; Shahzadi, S. Review: Structural Diversity in organotin(IV) Dithiocarboxylates and Carboxylates. *J. Coord. Chem.* **2013**, *66* (13), 2217–2234.

(10) Chandrasekhar, V.; Nagendran, S.; Baskar, V. Organotin Assemblies Containing Sn□O Bonds. *Coord. Chem. Rev.* **2002**, *235* (1-2), 1–52.

(11) Tiekink, E. R. T. Structural Chemistry of Organotin Carboxylates: A Review of the Crystallographic Literature. *Appl. Organomet. Chem.* **1991**, *5* (1), 1–23.

(12) Carraro, M.; Gross, S. Hybrid Materials Based on the Embedding of Organically Modified Transition Metal Oxoclusters or Polyoxometalates into Polymers for Functional Applications: A Review. *Materials* **2014**, *7* (5), 3956–3989.

(13) Dolbecq, A.; Dumas, E.; Mayer, C. R.; Mialane, P. Hybrid Organic−Inorganic Polyoxometalate Compounds: From Structural Diversity to Applications. *Chem. Rev.* **2010**, *110* (10), 6009–6048.

(14) Chandrasekhar, V.; Nagendran, S.; Bansal, S.; Kozee, M. A.; Powell, D. R. An Iron Wheel on a Tin Drum: A Novel Assembly of a Hexaferrocene Unit on a Tin–Oxygen Cluster. *Angew. Chem. Int. Ed.* **2000**, *39* (10), 1833–1835.

(15) Tariq, M.; Muhammad, N.; Sirajuddin, M.; Ali, S.; Shah, N. A.; Khalid, N.; Tahir, M. N.; Khan, M. R. Synthesis, Spectroscopic Characterization, X-Ray Structures, Biological Screenings, DNA Interaction Study and Catalytic Activity of organotin(IV) 3-(4-Flourophenyl)-2-Methylacrylic Acid Derivatives. *J. Organomet. Chem.* **2013**, *723*, 79–89.

(16) Rocha, C. S.; de Morais, B. P.; Rodrigues, B. L.; Donnici, C. L.; de Lima, G. M.; Ardisson, J. D.; Takahashi, J. A.; Bitzer, R. S. Spectroscopic and X-Ray Structural Characterization of New Organotin Carboxylates and Their in Vitro Antifungal Activities. *Polyhedron* **2016**, *117*, 35–47.

(17) Amir, M. K.; Khan, S.; Zia-ur-Rehman; Shah, A.; Butler, I. S. Anticancer Activity of Organotin(IV) Carboxylates. *Inorganica Chim. Acta* **2014**, *423*, 14–25.

(18) *Tin Chemistry*; Davies, A. G., Gielen, M., Pannell, K. H., Tiekink, E. R. T., Eds.; John Wiley & Sons, Ltd: Chichester, UK, 2008.

(19) Cardineau, B.; Del Re, R.; Marnell, M.; Al-Mashat, H.; Vockenhuber, M.; Ekinci, Y.; Sarma, C.; Freedman, D. A.; Brainard, R. L. Photolithographic Properties of Tin-Oxo Clusters Using Extreme Ultraviolet Light (13.5nm). *Microelectron. Eng.* **2014**, *127*, 44–50.

(20) Cardineau, B.; Del Re, R.; Al-Mashat, H.; Marnell, M.; Vockenhuber, M.; Ekinci, Y.; Sarma, C.; Neisser, M.; Freedman, D. A.; Brainard, R. L. EUV Resists Based on Tin-Oxo Clusters. *Proceedings SPIE 9051, Advances in Patterning Materials and Processes XXXI.* 2014; p. 90511B.

(21) Del Re, R.; Sortland, M.; Pasarelli, J.; Cardineau, B.; Ekinci, Y.; Vockenhuber, M.; Neisser, M.; Freedman, D.; Brainard, R. L. Low-LER Tin Carboxylate Photoresists Using EUV. *Proceedings SPIE 9422, Extreme Ultraviolet (EUV) Lithography VI.* 2015; p. 942221.

(22) Grenville, A.; Anderson, J. T.; Clark, B. L.; De Schepper, P.; Edson, J.; Greer, M.; Jiang, K.; Kocsis, M.; Meyers, S. T.; Stowers, J. K.; et al. Integrated Fab Process for Metal Oxide EUV Photoresist. *Proceedings SPIE 9425, Advances in Patterning Materials and Processes XXXII.* 2015; p.94250S.

(23) Holmes, R. R.; Schmid, C. G.; Chandrasekhar, V.; Day, R. O.; Holmes, J. M. Oxo Carboxylate Tin Ladder Clusters. A New Structural Class of Organotin Compounds. *J. Am. Chem. Soc.* **1987**, *109* (5), 1408–1414.

(24) Chandrasekhar, V.; Day, R. O.; Holmes, R. R. A New Structural Form of Tin Octahedrally Coordinated in a Drum-Shaped Molecule. *Inorg. Chem.* **1985**, *24* (13), 1970–1971.

(25) Chandrasekhar, V.; Gopal, K.; Nagendran, S.; Steiner, A.; Zacchini, S. Influence of Aromatic Substituents on the Supramolecular Architectures of Monoorganooxotin Drums. *Cryst. Growth Des.* **2006**, *6* (1), 267–273.

(26) M. Lukeman, CRC Handbook of Organic Photochemistry and Photobiology, CRC, 2012.

Chapter IV

(1) Li, L.; Liu, X.; Pal, S.; Wang, S.; Ober, C. K.; Giannelis, E. P. Extreme Ultraviolet Resist Materials for Sub-7 Nm Patterning. *Chem. Soc. Rev.* **2017**, *46*, 4855-4866.

(2) Wu, B.; Kumar, A. Extreme Ultraviolet Lithography and Three Dimensional Integrated Circuit—A Review. *Appl. Phys. Rev.* **2014**, *1*, 011104.

(3) Pirati, A.; Peeters, R.; Smith, D.; Lok, S.; van Noordenburg, M.; van Es, R.; Verhoeven, E.; Meijer, H.; Minnaert, A.; van der Horst, J.-W.; et al. EUV Lithography Performance for Manufacturing: Status and Outlook. *Proceedings SPIE 9776, Extreme Ultraviolet (EUV) Lithography VII.* 2016; p. 97760A.

(4) Jiang, J.; Zhang, B.; Yu, M.; Li, L.; Neisser, M.; Sung Chun, J.; Giannelis, E. P.; Ober, C. K. Oxide Nanoparticle EUV (ONE) Photoresists: Current Understanding of the Unusual Patterning Mechanism. *J. Photopolym. Sci. Technol.* **2015**, *28*, 515–518.

(5) Jiang, J.; Chakrabarty, S.; Yu, M.; Ober, C. K. Metal Oxide Nanoparticle Photoresists for EUV Patterning. *J. Photopolym. Sci. Technol.* **2014**, *27*, 663–666.

(6) Bae, W. J.; Trikeriotis, M.; Sha, J.; Schwartz, E. L.; Rodriguez, R.; Zimmerman, P.; Giannelis, E. P.; Ober, C. K. High Refractive Index and High Transparency HfO2 Nanocomposites for next Generation Lithography. *J. Mater. Chem.* **2010**, *20*, 5186-5189.

(7) Trikeriotis, M.; Krysaki, M.; Chung, Y. S.; Ouyang, C.; Cardineau, B.; Brainard, R.; Ober, C. K.; Giannelis, E. P.; Cho, K. Nanoparticle Photoresists from HfO2 and ZrO2 for EUV Patterning. *J. Photopolym. Sci. Technol.* **2012**, *25*, 583–586.

(8) Oleksak, R. P.; Ruther, R. E.; Luo, F.; Fairley, K. C.; Decker, S. R.; Stickle, W. F.; Johnson, D. W.; Garfunkel, E. L.; Herman, G. S.; Keszler, D. A. Chemical and Structural Investigation of High-Resolution Patterning with HafSO$_x$. *ACS Appl. Mater. Interfaces* **2014**, *6*, 2917–2921.

(9) Cardineau, B.; Del Re, R.; Marnell, M.; Al-Mashat, H.; Vockenhuber, M.; Ekinci, Y.; Sarma, C.; Freedman, D. A.; Brainard, R. L. Photolithographic Properties of Tin-Oxo Clusters Using Extreme Ultraviolet Light (13.5nm). *Microelectron. Eng.* **2014**, *127*, 44–50.

(10) Del Re, R.; Sortland, M.; Pasarelli, J.; Cardineau, B.; Ekinci, Y.; Vockenhuber, M.; Neisser, M.; Freedman, D.; Brainard, R. L. Low-LER Tin Carboxylate Photoresists Using EUV. *Proceedings SPIE 9422, Extreme Ultraviolet (EUV) Lithography VI.* 2015; p. 942221.

(11) Grenville, A.; Anderson, J. T.; Clark, B. L.; De Schepper, P.; Edson, J.; Greer, M.; Jiang, K.; Kocsis, M.; Meyers, S. T.; Stowers, J. K.; et al. Integrated Fab Process for Metal Oxide EUV Photoresist. *Proceedings SPIE 9425, Advances in Patterning Materials and Processes XXXII.* 2015; p. 94250S.

(12) Stowers, J.; Keszler, D. A. High Resolution, High Sensitivity Inorganic Resists. *Microelectron. Eng.* **2009**, *86*, 730–733.

(13) Telecky, A.; Xie, P.; Stowers, J.; Grenville, A.; Smith, B.; Keszler, D. A. Photopatternable Inorganic Hardmask. *J. Vac. Sci. Technol. B Microelectron. Nanometer Struct.* **2010**, *28*, C6S19.

(14) Wu, L.; Tiekink, M.; Giuliani, A.; Nahon, L.; Castellanos, S. Tuning Photoionization Mechanisms of Molecular Hybrid Materials for EUV Lithography Applications. *J. Mater. Chem. C.* **2019**, *7*, 33-37.

(15) Lio, A. EUV Resists: What's Next? *Proceedings SPIE 9776, Extreme Ultraviolet (EUV) Lithography VII*. 2016; p. 97760V.

(16) Stowers, J. K.; Telecky, A.; Kocsis, M.; Clark, B. L.; Keszler, D. A.; Grenville, A.; Anderson, C. N.; Naulleau, P. P. Directly Patterned Inorganic Hardmask for EUV Lithography. *Proceedings SPIE 7969, Extreme Ultraviolet (EUV) Lithography II*. 2011; p. 796915.

(17) Mojarad, N.; Gobrecht, J.; Ekinci, Y. Beyond EUV Lithography: A Comparative Study of Efficient Photoresists' Performance. *Sci. Rep.* **2015**, *9235.*

(18) Wang, Y.; Fedin, I.; Zhang, H.; Talapin, D. V. Direct Optical Lithography of Functional Inorganic Nanomaterials. *Science* **2017**, *357*, 385–388.

(19) Oleksak, R. P.; Ruther, R. E.; Luo, F.; Amador, J. M.; Decker, S. R.; Jackson, M. N.; Motley, J. R.; Stowers, J. K.; Johnson, D. W.; Garfunkel, E. L.; et al. Evaluation of Thermal and Radiation Induced Chemistries of Metal Oxo–Hydroxo Clusters for Next-Generation Nanoscale Inorganic Resists. *ACS Appl. Nano Mater.* **2018**, *1*, 4548–4556.

(20) Frederick, R. T.; Amador, J. M.; Goberna-Ferrón, S.; Nyman, M.; Keszler, D. A.; Herman, G. S. Mechanistic Study of HafSO$_x$ Extreme Ultraviolet Inorganic Resists. *J. Phys. Chem. C* **2018**, *122*, 16100–16112.

(21) Ganesan, R.; Dumond, J.; Saifullah, M. S. M.; Lim, S. H.; Hussain, H.; Low, H. Y. Direct Patterning of TiO_2 Using Step-and-Flash Imprint Lithography. *ACS Nano* **2012**, *6*, 1494–1502.

(22) Palazon, F.; Prato, M.; Manna, L. Writing on Nanocrystals: Patterning Colloidal Inorganic Nanocrystal Films through Irradiation-Induced Chemical Transformations of Surface Ligands. *J. Am. Chem. Soc.* **2017**, *139*, 13250–13259.

(23) Haitjema, J.; Zhang, Y.; Ottosson, N.; Brouwer, A. M. Photoreactions of Tin Oxo Cages, Model EUV Photoresists. *J. Photopolym. Sci. Technol.* **2017**, *30*, 99–102.

(24) Frederick, R. T.; Diulus, J. T.; Hutchison, D. C.; Olsen, M. R.; Lyubinetsky, I.; Nyman, M.; Herman, G. S. Surface Characterization of Tin-Based Inorganic EUV Resists. *Proceedings SPIE 10586, Advances in Patterning Materials and Processes XXXV.* 2018; p. 1058607.

(25) Frederick, R. T.; Saha, S.; Diulus, J. T.; Luo, F.; Amador, J. M.; Park, D. H.; Garfunkel, E. L.; Keszler, D. A.; Herman, G. S. Thermal and Radiation Chemistry of Butyltin Oxo Hydroxo: A Model Inorganic Photoresist. *Microelectron. Eng.* **2019**, *15*, 26–31.

(26) Frederick, R. T.; Diulus, J. T.; Hutchison, D. C.; Nyman, M.; Herman, G. S. Effect of Oxygen on Thermal and Radiation Induced Chemistries in a Model Organotin Photoresist. *ACS Appl. Mater. Interfaces* **2019**, *11*, 4514-4522.

(27) Diulus, J. T.; Frederick, R. T.; Li, M.; Hutchison, D. C.; Olsen, M. R.; Lyubinetsky, I.; Árnadóttir, L.; Garfunkel, E. L.; Nyman, M.; Ogasawara, H.; et al. Ambient-Pressure X-Ray Photoelectron Spectroscopy Characterization of Radiation-Induced Chemistries of Organotin Clusters. *ACS Appl. Mater. Interfaces* **2019**, *11*, 2526–2534.

(28) Haitjema, J.; Wu, L.; Giuliani, A.; Nahon, L.; Castellanos, S.; Brouwer, A. M. Photo-Induced Fragmentation of a Tin-Oxo Cage Compound. *J. Photopolym. Sci. Technol.* **2018**, *31*, 243–247.

(29) Holmes, R. R.; Swamy, K. C. K.; Schmid, C. G.; Day, R. O. Organotin Clusters. 4. Cubic, Butterfly, and Oxygen-Capped Clusters of n-Butyloxotin Phosphinates. A New Class of Organotin Compounds. *J. Am. Chem. Soc.* **1988**, *110*, 7060–7066.

(30) Holmes, R. R. Organotin Cluster Chemistry. *Acc. Chem. Res.* **1989**, *22*, 190–197.

(31) Chandrasekhar, V.; Schmid, C. G.; Burton, S. D.; Holmes, J. M.; Day, R. O.; Holmes, R. R. New Drum and Ladder Organooxotin Carboxylates. *Inorg. Chem.* **1987**, *26*, 1050–1056.

(32) Abbas, S. M.; Ali, S.; Hussain, S. T.; Shahzadi, S. Review: Structural Diversity in Organotin(IV) Dithiocarboxylates and Carboxylates. *J. Coord. Chem.* **2013**, *66*, 2217–2234.

(33) Tiekink, E. R. T. Structural Chemistry of Organotin Carboxylates: A Review of the Crystallographic Literature. *Appl. Organomet. Chem.* **1991**, *5*, 1–23.

(34) Eychenne-Baron, C.; Ribot, F.; Steunou, N.; Sanchez, C.; Fayon, F.; Biesemans, M.; Martins, J. C.; Willem, R. Reaction of Butyltin Hydroxide Oxide with *p* -Toluenesulfonic Acid: Synthesis, X-Ray Crystal Analysis, and Multinuclear NMR Characterization of $(BuSn)_{12}O_{14}(OH)_6(4\text{-}CH_3C_6H_4SO_3)_2$. *Organometallics* **2000**, *19*, 1940–1949.

(35) Eychenne-Baron, C.; Ribot, F.; Sanchez, C. New Synthesis of the Nanobuilding Block $(BuSn)_{12}O_{14}(OH)_6^{2+}$ and Exchange Properties of $(BuSn)_{12}O_{14}(OH)_6(O_3SC_6H_4CH_3)_2$. *J. Organomet. Chem.* **1998**, *567*, 137–142.

(36) Sharps, M. C.; Marsh, D. A.; Zakharov, L. N.; Hutchison, J. E.; Johnson, D. W. Implications of Crystal Structure on Organotin Carboxylate Photoresists. *Cryst. Res. Technol.* **2017**, 1700081.

(37) Wolf, S.; Tauber, R. N. *Silicon Processing for the VLSI Era*; Lattice Press: Sunset Beach, Calif, 1986.

(38) Themlin, J.-M.; Chtaïb, M.; Henrard, L.; Lambin, P.; Darville, J.; Gilles, J.-M. Characterization of Tin Oxides by X-Ray-Photoemission Spectroscopy. *Phys. Rev. B* **1992**, *46*, 2460–2466.

(39) Batzill, M.; Diebold, U. The Surface and Materials Science of Tin Oxide. *Prog. Surf. Sci.* **2005**, *79*, 47–154.

(40) Weidner, M. Fermi Level Determination in Tin Oxide by Photoelectron Spectroscopy. Ph.D. Dissertation, TU Darmstadt, 2015.

(41) Renard, L.; Babot, O.; Saadaoui, H.; Fuess, H.; Brötz, J.; Gurlo, A.; Arveux, E.; Klein, A.; Toupance, T. Nanoscaled Tin Dioxide Films Processed from Organotin-Based Hybrid Materials: An Organometallic Route toward Metal Oxide Gas Sensors. *Nanoscale* **2012**, *4*, 6806.

(42) Themlin, J. M.; Sporken, R.; Darville, J.; Caudano, R.; Gilles, J. M.; Johnson, R. L. Resonant-Photoemission Study of SnO 2 : Cationic Origin of the Defect Band-Gap States. *Phys. Rev. B* **1990**, *42*, 11914–11925.

(43) Schleife, A.; Varley, J. B.; Fuchs, F.; Rödl, C.; Bechstedt, F.; Rinke, P.; Janotti, A.; Van de Walle, C. G. Tin Dioxide from First Principles: Quasiparticle Electronic States and Optical Properties. *Phys. Rev. B* **2011**, *83*, 035116.

(44) Zhang, Y.; Haitjema, J.; Baljozovic, M.; Vockenhuber, M.; Kazazis, D.; Jung, T. A.; Ekinci, Y.; Brouwer, A. M. Dual-Tone Application of a Tin-Oxo Cage Photoresist Under E-Beam and EUV Exposure. *J. Photopolym. Sci. Technol.* **2018**, *31*, 249–255.

(45) Nam, C.-Y.; Stein, A.; Kisslinger, K. Direct Fabrication of High Aspect-Ratio Metal Oxide Nanopatterns via Sequential Infiltration Synthesis in Lithographically Defined SU-8 Templates. *J. Vac. Sci. Technol. B Nanotechnol. Microelectron. Mater. Process. Meas. Phenom.* **2015**, *33*, 06F201.

Chapter V

(1) Wu, W. Inorganic Nanomaterials for Printed Electronics: A Review. *Nanoscale* **2017**, *9* (22), 7342–7372.

(2) Li, H.; Tang, Y.; Guo, W.; Liu, H.; Zhou, L.; Smolinski, N. Polyfluorinated Electrolyte for Fully Printed Carbon Nanotube Electronics. *Adv. Funct. Mater.* **2016**, *26* (38), 6914–6920.

(3) Zhao, J.; Gao, Y.; Gu, W.; Wang, C.; Lin, J.; Chen, Z.; Cui, Z. Fabrication and Electrical Properties of All-Printed Carbon Nanotube Thin Film Transistors on Flexible Substrates. *J. Mater. Chem.* **2012**, *22* (38), 20747.

(4) Homenick, C. M.; James, R.; Lopinski, G. P.; Dunford, J.; Sun, J.; Park, H.; Jung, Y.; Cho, G.; Malenfant, P. R. L. Fully Printed and Encapsulated SWCNT-Based Thin Film Transistors via a Combination of R2R Gravure and Inkjet Printing. *ACS Appl. Mater. Interfaces* **2016**, *8* (41), 27900–27910.

(5) Hwang, K.; Jung, Y.-S.; Heo, Y.-J.; Scholes, F. H.; Watkins, S. E.; Subbiah, J.; Jones, D. J.; Kim, D.-Y.; Vak, D. Toward Large Scale Roll-to-Roll Production of Fully Printed Perovskite Solar Cells. *Adv. Mater.* **2015**, *27* (7), 1241–1247.

(6) Cheng, Y.-B.; Pascoe, A.; Huang, F.; Peng, Y. Print Flexible Solar Cells. *Nature* **2016**, *539* (7630), 488–489.

(7) Kim, J.; Kumar, R.; Bandodkar, A. J.; Wang, J. Advanced Materials for Printed Wearable Electrochemical Devices: A Review. *Adv. Electron. Mater.* **2017**, *3* (1), 1600260.

(8) Li, Y.; Zhang, Z.; Su, M.; Huang, Z.; Li, Z.; Li, F.; Pan, Q.; Ren, W.; Hu, X.; Li, L.; et al. A General Strategy for Printing Colloidal Nanomaterials into One-Dimensional Micro/Nanolines. *Nanoscale* **2018**, *10* (47), 22374–22380.

(9) Wang, Y.; Fedin, I.; Zhang, H.; Talapin, D. V. Direct Optical Lithography of Functional Inorganic Nanomaterials. *Science* **2017**, *357* (6349), 385–388.

(10) Striccoli, M. Photolithography Based on Nanocrystals. *Science* **2017**, *357* (6349), 353–354.

(11) Li, L.; Chakrabarty, S.; Spyrou, K.; Ober, C. K.; Giannelis, E. P. Studying the Mechanism of Hybrid Nanoparticle Photoresists: Effect of Particle Size on Photopatterning. *Chem. Mater.* **2015**, *27* (14), 5027–5031.

(12) Jiang, J.; Chakrabarty, S.; Yu, M.; Ober, C. K. Metal Oxide Nanoparticle Photoresists for EUV Patterning. *J. Photopolym. Sci. Technol.* **2014**, *27* (5), 663–666.

(13) Jiang, J.; Zhang, B.; Yu, M.; Li, L.; Neisser, M.; Sung Chun, J.; Giannelis, E. P.; Ober, C. K. Oxide Nanoparticle EUV (ONE) Photoresists: Current Understanding of the Unusual Patterning Mechanism. *J. Photopolym. Sci. Technol.* **2015**, *28* (4), 515–518.

(14) Kothari, R.; Beaulieu, M. R.; Hendricks, N. R.; Li, S.; Watkins, J. J. Direct Patterning of Robust One-Dimensional, Two-Dimensional, and Three-Dimensional Crystalline Metal Oxide Nanostructures Using Imprint Lithography and Nanoparticle Dispersion Inks. *Chem. Mater.* **2017**, *29* (9), 3908–3918.

(15) Ganesan, R.; Dumond, J.; Saifullah, M. S. M.; Lim, S. H.; Hussain, H.; Low, H. Y. Direct Patterning of TiO_2 Using Step-and-Flash Imprint Lithography. *ACS Nano* **2012**, *6* (2), 1494–1502.

(16) Wang, W. M.; Stoltenberg, R. M.; Liu, S.; Bao, Z. Direct Patterning of Gold Nanoparticles Using Dip-Pen Nanolithography. *ACS Nano* **2008**, *2* (10), 2135–2142.

(17) Palazon, F.; Prato, M.; Manna, L. Writing on Nanocrystals: Patterning Colloidal Inorganic Nanocrystal Films through Irradiation-Induced Chemical Transformations of Surface Ligands. *J. Am. Chem. Soc.* **2017**, *139* (38), 13250–13259.

(18) Koh, A. L.; Fernández-Domínguez, A. I.; McComb, D. W.; Maier, S. A.; Yang, J. K. W. High-Resolution Mapping of Electron-Beam-Excited Plasmon Modes in Lithographically Defined Gold Nanostructures. *Nano Lett.* **2011**, *11* (3), 1323–1330.

(19) Saifullah, M. S. M.; Asbahi, M.; Binti-Kamran Kiyani, M.; Tripathy, S.; Ong, E. A. H.; Ibn Saifullah, A.; Tan, H. R.; Dutta, T.; Ganesan, R.; Valiyaveettil, S.; et al. Direct Patterning of Zinc Sulfide on a Sub-10 Nanometer Scale *via* Electron Beam Lithography. *ACS Nano* **2017**, *11* (10), 9920–9929.

(20) Nandwana, V.; Subramani, C.; Yeh, Y.-C.; Yang, B.; Dickert, S.; Barnes, M. D.; Tuominen, M. T.; Rotello, V. M. Direct Patterning of Quantum Dot Nanostructures via Electron Beam Lithography. *J. Mater. Chem.* **2011**, *21* (42), 16859.

(21) Nam, C.-Y.; Stein, A.; Kisslinger, K. Direct Fabrication of High Aspect-Ratio Metal Oxide Nanopatterns via Sequential Infiltration Synthesis in Lithographically Defined SU-8 Templates. *J. Vac. Sci. Technol. B Nanotechnol. Microelectron. Mater. Process. Meas. Phenom.* **2015**, *33* (6), 06F201.

(22) Schirmeisen, A.; Taskiran, A.; Fuchs, H.; Bracht, H.; Murugavel, S.; Roling, B. Fast Interfacial Ionic Conduction in Nanostructured Glass Ceramics. *Phys. Rev. Lett.* **2007**, *98* (22).

(23) Rosenflanz, A.; Frey, M.; Endres, B.; Anderson, T.; Richards, E.; Schardt, C. Bulk Glasses and Ultrahard Nanoceramics Based on Alumina and Rare-Earth Oxides. *Nature* **2004**, *430* (7001), 761–764.

(24) Falcão-Filho, E. L.; Bosco, C. A. C.; Maciel, G. S.; Acioli, L. H.; de Araújo, C. B.; Lipovskii, A. A.; Tagantsev, D. K. Third-Order Optical Nonlinearity of a Transparent Glass Ceramic Containing Sodium Niobate Nanocrystals. *Phys. Rev. B* **2004**, *69* (13).

(25) Llordés, A.; Garcia, G.; Gazquez, J.; Milliron, D. J. Tunable Near-Infrared and Visible-Light Transmittance in Nanocrystal-in-Glass Composites. *Nature* **2013**, *500* (7462), 323–326.

(26) Llordes, A.; Hammack, A. T.; Buonsanti, R.; Tangirala, R.; Aloni, S.; Helms, B. A.; Milliron, D. J. Polyoxometalates and Colloidal Nanocrystals as Building Blocks for Metal Oxide Nanocomposite Films. *J. Mater. Chem.* **2011**, *21* (31), 11631.

(27) Ito, D.; Yokoyama, S.; Zaikova, T.; Masuko, K.; Hutchison, J. E. Synthesis of Ligand-Stabilized Metal Oxide Nanocrystals and Epitaxial Core/Shell Nanocrystals *via* a Lower-Temperature Esterification Process. *ACS Nano* **2014**, *8* (1), 64–75.

(28) Jansons, A. W.; Hutchison, J. E. Continuous Growth of Metal Oxide Nanocrystals: Enhanced Control of Nanocrystal Size and Radial Dopant Distribution. *ACS Nano* **2016**, *10* (7), 6942–6951.

(29) Crockett, B. M.; Jansons, A. W.; Koskela, K. M.; Johnson, D. W.; Hutchison, J. E. Radial Dopant Placement for Tuning Plasmonic Properties in Metal Oxide Nanocrystals. *ACS Nano* **2017**, *11* (8), 7719–7728.

(30) Dong, A.; Ye, X.; Chen, J.; Kang, Y.; Gordon, T.; Kikkawa, J. M.; Murray, C. B. A Generalized Ligand-Exchange Strategy Enabling Sequential Surface Functionalization of Colloidal Nanocrystals. *J. Am. Chem. Soc.* **2011**, *133* (4), 998–1006.

(31) Kim, J.; Ong, G. K.; Wang, Y.; LeBlanc, G.; Williams, T. E.; Mattox, T. M.; Helms, B. A.; Milliron, D. J. Nanocomposite Architecture for Rapid, Spectrally-Selective Electrochromic Modulation of Solar Transmittance. *Nano Lett.* **2015**, *15* (8), 5574–5579.

(32) Lin, X. M.; Parthasarathy, R.; Jaeger, H. M. Direct Patterning of Self-Assembled Nanocrystal Monolayers by Electron Beams. *Appl. Phys. Lett.* **2001**, *78* (13), 1915–1917.

(33) Hogg, C. R.; Majetich, S. A.; Bain, J. A. Investigating Pattern Transfer in the Small-Gap Regime Using Electron-Beam Stabilized Nanoparticle Array Etch Masks. *IEEE Trans. Magn.* **2010**, *46* (6), 2307–2310.

(34) Palazon, F.; Akkerman, Q. A.; Prato, M.; Manna, L. X-Ray Lithography on Perovskite Nanocrystals Films: From Patterning with Anion-Exchange Reactions to Enhanced Stability in Air and Water. *ACS Nano* **2016**, *10* (1), 1224–1230.

(35) Miszta, K.; Greullet, F.; Marras, S.; Prato, M.; Toma, A.; Arciniegas, M.; Manna, L.; Krahne, R. Nanocrystal Film Patterning by Inhibiting Cation Exchange via Electron-Beam or X-Ray Lithography. *Nano Lett.* **2014**, *14* (4), 2116–2122.

Chapter VI

(1) *Nanoscience and Cultural Heritage*; Dillmann, P., Bellot-Gurlet, L., Nenner, I., Eds.; Atlantis Press: Paris, 2016.

(2) *Non-Destructive Microanalysis of Cultural Heritage Materials*, 1. ed.; Janssens, K. H. A., Barceló, D., Wilson, C. L., Eds.; Wilson & Wilson's comprehensive analytical chemistry; Elsevier: Amsterdam, 2004.

(3) Sciau, P.; Salles, P.; Roucau, C.; Mehta, A.; Benassayag, G. Applications of Focused Ion Beam for Preparation of Specimens of Ancient Ceramic for Electron Microscopy and Synchrotron X-Ray Studies. *Micron* **2009**, *40* (5–6), 597–604.

(4) Haswell, R.; Zeile, U.; Mensch, K. Van Gogh's Painting Grounds: An Examination of Barium Sulphate Extender Using Analytical Electron Microscopy – SEM/FIB/TEM/EDX. *Microchim. Acta* **2008**, *161* (3–4), 363–369.

(5) Carl, M.; Smith, C. A.; Young, M. L. Dual-Beam Scanning Electron Microscope (SEM) and Focused Ion Beam (FIB): A Practical Method for Characterization of Small Cultural Heritage Objects. *MRS Proc.* **2017**, *1656*, 355–369.

(6) Pradell, T.; Fernandes, R.; Molina, G.; Smith, A. D.; Molera, J.; Climent-Font, A.; Tite, M. S. Technology of Production of Syrian Lustre (11th to 13th Century). *J. Eur. Ceram. Soc.* **2018**, *38* (7), 2716–2727.

(7) Peck, G. *The Smithsonian Castle and the Seneca Quarry*; The History Press: Charleston, SC, 2013.

(8) Grissom, C. A.; Aloiz, E. M.; Vicenzi, E. P.; Livingston, R. A. Seneca Sandstone: A Heritage Stone from the USA. *Geol. Soc. Lond. Spec. Publ.* **2018**, SP486.4.

(9) Grissom, C. A.; Vicenzi, E. P.; Livingston, R. A.; Aloiz, E.; Little, N.; Giaccai, J.; Freedman, W. Manganese in Black Crusts on Seneca Sandstone. *Microsc. Microanal.* **2014**, *20* (S3), 2044–2045.

(10) Potter, R. M.; Rossman, G. R. Desert Varnish: The Importance of Clay Minerals. *Science* **1977**, *196* (4297), 1446–1448.

(11) Dorn, R. I. Rock Varnish. In *Geochemical Sediments and Landscapes*; Nash, D. J., McLaren, S. J., Eds.; Blackwell Publishing Ltd: Oxford, UK, 2007; pp 246–297.

(12) Humboldt, A. von; Wilson, J. *Personal Narrative*; Penguin classics; Penguin Books: London ; New York, 1995.

(13) Elvidge, C. D.; Moore, C. B. Restoration of Petroglyphs with Artificial Desert Varnish. *Stud. Conserv.* **1980**, *25* (3), 108–117.

(14) Dorn, R. I.; Moore, G.; Pagán, E. O.; Bostwick, T. W.; King, M.; Ostapuk, P. Assessing Early Spanish Explorer Routes Through Authentication of Rock Inscriptions. *Prof. Geogr.* **2012**, *64* (3), 415–429.

(15) Broecker, W. S.; Liu, T. Rock Varnish: Recorder of Desert Wetness? *GSA Today* **2001**, *11* (8), 4.

(16) Liu, T.; Broecker, W. S. Holocene Rock Varnish Microstratigraphy and Its Chronometric Application in the Drylands of Western USA. *Geomorphology* **2007**, *84* (1–2), 1–21.

(17) Liu, T.; Broecker, W. S. Rock Varnish Microlamination Dating of Late Quaternary Geomorphic Features in the Drylands of Western USA. *Geomorphology* **2008**, *93* (3–4), 501–523.

(18) Krinsley, D.; Dorn, R. I.; DiGregorio, B. Astrobiological Implications of Rock Varnish in Tibet. *Astrobiology* **2009**, *9* (6), 551–562.

(19) Allen, C. C.; Probst, L. W.; Flood, B. E.; Longazo, T. G.; Schelble, R. T.; Westall, F. Meridiani Planum Hematite Deposit and the Search for Evidence of Life on Mars—Iron Mineralization of Microorganisms in Rock Varnish. *Icarus* **2004**, *171* (1), 20–30.

(20) Liu, T.; Broecker, W. S. How Fast Does Rock Varnish Grow? *Geology* **2000**, *28* (2), 183-186.

(21) Vicenzi, E. P.; Grissom, C. A.; Livingston, R. A.; Weldon-Yochim, Z. Rock Varnish on Architectural Stone: Microscopy and Analysis of Nanoscale Manganese Oxide Deposits on the Smithsonian Castle, Washington, DC. *Herit. Sci.* **2016**, *4* (1).

(22) Macholdt, D. S.; Herrmann, S.; Jochum, K. P.; Kilcoyne, A. L. D.; Laubscher, T.; Pfisterer, J. H. K.; Pöhlker, C.; Schwager, B.; Weber, B.; Weigand, M.; et al. Black Manganese-Rich Crusts on a Gothic Cathedral. *Atmos. Environ.* **2017**, *171*, 205–220.

(23) Macholdt, D. S.; Jochum, K. P.; Pöhlker, C.; Arangio, A.; Förster, J.-D.; Stoll, B.; Weis, U.; Weber, B.; Müller, M.; Kappl, M.; et al. Characterization and Differentiation of Rock Varnish Types from Different Environments by Microanalytical Techniques. *Chem. Geol.* **2017**, *459*, 91–118.

(24) Dorn, R. I.; Krinsley, D. Spatial, Temporal and Geographic Considerations of the Problem of Rock Varnish Diagenesis. *Geomorphology* **2011**, *130* (1–2), 91–99.

(25) Fleisher, M.; Liu, T.; Broecker, W. S.; Moore, W. A Clue Regarding the Origin of Rock Varnish. *Geophys. Res. Lett.* **1999**, *26* (1), 103–106.

(26) Perry, R. S.; Adams, J. B. Desert Varnish: Evidence for Cyclic Deposition of Manganese. *Nature* **1978**, *276*, 489.

(27) McKeown, D. A.; Post, J. E. Characterization of Manganese Oxide Mineralogy in Rock Varnish and Dendrites Using X-Ray Absorption Spectroscopy. *Am. Mineral.* **2001**, *86* (5–6), 701–713.

(28) Engel, C. G.; Sharp, R. P. Chemical Data on Desert Varnish. *Geol. Soc. Am. Bull.* **1958**, *69* (5), 487.

(29) Thiagarajan, N.; Aeolus Lee, C.-T. Trace-Element Evidence for the Origin of Desert Varnish by Direct Aqueous Atmospheric Deposition. *Earth Planet. Sci. Lett.* **2004**, *224* (1–2), 131–141.

(30) Northup, D. E.; Snider, J. R.; Spilde, M. N.; Porter, M. L.; van de Kamp, J. L.; Boston, P. J.; Nyberg, A. M.; Bargar, J. R. Diversity of Rock Varnish Bacterial Communities from Black Canyon, New Mexico. *J. Geophys. Res. Biogeosciences* **2010**, *115* (G2).

(31) Tebo, B. M.; Bargar, J. R.; Clement, B. G.; Dick, G. J.; Murray, K. J.; Parker, D.; Verity, R.; Webb, S. M. Biogenic Manganese Oxides: Properties and Mechanisms of Formation. *Annu. Rev. Earth Planet. Sci.* **2004**, *32* (1), 287–328.

(32) Nealson, K. H. The Manganese-Oxidizing Bacteria. In *The Prokaryotes*; Dworkin, M., Falkow, S., Rosenberg, E., Schleifer, K.-H., Stackebrandt, E., Eds.; Springer New York: New York, NY, 2006; pp 222–231.

(33) Post, J. E. Manganese Oxide Minerals: Crystal Structures and Economic and Environmental Significance. *Proc. Natl. Acad. Sci.* **1999**, *96* (7), 3447–3454.

(34) *Biomineralization: Processes of Iron and Manganese ; Modern and Ancient Environments*; Skinner, H. C., Ed.; Catena Supplement; Catena-Verl: Cremlingen-Destedt, 1992.

(35) Garvie, L. A. J.; Burt, D. M.; Buseck, P. R. Nanometer-Scale Complexity, Growth, and Diagenesis in Desert Varnish. *Geology* **2008**, *36* (3), 215.

(36) Ortiz-Montalvo, D. L.; Vicenzi, E. P.; Ritchie, N. W.; Grissom, C. A.; Livingston, R. A.; Weldon-Yochim, Z.; Conny, J. M.; Wight, S. A. Chemical Compound Classification by Elemental Signatures in Castle Dust Using SEM Automated X-Ray Particle Analysis. *Microsc. Microanal.* **2018**, *24* (S1), 718–719.

(37) Lu, Y.; Tang, C.-F.; Wright, M. A. Optimization of a Commercial Brake Pad Formulation. *J. Appl. Polym. Sci.* **2002**, *84* (13), 2498–2504.

(38) Gietl, J. K.; Lawrence, R.; Thorpe, A. J.; Harrison, R. M. Identification of Brake Wear Particles and Derivation of a Quantitative Tracer for Brake Dust at a Major Road. *Atmos. Environ.* **2010**, *44* (2), 141–146.

(39) Hulskotte, J. H. J.; Roskam, G. D.; Denier van der Gon, H. A. C. Elemental Composition of Current Automotive Braking Materials and Derived Air Emission Factors. *Atmos. Environ.* **2014**, *99*, 436–445.

(40) Dorn, R. I. *Rock Coatings*; Developments in earth surface processes; Elsevier: Amsterdam ; New York, 1998.

(41) McGee, E. S. *Acid Rain and Our Nation's Capital: A Guide to Effects on Buildings and Monuments*; U.S. G.P.O ; U.S. Geological Survey, Information Services Washington, DC. Denver, CO, 1995.

(42) Krinsley, D. Models of Rock Varnish Formation Constrained by High Resolution Transmission Electron Microscopy. *Sedimentology* **1998**, *45* (4), 711–725.

(43) Livingston, R. A.; Grissom, C. A.; Aloiz, E. M. Building Stones of the National Mall. In *Field Guides*; Geological Society of America, 2015; Vol. 40, pp 543–571.

Appendix C

(1) Frederick, R. T.; Saha, S.; Diulus, J. T.; Luo, F.; Amador, J. M.; Park, D. H.; Garfunkel, E. L.; Keszler, D. A.; Herman, G. S. Thermal and Radiation Chemistry of Butyltin Oxo Hydroxo: A Model Inorganic Photoresist. *Microelectron. Eng.* **2019**. 15, 26-31.

(2) Frederick, R. T.; Amador, J. M.; Goberna-Ferrón, S.; Nyman, M.; Keszler, D. A.; Herman, G. S. Mechanistic Study of HafSO $_x$ Extreme Ultraviolet Inorganic Resists. *J. Phys. Chem. C* **2018**, *122* (28), 16100–16112.

(3) Menzel, D.; Gomer, R. Desorption from Metal Surfaces by Low-Energy Electrons. *J. Chem. Phys.* **1964**, *41*, 3311–3328.

(4) Redhead, P. A. Interaction of Slow Electrons with Chemisorbed Oxygen. *Can. J. Phys.* **1964**, *42*, 886–905.